THESIS

THE ROLE OF SOIL MOISTURE GRADIENTS IN SUMMERTIME CONVECTION INITIATION OVER THE COLORADO FRONT RANGE: AN IDEALIZED NUMERICAL MODELING STUDY

Submitted by

Evan Cowden

Department of Atmospheric Sciences

In partial fulfillment of the requirements

For the Degree of Master of Science

Colorado State University

Fort Collins, Colorado

Summer 2026

Master's Committee:

Advisor: Russ Schumacher

Kristen Rasmussen
Peter Nelson

Copyright by Evan M. Cowden 2026

All Rights Reserved

ABSTRACT

THE ROLE OF SOIL MOISTURE GRADIENTS IN SUMMERTIME CONVECTION INITIATION OVER THE COLORADO FRONT RANGE: AN IDEALIZED NUMERICAL MODELING STUDY

This study investigates how horizontal soil moisture gradients influence the initiation of convection (CI) along the Colorado Front Range using idealized convection-permitting simulations with the Weather Research and Forecasting (WRF) model. Using the tornado outbreak event of 21–22 June 2023 as a case study, eight perturbation experiments were conducted where the atmospheric initial and boundary conditions were held constant and only land surface soil moisture was modified. Soil moisture gradients were imposed across northeastern Colorado in both zonal and meridional orientations, with perturbation magnitudes derived from a 46-year NLDAS-2 June climatology. Across all experiments, a consistent response emerges: CI preferentially occurs over the dry portion of the soil moisture gradient. This is not due to enhanced moisture availability, but rather the dynamical response to differential surface heating. Dry soils suppress the evapotranspiration, increasing the Bowen ratio and enhancing sensible heat flux, which then deepens the daytime mixed layer and creates horizontal temperature gradients between adjacent wet and dry patches. Through hydrostatic balance, these temperature differences produce lower surface pressure over the warmer dry regions, driving low-level convergence along the soil moisture boundary. This convergence locally reduces convective inhibition and helps lift parcels to their level of free convection. This mechanism is robust across gradient orientations and spatial scales, with sharper gradients producing stronger responses. Overall, the results support a convergence-driven land–atmosphere coupling regime where surface thermal contrasts matter more than near-surface moisture availability in setting where deep convection is triggered. This highlights the importance

of representing land surface heterogeneity in high-resolution numerical models used for convective prediction in semi-arid, complex terrain environments like eastern Colorado.

ACKNOWLEDGEMENTS

First and foremost, I owe tremendous thanks to my advisor, Dr. Russ Schumacher. From day one, he welcomed me into the program with excitement about having me as a research student. His wealth of knowledge has pushed me to think curiously, and his mentorship made me feel like a true scientist. I also have to thank a former Schumacher group member, LtCol Casey Zoellick, for answering all of my Air Force related questions making the transition into graduate school so much smoother. I want to also thank LtCol Chandra Pasillas at AFIT, who went above and beyond helping me figure out how to juggle civilian graduate school with Air Force commitments.

I'm also deeply grateful to the faculty of the Department of Atmospheric Science at Colorado State University. Their courses gave me the foundation and tools I needed for this research. But what made the biggest impact was how much they genuinely care about what they do. Through their teaching, I'm able to see the natural world through a different lens than when I started this program. I feel really fortunate to have learned from scientists who have such an enthusiasm for their field and their students understanding.

The views expressed in this thesis are those of the author and do not reflect the official policy or position of the United States Air Force, Department of Defense, or the U.S. Government.

TABLE OF CONTENTS

ABSTRACT ii
ACKNOWLEDGEMENTS iv
LIST OF TABLES vii
LIST OF FIGURES viii

Chapter 1 Introduction 1
1.1 Research Questions 5

Chapter 2 Background and Theory 6
2.1 Energy Exchange between Land and Atmosphere 6
2.2 Summertime Convection in CO & Soil Moisture Feedback 9

Chapter 3 Data and Methodology 13
3.1 Observational and Reanalysis Datasets 13
3.1.1 NLDAS-2 Noah Land Surface Data 13
3.1.2 Radar-Based Precipitation Observations 14
3.2 Model Configuration (WRF) 14
3.2.1 Domain Configuration 15
3.2.2 Physical Parameterizations 16
3.2.3 Initial and Boundary Conditions 17
3.3 Case Study Overview: 21 June 2023 Severe Weather Event 18
3.3.1 Synoptic Setup 18
3.3.2 Convective Outlook 21
3.4 Experiment Design 22
3.4.1 Soil Moisture Perturbation Experiments 23
3.5 Evaluation Metrics and Analysis Methods 28
3.5.1 Statistical Methods 31

Chapter 4 Results 34
4.1 Overview of Soil Moisture-Atmosphere Response 34
4.1.1 Evaluation of the Climatology against the Observed 35
4.1.2 Surface Energy Partitioning using the Bowen Ratio 37
4.2 The Initiation of Convection 42
4.3 Convective Available Potential Energy & Inhibition 49
4.3.1 Low-level Clouds 59
4.4 Storm Morphology 63
4.5 Precipitation 68
4.6 Surface Pressure Perturbations 75
4.7 Surface Divergence Anomaly 77

Chapter 5 Discussion 80
5.1 Synthesis of Soil Moisture–Convection Feedback 80

5.2 Thermodynamic vs. Dynamic Controls on Initiation 81
5.3 Role of Orography in Land–Atmosphere Feedback 82
5.4 Special Consideration to EX_5 83
5.5 Limitations and Model Sensitivity 87

Chapter 6 Conclusion 89
6.1 Summary 89
6.2 Future directions 90

LIST OF TABLES

3.1 WRF model configuration used in this study. 16
3.2 Physical parameterization schemes used in the WRF simulations. 17
3.3 Experiment groupings based on soil moisture perturbation rectangle. 29
3.4 Latitude and longitude targets of the averaging box for Skew-T analysis by grouping. . 32

4.1 Summary of area-averaged Skew-T thermodynamic diagnostics at 1000 MDT for each experiment and grouping, centered on the observed convection initiation region. 57

LIST OF FIGURES

1.1 MRMS Reflectivity at 2000 MDT on June 21st, 2023 4

2.1 Shows the generalization of the Bowen Ratio over dry and wet soil conditions. 12

3.1 Graphic showing the WRF domains for this study. Overlaid with Reflectivity at hour 12 of the Control Climatology run. 15
3.2 ERA5 500 hPa Absolute Vorticity and wind barbs at 16Z, or 1000 MDT, on 21 June 2023 20
3.3 ERA5 850 hPa Specific Humidity and wind barbs at 16Z, or 1000 MDT, on 21 June 2023 20
3.4 ERA5 Temperature advection at 850 hPa at 16 UTC, or 1000 MDT, on June 21st 2023 21
3.5 SPC Day-1 Convective Outlook issued at 1630Z on 21 June 2023 (Enhanced Risk). Left: categorical severe weather outlook. Right: tornado probability outlook. 22
3.6 Example of the Top Layer of the Climatological Soil Moisture 24
3.7 Colorado elevation in meters from WRF CONTROL file overlaid with major roads and Key Orographic Features. Including, the Northern Cheyenne Ridge, The Platte River Basin, the Denver Convergence Vorticity Zone, and the Southern Palmer Divide. . . . 25
3.8 Multi-panel Figure showing all the Soil Moisture Perturbation boxes on the top layer of the soil moisture field in WRF for all 8 experiments. 27
3.9 Soil Moisture perturbation region used in WRF experiments. 29
3.10 Center target pixel of the averaging box used for Skew-T analysis. 32

4.1 NLDAS resolved Soil Moisture Percentile against a climatology created from 1979-2025 across the US in June of 2023 36
4.2 Comparison of the reflectivity from the modeled output and observed radar reflectivity at 2000 MDT, 2300 MDT, on June 21st and 0200 MDT on June 22nd, WRF REFD_MAX from the GFS Run (left) MRMS Composite Reflectivity (right) 38
4.3 Accumulated precipitation (mm) of the GFS run with the GFS soil moisture (left) MRMS observed Cumulative Precipitation in the nested domain (right) 39
4.4 Time series of the Bowen ratio (β = HFX/LH) departure from the CONTROL run averaged over the western (left) and eastern (right) sub-regions of the soil moisture perturbation zone for Grouping #1 (E/W gradient, large patch). The zero line corresponds to the CONTROL climatological simulation, such that positive departures indicate a shift toward greater sensible heat flux relative to the control, while negative departures reflect enhanced latent heat flux. Shading denotes nighttime hours (1900-0600 MST), during which the Bowen ratio is not physically meaningful. 40
4.5 As in Figure 4.4, but for Grouping #2 (E/W gradient, narrow patch), averaged over the western (left) and eastern (right) sub-regions. 40
4.6 As in Figure 4.4, but for Grouping #3 (N/S gradient), averaged over the northern (left) and southern (right) sub-regions. 41
4.7 Hours of developed convection initiation (1500 MDT or 1600 MDT) overlaid with reflectivity and Soil Moisture gradients from each of the groupings and EX_5 43

4.8 Convective initiation diagnostics for Group 1. Histograms show the number of pixels exceeding 40 dBZ over the wet and dry soil moisture perturbation rectangles at four selected hours. Mean soil moisture in each rectangle is shown beneath each panel. . . . 45
4.9 Convective initiation diagnostics for Group 2 (E/W gradient, narrow patch). Histograms show the number of pixels over 40 dBZ over the dry and wet soil moisture perturbation, for West(top) and East(bottom) configurations. Mean volumetric soil moisture within each subregion is shown in black. 46
4.10 Convective initiation diagnostics for Group 3 (N/S gradient). Histograms show the number of pixels exceeding 40 dBZ over the dry and wet soil moisture regions, for the North (top) and South (bottom) configurations. Mean volumetric soil moisture within each subregion is shown beneath each panel. 48
4.11 Area-averaged Skew-T log-p profile at 1000 MDT for the CONTROL simulation, Grouping #1 (E/W gradient, large patch), centered on the observed CI region. Solid red and green lines show temperature and dewpoint. The dashed black line shows the lifted parcel profile. Filled circles indicate the LCL (black), LFC (blue), and EL (magenta). Key thermodynamic diagnostics are annotated in the upper left and right of each panel. 50
4.12 As in Figure 4.11, but for EX_1 Dry→Wet. 51
4.13 As in Figure 4.11, but for EX_2 Wet→Dry. 51
4.14 Area-averaged Skew-T log-p profile at 1000 MDT for the CONTROL simulation, Grouping #2 (E/W gradient, narrow patch), centered on the observed CI region. Solid red and green lines show temperature and dewpoint. The dashed black line shows the lifted parcel profile. Filled circles indicate the LCL (black), LFC (blue), and EL (magenta). Key thermodynamic diagnostics are annotated in the upper left and right of each panel. 52
4.15 As in Figure 4.11, but for EX1_2 Narrow Dry→Wet. 53
4.16 As in Figure 4.11, but for EX2_2 Narrow Wet→Dry. 53
4.17 Area-averaged Skew-T log-p profile at 1000 MDT for the CONTROL simulation, Grouping #3 (N/S gradient, large patch), centered on the observed CI region. Solid red and green lines show temperature and dewpoint. The dashed black line shows the lifted parcel profile. Filled circles indicate the LCL (black), LFC (blue), and EL (magenta). Key thermodynamic diagnostics are annotated in the upper left and right of each panel. 55
4.18 As in Figure 4.11, but for EX_3 N/S Wet→Dry. 56
4.19 As in Figure 4.11, but for EX_4 N/S Dry→Wet. 56
4.20 Composite bottom-layer skew-T log-p profiles at $t = 0$ h averaged over the region of strongest convective initiation (CI) signal for each soil moisture perturbation grouping. 60
4.21 Comparison of the averaged cloud fraction at 0800 MDT in %. Top row: Groups #1 and #2. Bottom row: Group #3. 62
4.22 Grouping #3 Comparison of the cloud water mixing ratio at 0800 MDT in g/kg. 63
4.23 Grouping #1 Cloud fraction (blues) and the cloud top temperature between 1000–700 hPa at 0800 MDT. 64
4.24 Grouping #3 Cloud fraction (blues) and the cloud top temperature between 1000–700 hPa at 0800 MDT. 64

4.25 Storm track of the CONTROL Run from hours 28-36 of the forecast, with overlaid surface equivalent potential temperature 65
4.26 Convective initiation and cell development over dry perturbation regions for Grouping #1, highlighting the reinforcement of storm intensity and cold-pool formation. 66
4.27 Centroid-based storm tracks and reflectivity contours for Grouping #2, showing the overall storm morphology and track. 67
4.28 Convective initiation and cell development over dry perturbation regions for Grouping #3, highlighting the reinforcement of storm intensity and cold-pool formation. 68
4.29 Accumulated precipitation from the CONTROL climatology run 69
4.30 Coordinates that record the maximum cumulative rainfall in mm by experiment numbers 70
4.31 Averaged precipitation over the outlined red box for the CONTROL simulation. Hourly rainfall rate is shown over the forecast period, with the maximum precipitation marked by a red dot. 72
4.32 Averaged precipitation over the outlined red box for the DRY→WET (EX_1) simulation. Hourly rainfall rate is shown over the forecast period, with the maximum precipitation marked by a red dot. 72
4.33 Averaged precipitation over the outlined red box for the Narrow DRY→WET (EX_1_2) simulation. Hourly rainfall rate is shown over the forecast period, with the maximum precipitation marked by a red dot. 73
4.34 Averaged precipitation over the outlined red box for the NS WET→DRY (EX_3) simulation. Hourly rainfall rate is shown over the forecast period, with the maximum precipitation marked by a red dot. 73
4.35 Averaged precipitation over the outlined red box for the NS DRY→WET (EX_4) simulation. Hourly rainfall rate is shown over the forecast period, with the maximum precipitation marked by a red dot. 74
4.36 Surface Pressure anomaly and the 10 m winds at 1000 MDT from Group #1 comparing the the surface pressure of the control run to the perturbations runs. 76
4.37 Surface Pressure anomaly and the 10 m winds at 1000 MDT from Group #2 comparing the the surface pressure of the control run to the perturbations runs. 76
4.38 Surface Pressure anomaly and the 10 m winds at 1000 MDT from Group #3 comparing the the surface pressure of the control run to the perturbations runs. 76
4.39 10 m divergence ($10^{-4}\,\mathrm{s}^{-1}$; blue = convergence, red = divergence) for the broad east to west experiments. Left: CONTROL with surface pressure (hPa) contoured. Center: EX_1 (Dry→Wet). Right: EX_2 (Wet→Dry), each with ΔPSFC (hPa; dashed = negative, solid = positive). Red rectangle:perturbation region; red dashed line: dry/wet interface. 78
4.40 As in Fig. 4.39, for the narrow east to west experiments. Center: EX1_2 (Narrow Dry→Wet). Right: EX2_2 (Narrow Wet→Dry). 79
4.41 As in Fig. 4.39, for the north to south experiments. Center: EX_3 (NS Wet→Dry). Right: EX_4 (NS Dry→Wet). Red dashed line oriented horizontally, marking the north to south dry/wet interface. 79

5.1 Summary of the observed results. 81
5.2 Count of convective pixels INSIDE Pivot circles area in the Polka Dot Run vs. the climatology run 84

5.3 Count of convective pixels OUTSIDE Pivot circles area in in the Polka Dot Run vs. the climatology run 85
5.4 The total Bowen ratio over the Polka Dot run 86
5.5 Surface Pressure anomaly and 10 m winds at 1000 MDT for the Control run and EX_5 86

Chapter 1

Introduction

During the summer months, Colorado's Eastern Slope is a frequent breeding ground for Mesoscale Convective Systems (MCSs) that can go on to deliver substantial rainfall to the Great Plains region (Ashley et al., 2003). These severe weather events are an important area of research as they account for 30% to 70% of the total warm seasonal rainfall seen by the Great Plains (Carbone et al., 2002; Fritsch et al., 1986; Haberlie and Ashley, 2019; Tripoli and Cotton, 1981). Because of these hydrologic impacts, understanding the complex processes that regulate the initiation of convection along the Colorado Front Range remains an important area of research.

Eastern Colorado is also characterized by its vast irrigated agriculture infrastructure. Approximately 3.28 million acres of land in the state are irrigated and account for nearly 89% of total statewide water use and contribute a whopping $\$47$ billion to Colorado's agricultural economy every year (US Department of Commerce, 2024). Irrigation has the ability to directly alter the soil moisture through the depth of the root zone. This can introduce persistent, and sharp spatial heterogeneity in what is an otherwise dry landscape. These differences in soil moisture change how much of the available surface energy goes into sensible heating versus evaporation, which can then shift the Bowen ratio and ultimately influence the above surface boundary layer growth and structure (Findell and Eltahir, 2003; Pielke, 2001).

The interaction between soil moisture and developing convective cells is complex and not fully understood. In a study using GLACE data, it is suggested that there is strong coupling between the soil moisture and precipitation in the region East of the Rocky Mountains (Koster et al., 2004). In general, drier soils tend to suppress evapotranspiration, reducing the latent heat flux and increasing the sensible heating. Latent heat flux refers to the portion of surface energy used for evaporation or, more technically, the energy that goes into changing liquid water into water vapor. When the soils are dry, less energy is used for evaporation, so more energy goes into sensible heat flux. And sensible heat is the energy that directly warms the air near the surface. The enhanced sensible

heating warms the air above the surface, increasing the buoyancy and promoting deeper boundary layer growth (Stull, 1988, p. 5).

In contrast, wetter soils enhance the latent heat flux through evaporation, increasing the humidity near the surface, while also limiting surface warming and ability for the boundary layer to deepen. In this case, more of the available energy is used to evaporate water rather than heat the air, which keeps surface temperatures lower and reduces the rate at which the boundary layer grows. When dry and wet patches exist adjacent to one another, these differences in surface heating can generate horizontal temperature gradients, induce pressure perturbations, and make areas of mesoscale convergence capable of lifting air parcels (Ookouchi et al., 1984; Segal and Arritt, 1992).

The typical initiation of convection along the Colorado Front Range is frequently associated with a combination of upslope flow, differential heating, and mesoscale convergence that develop along the topographic boundary between the mountains and the adjacent plains. With the ingredients-based framework for convection (Doswell, 1987), convective development requires sufficient low-level moisture, instability, lifting, and vertical wind shear. Soil moisture can influence several of these ingredients indirectly. Increased evapotranspiration may enhance the available moisture and convective available potential energy (CAPE), while reduced sensible heating can increase convective inhibition (CIN) (US Department of Commerce, 2024). At the same time, spatial gradients in soil moisture can provide a dynamical lifting mechanism through thermally driven circulations, even in environments with weak large-scale forcing.

Altered soil moisture can change several of the key ingredients for convection. For example, irrigation increases evapotranspiration and the associated latent heat flux into the lower atmosphere, while simultaneously cooling the surface air and reducing sensible heat flux (Yang et al., 2019). This enhanced flux of moisture can intensify the hydrologic cycle locally. The resulting increase in low level moisture can raise the convective available potential energy (CAPE), promoting atmospheric instability. In contrast, cooler surface temperatures associated with wetter soils can increase convective inhibition (CIN), making it more difficult for convection to initiate. These thermody-

namic effects show how irrigation can create competing results on the conditions necessary for the development of convection.

Observational studies have shown that wetter soils are associated with lower lifting condensation level (LCL) heights due to the enhanced near surface moisture, creating a more favorable thermodynamic environment for convection (Barton et al., 2021; Taylor, 2015; Taylor et al., 2013). Upon first glance, this suggests a straightforward conclusion; convection should preferentially initiate over wetter soils. However, in the absence of strong large-scale forcing, horizontal gradients in soil moisture can be strong enough to generate thermally driven mesoscale circulations and provide a lifting mechanism capable of initiating and organizing convection (Frye and Mote, 2010). These findings indicate that it is not the absolute soil moisture alone, but rather the spatial gradients and contrasts in soil moisture that strongly influence where convective initiation occurs (Taylor, 2015; Taylor et al., 2013). The experiments conducted in this study aim to isolate and better understand how such gradients influence summertime convection along the Colorado Front Range. Previous work done by Hohenegger and Stevens, showed using convection-permitting modeling in a tropical regime that the spatial difference in soil moisture can induce circulations that when drying the soil to its permanent wilting point generates a circulations that is strong enough to overtake the inhibition (Hohenegger and Stevens, 2018).

Even with the progress made in understanding land–atmosphere interactions, there's still a lot unknown about how soil moisture gradients interact with a favorable severe weather environment along the Colorado Front Range. In particular, it's still unclear how soil moisture heterogeneity shapes mesoscale convergence, the boundary layer, and the timing of convection during severe weather events. Much of the existing literature does not center around cases where the land surface feedback can dominate the evolution of convection. However, it is important to mention that severe weather events along the Colorado Front Range are often paired within strong synoptic forcing, favorable vertical wind shear and orographic flows. In these complex environments, it is unclear whether soil moisture gradients can be the primary thing to modify the location and timing of convection, or whether they can substantially alter storm evolution itself. Understanding how these

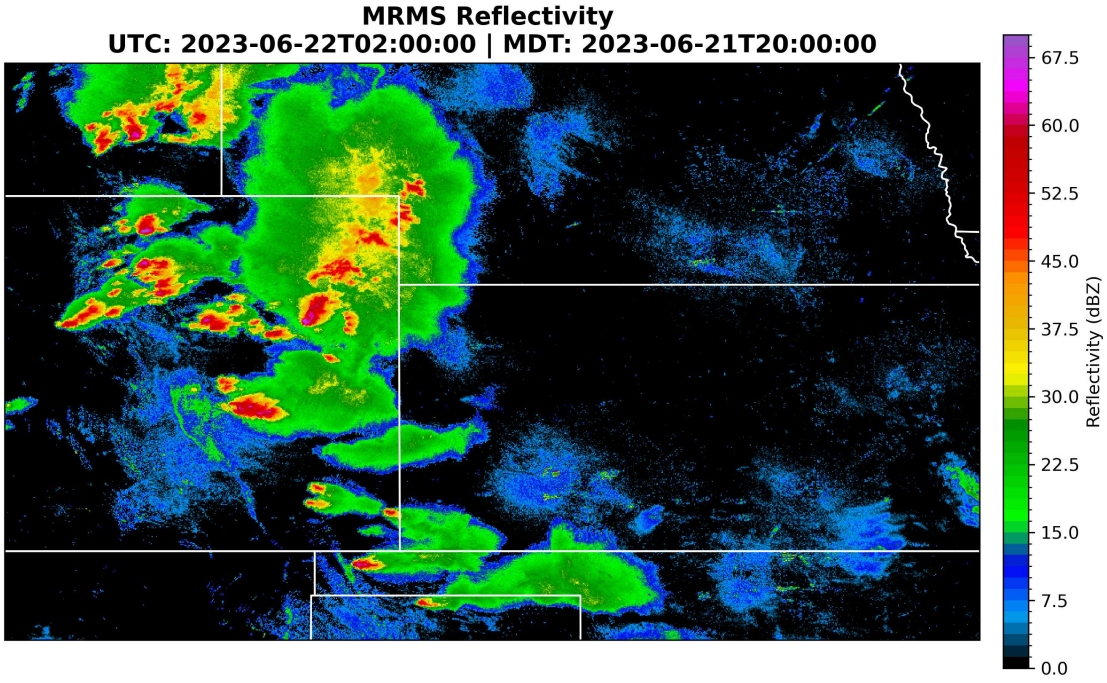


Figure 1.1: MRMS Reflectivity at 2000 MDT on June 21st, 2023

mesoscale land surface perturbations interact with the larger scale atmospheric forcing remains an important open question.

To tackle this, this study focuses on a severe weather event that occurred from 21–22 June 2023, a period that was chosen because it falls during Colorado's peak summertime severe weather season. This event was particularly notable for its strength, duration, and size, producing a tornado outbreak and numerous intense hailstorms across the region, making it an ideal case for examining the land/atmosphere interactions (US Department of Commerce, 2024). Using convection-permitting WRF simulations, a series of idealized soil moisture experiments were conducted where the atmosphere was held constant and only the land surface was modified (Skamarock et al., 2019). This study aims to show exactly how horizontal soil moisture gradients influence mesoscale circulations, the timing of convective initiation, and storm evolution across eastern Colorado.

Figure 1.1 shows a snapshot of composite radar reflectivity from the MRMS system on 21 June 2023 at 2000 MDT. Convective cells initiated along the Colorado Front Range and quickly intensified into a system producing severe hail and numerous tornadoes across eastern Colorado.

This figure highlights the spatial scale and intensity of the event, motivating its selection as a case study to examine how soil moisture heterogeneity can influence convective initiation and evolution.

The primary hypothesis of this study is that sharp gradients in soil moisture will be enough to modify the spatial distribution of surface energy fluxes (latent and sensible heat flux) which in turn alters the boundary-layer growth across the region. These differences in the surface heating are expected to create thermally driven mesoscale circulations that enhance the low level convergence locally. As a result, the location, timing, and intensity of convective initiation will differ from what was observed during the 21–22 June 2023 event Fig. 1.1.

1.1 Research Questions

The following research questions were used to guide this study:

1. How do imposed soil moisture gradients modify the initiation of convection timing and storm intensity during the 21–22 June 2023 severe weather event?

2. Through what mechanisms do sharp soil moisture gradients alter mesoscale convergence, boundary-layer growth, and surface flux partitioning?

3. How sensitive is the evolution of convection to the to the magnitude and orientation of the imposed soil moisture gradients (East$\rightarrow$West, North$\rightarrow$South)?

Chapter 2

Background and Theory

2.1 Energy Exchange between Land and Atmosphere

To first understand how the soil moisture feedback in the Front Range of Colorado can be connected with storm evolution, it is important to examine the underlying physical equations governing the land-atmosphere interactions. The net radiation (R_{n}) is commonly written as the combined sum of the upward and downward longwave and shortwave components. At the land's surface, the available net radiation (R_{n}) can be partitioned into the sensible heat flux (H), latent heat flux (LE), and the heat into the ground or the ground heat flux (G) (Stull, 1988):

$$R_{\mathrm{n}} = H + LE - G \tag{2.1}$$

The separation of the sensible (H) and latent heat (LE) flux is commonly expressed through the Bowen ratio (β) (Bowen, 1926):

$$\beta = \frac{H}{LE} \tag{2.2}$$

The Bowen ratio provides a good measure of how efficiently the surface converts the available energy into atmospheric warming, versus evaporative cooling. In semi-arid environments like eastern Colorado, soil moisture can have an impact on this ratio (Seneviratne et al., 2010). Dry soils will suppress evapotranspiration, reducing LE and increasing H for a relatively fixed net radiation (R_{n}), resulting in higher Bowen ratios ($\beta > 1$). On the other hand, wet soils can enhance evapotranspiration and latent cooling, producing lower Bowen ratios ($\beta < 1$). So another way to look at how soil moisture heterogeneity manifests dynamically is through the spatial gradients in the Bowen ratio.

The Food and Agriculture Organization (FAO) Penman–Monteith equation also helps formalize the sensitivity of evapotranspiration to radiative and meteorological variables and is commonly

applied in its standardized form (Penman, 1948):

$$ET_0 = \frac{0.408\Delta(R_\mathrm{n} - G) + \frac{900}{T}\gamma u_2 \delta e}{\Delta + \gamma(1 + 0.34u_2)} \tag{2.3}$$

where ET_0 is the reference evapotranspiration rate, Δ is the slope of the saturation vapor pressure curve, R_n is the net radiation, G is the ground heat flux, T is the mean air temperature, γ is the psychrometric constant, u_2 is the wind speed at 2 meters, and δe is the vapor pressure deficit.

This formula assumes a "well-watered" reference surface and that the near surface atmosphere is in equilibrium with that surface (DeJonge et al., 2025). That means, that the temperature, humidity, and wind profiles near the ground should reflect the exchanges of energy and moisture from the surface. For this to be a good approximation, a large and uniformly moist patch (upwind distance of consistent surface conditions) is needed; otherwise, the 2m temperature and humidity measurements may not fully capture the effects of evapotranspiration. This is particularly difficult in arid and semiarid regions, where maintaining these conditions often requires sustained irrigation. When these assumptions break down, the equation can misconstrue evapotranspiration, especially since drier soils can increase a pressure deficit and lead to artificially high reference ET estimates.

This equation explicitly relates evapotranspiration to the surface energy balance through the soil heat flux (G), net radiation (R_n), and atmospheric variables such as air temperature and vapor pressure deficit. Because latent heat flux is directly proportional to evapotranspiration, variations in soil moisture alter the magnitude of LE and therefore shift the Bowen ratio. In this way, the Penman–Monteith framework provides the physical basis linking soil moisture variability to surface energy partitioning.

Changes in the Bowen ratio directly modify the boundary layer thermodynamics. A higher Bowen ratio (larger sensible heat flux compared to latent heat flux) favors larger surface warming, increased surface potential temperature, and more rapid boundary-layer growth. In contrast, a lower Bowen ratio, closer to 0, indicates that a greater fraction of available energy is partitioned into latent heat flux; promoting evaporative cooling, higher near-surface humidity, and comparatively shallower mixed layers.

When soil moisture varies horizontally, these differences in surface energy partitioning create spatial gradients in temperature and the boundary layer depth between adjacent dry and wet patches. Dry regions, characterized by higher Bowen ratios, develop warmer and deeper mixed layers, while wet regions remain cooler and more weakly mixed.

Through hydrostatic balance,

$$\frac{\partial p}{\partial z} = -\rho g \tag{2.4}$$

a warmer atmospheric column becomes less dense and expands vertically, lowering the surface pressure relative to a cooler neighboring column. These pressure perturbations generate horizontal pressure gradient forces that drive low-level flow toward the warmer, high Bowen ratio region. By mass continuity, horizontal convergence ($\nabla \cdot \mathbf{V} < 0$) is associated with upward vertical motion. This thermally driven circulation provides a dynamically forced lifting mechanism capable of initiating convection even in the absence of strong large-scale ascent. To connect this surface-driven process to a diagnostic framework for vertical motion, it is useful to consider the generalized omega equation used by Rantanen et al. (2017). In its simplified form,

$$L(\omega) = F_{\mathrm{V}} + F_{\mathrm{T}} + F_{\mathrm{F}} + F_{\mathrm{Q}} + F_{\mathrm{A}} \tag{2.5}$$

where $L(\omega)$ is the omega operator applied to vertical pressure velocity, F_{V} represents the forcing from vertical velocity advection, F_{T} is the forcing from temperature advection, F_{F} is the forcing from friction, F_{Q} is the forcing from diabatic heating, and F_{A} is the forcing from horizontal advection of absolute vorticity. The forcing of primary interest here is the contribution from diabatic heating, F_{Q}. After applying the horizontal Laplacian to the thermodynamic energy equation, the diabatic forcing term takes the form:

$$F_{\mathrm{Q}} = -\frac{R}{c_{\mathrm{p}}}\nabla^2 Q \tag{2.6}$$

where Q represents diabatic heating, R is the specific gas constant for dry air, and c_{p} is the specific heat at constant pressure. Diabatic effects associated with the boundary layer (J_{BL}) are mostly

related to evaporative cooling and do not directly heat the atmospheric column; instead, they locally cool the near surface air ($J_{\mathrm{BL}} < 0$). In contrast, diabatic heating associated with condensation is substantially larger ($J_{\mathrm{cond}} \gg 0$). When moisture supplied by evapotranspiration is advected, lifted, and subsequently condensed, strong positive diabatic heating is produced aloft.

Using this framework, the spatial variability in the Bowen ratio influences the structure of Q by modifying the boundary layer temperature tendencies and the distribution of condensational heating once convection initiates. Because the omega equation emphasizes the Laplacian of diabatic heating, horizontal contrasts in heating are dynamically important. Additionally, the soil moisture heterogeneity also modulates the thermal advection term (F_{T}) in the omega equation. Horizontal temperature gradients arising from differential surface heating drive wind perturbations at the mesoscale, and these wind/temperature correlations directly affect vertical motion through the advection of warmer air from dry regions and cooler air from wet regions (Rantanen et al., 2017). So, soil moisture heterogeneity affects vertical motion through multiple pathways: not just through its contribution to atmospheric moisture and thermally induced pressure gradients, but also through diabatic heating contrasts tied directly to surface energy partitioning and modifications to the thermal advection term when wind perturbations develop in response to surface-induced pressure gradients.

2.2 Summertime Convection in CO & Soil Moisture Feedback

Summertime convection along the Colorado Front Range is strongly influenced by the interaction between complex terrain, diversely heated land surface conditions, and weak to moderate synoptic forcing (Smith, 2019). During the warm summer months, deep convection frequently initiates along the eastern slopes of the Rocky Mountains, where upslope flow, differential heating, and boundary-layer convergence act to locally erode convective inhibition. In the absence of strong large-scale ascent, mesoscale and land–atmosphere processes play an important role in determining when and where convective initiation occurs.

A common framework for understanding convective development is the ingredients-based methodology, which proposes that for convection to happen it requires sufficient moisture, instability, and a lifting mechanism (Doswell, 1987). Soil moisture influences all three of these ingredients indirectly through its control on surface energy partitioning and, therefore, can also control the Bowen ratio. Increased soil moisture enhances latent heat flux at the expense of sensible heat flux, increasing surface humidity while simultaneously reducing temperature (Schär et al., 1999). This coupling links land surface conditions to boundary layer thermodynamics and convective potential.

Early conceptual models suggested that wetter soils should promote convection by increasing evapotranspiration and boundary-layer moisture, thereby increasing CAPE. However, both observational and modeling studies have shown that this relationship depends strongly on the spatial scale and magnitude of the soil moisture differences. Frye and Mote (2010) showed that in environments lacking strong synoptic forcing, horizontal gradients in soil moisture can generate thermally drive the mesoscale dynamics capable of initiating convection and organizing mesoscale convective systems. These circulations arise from differential surface heating, effectively linking soil moisture gradients to convergence through Bowen ratio contrasts.

In the Colorado Front Range specifically, Gaal and Kinter (2021) found a negative correlation between absolute soil moisture and MCS initiation, with convection preferentially initiating over anomalously dry soil patches at smaller spatial scales. Over larger domains, however, the magnitude and sharpness of soil moisture gradients were more important than absolute soil moisture values. These results suggest that it is not simply "wet" or "dry" soils that matter for convection initiation, but rather the spatial gradients in surface energy partitioning and the thermally driven circulations they induce.

Irrigation adds an additional layer of complexity to this land–atmosphere coupling in eastern Colorado. Approximately 3.28 million acres of land in Colorado are irrigated, accounting for nearly 89% of the state's total water usage and contributing substantially to the state economy (Colorado, 2023). Irrigated agriculture, particularly center-pivot systems across northeastern Col-

orado, introduces persistent and spatially sharp soil moisture contrasts that directly modify the Bowen ratio at scales relevant for mesoscale convective processes.

Previous studies examining irrigation impacts have identified competing thermodynamic effects. Yang et al. demonstrated that irrigation enhances evapotranspiration and latent heat flux, increasing near-surface humidity and CAPE (Yang et al., 2019). At the same time, irrigation reduces sensible heating, lowers the Bowen ratio, and can increase convective inhibition (CIN), potentially suppressing convection initiation. This highlights that enhanced moisture and instability can coexist with reduced dynamical forcing associated with weaker thermal gradients.

In semi-arid regions, this complexity is further highlighted by Taylor et al. (2013), who showed that afternoon rainfall preferentially occurs over relatively drier soils compared to their surroundings. This preference is consistent with the idea that dry soils, through higher Bowen ratios, promote stronger sensible heating, deeper boundary layers, enhanced hydrostatic pressure falls, and mesoscale convergence sufficient to trigger convection.

Taken together, these studies suggest that summertime convection along the Colorado Front Range is particularly sensitive to soil moisture non-uniformity imposed by irrigation and natural land surface variability. The balance between enhanced moisture supply and thermally driven dynamical forcing, governed by the Bowen ratio, remains an open question. Moreover, recent work has shown that wind shear, which can be locally altered by surface induced pressure perturbations and horizontal wind gradients, can also play a role in organizing convective systems and modulating their intensity and structure (Taylor et al., 2026). This underscores the importance of considering not only the thermodynamic environment shaped by soil moisture heterogeneity but also the additional effects from mesoscale wind perturbations. These findings motivate the controlled experiments conducted in this study to isolate the role of soil moisture induced surface energy partitioning on the convective evolution.

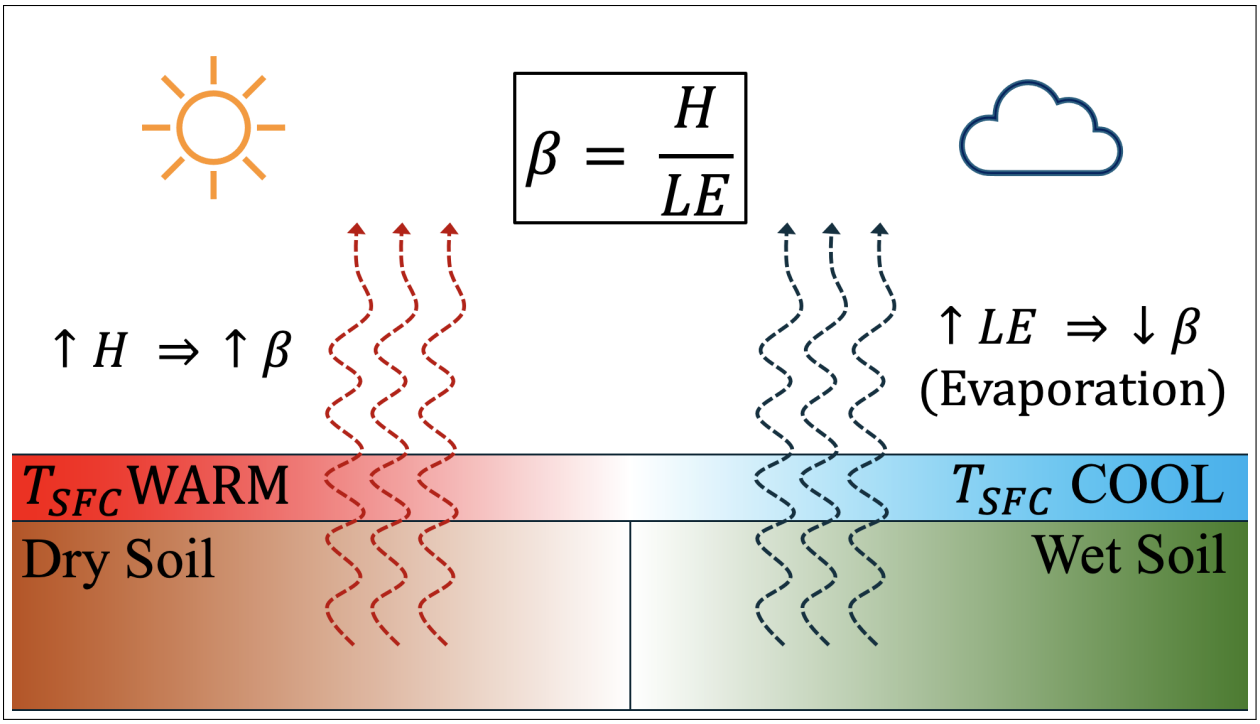


Figure 2.1: Shows the generalization of the Bowen Ratio over dry and wet soil conditions.

Chapter 3

Data and Methodology

3.1 Observational and Reanalysis Datasets

3.1.1 NLDAS-2 Noah Land Surface Data

NASA's North American Land Data Assimilation System, Version 2 (NLDAS-2), Noah land surface model output was used to construct a climatology of June soil moisture for initializing the WRF simulations (Mitchell et al., 2004). NLDAS-2 provides observation constrained land surface fields over North America through the assimilation of gauge-based precipitation, and surface observations on a high resolution (0.125°) grid. NLDAS-2 was selected for this study because of its demonstrated skill in representing soil moisture variability across the United States and consistency with the Noah Land Surface Model used within WRF (Xia et al., 2012).

To create a climatology fitting for this study, the monthly-mean soil moisture data from the 0.125°NLDAS-2 Noah product was extracted for all June months from 1979 through 2025, yielding a total sample size of 46 years. June was selected because a substantial fraction of Colorado's pre-monsoonal convection activity occurs during this month, making it a good period for land–atmosphere interactions relevant to convection. In Colorado, the summer is the wettest of the seasons for the Eastern foothills. And June is one of the months that racks up some of the maximum average precipitation for many counties in Eastern CO (Childs and Schumacher, 2019). This makes June a good month for the study because the soil moisture variability can strongly modulate surface energy partitioning, boundary-layer growth, and mesoscale dynamics. Additionally, Eastern Colorado is a hotspot for summertime severe thunderstorms that can produce damaging tornadoes and severe hail. It is also known to be the place of initiation for some of the most intense mesoscale convective systems that can produce anywhere from 30-70% of the total rainfall in the Great Plains (Yang et al., 2019). Since storms originated in this area can have such an impact on

the populations and agriculture East of the Rocky Mountains, it is an important area to understand the dynamics of the atmosphere and surface.

The Noah land surface model represents soil moisture using four discrete soil layers with depths of 0–10 cm, 10–40 cm, 40–100 cm, and 100–200 cm. Monthly-mean soil moisture values from each layer were averaged across all June months over the 46 years to create a vertically consistent June soil moisture climatology.

3.1.2 Radar-Based Precipitation Observations

The actual observed precipitation and evolution of convection were compared to the experiment output using the NOAA/NSSL Multi-Radar/Multi-Sensor (MRMS) system (Zhang et al., 2016). The MRMS system, developed by the NOAA National Severe Storms Laboratory, merges data from multiple WSR-88D (Weather Surveillance Radar, 1988 Doppler) radars into a high resolution national mosaic. MRMS provides a high resolution, radar based precipitation and reflectivity estimates at approximately 1 km spatial and 2–5 minute temporal resolution.

MRMS reflectivity fields were used to identify convection initiation and storm morphology to assess the timing and spatial distribution of simulated convection during the June 21, 2023 event. Reflectivity thresholds of 40 dBZ were used to define convective initiation which is consistent with the practice for identifying robust updraft-driven precipitation cores (Kain et al., 2008; Weisman et al., 2008). While radar-based reflectivity is subject to uncertainties such as beam blockage, hail contamination, and attenuation, MRMS provides good observational basis for evaluating the spatial and temporal evolution of simulated convection from WRF.

3.2 Model Configuration (WRF)

The Advanced Research core of the Weather Research and Forecasting Model (WRF-ARW) was used to simulate the 21–22 June 2023 convective event. WRF-ARW is a nonhydrostatic, fully compressible atmospheric model that employs terrain-following sigma coordinates and is widely used for mesoscale and convection-permitting simulations (Skamarock et al., 2019).

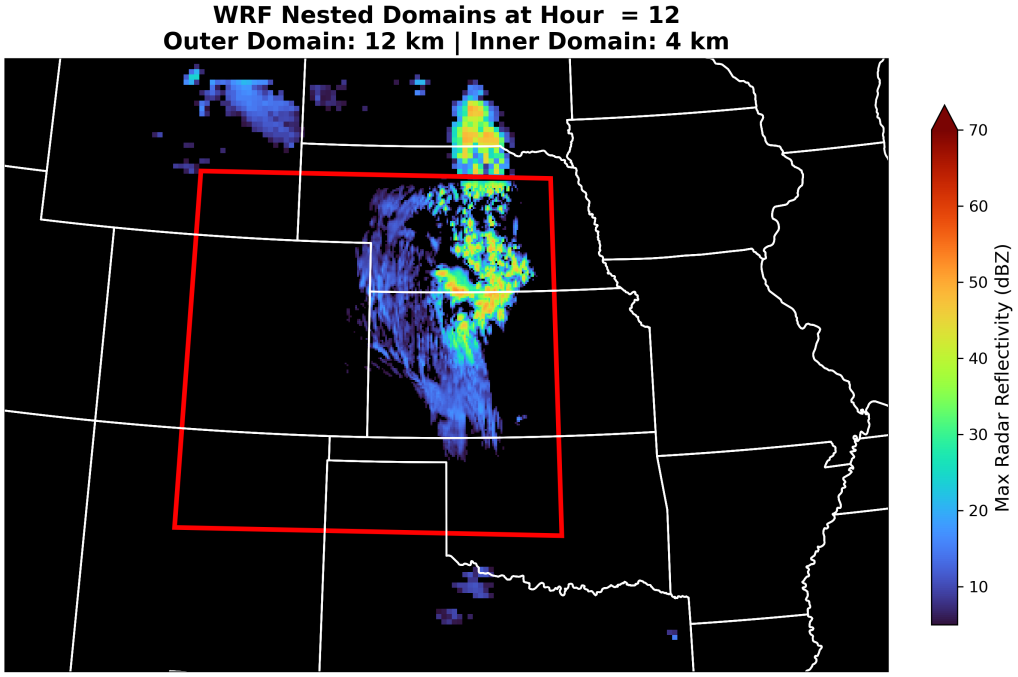


Figure 3.1: Graphic showing the WRF domains for this study. Overlaid with Reflectivity at hour 12 of the Control Climatology run.

3.2.1 Domain Configuration

The Advanced Research Weather Research and Forecasting (WRF-ARW) model was configured with two one-way nested domains centered over Colorado to simulate a severe weather event on 21–22 June 2023. The outer domain, d01, used a horizontal grid spacing of 12 km, while the inner convection permitting domain, d02, employed a grid spacing of 4 km. A grid spacing of 4 km was chosen because it allows deep convection to be partially resolved without reliance on a cumulus parameterization, enabling explicit simulation of convective initiation and storm structure (Weisman et al., 2008, 1997). However, individual convective cells are not fully resolved at this grid spacing and remain partially parameterized, showing the compromise between computational cost and the representation of convection-scale dynamics.

A ratio of 3:1 for the nested domain was chosen due to its performance in topographically complex domains and severe events (Sofokleous et al., 2021). The inner domain was designed to explicitly simulate deep convection and mesoscale boundaries relevant to the initiation of convection.

The domains consisted of 169 × 118 grid points for d01 and 202 × 202 grid points for d02. Both domains employed 50 vertical terrain following sigma levels extending from the surface to a model top of 50 hPa. Vertical resolution was enhanced near the surface using a stretched grid, with a lowest model level thickness of 50 m, to better resolve boundary-layer and land–atmosphere interactions critical for convective development.

A Lambert conformal projection was used, appropriate for mid-latitude regional simulations. One-way feedback between the nested domains was enabled, allowing fine scale features in the inner domain to influence the parent domain. A summary of the important domain structure choices is shown in Table 3.1.

Table 3.1: WRF model configuration used in this study.

Model Setting	**Value**
WRF Version	4.5
Horizontal Grid Spacing	12 km (d01), 4 km (d02)
Vertical Levels	50
Model Top	50 hPa
Time Step	60 s
Inner Domain Time Step	20 s
Simulation Length	42 hours
Initial Conditions	GFS Forecast
Boundary Conditions	GFS (6-hourly)

3.2.2 Physical Parameterizations

In the namelist file from WRF, the forecast integration was set for 42 hours with the start date being 0000 UTC on 21 June 2023, and the end time being 1800 UTC on June 22nd, 2023 (1200 MDT on 22 June in local time). This period allowed sufficient spin-up time prior to convection

initiation and coverage of the full diurnal convective cycle. Additionally, for these experiments the `nwp_diagnostics` parameter was turned on to give output variables for reflectivity, updraft helicity, CAPE, and CIN.

The Weather Research and Forecasting (WRF) model was configured using the CONUS physics suite. This configuration employs the Thompson aerosol microphysics scheme, the Yonsei University (YSU) planetary boundary layer scheme, the Noah land surface model, and the MM5 similarity surface layer scheme. Radiative processes were represented using the Rapid Radiative Transfer Model for GCMs (RRTMG) for both shortwave and longwave radiation. Convection was parameterized using the Grell–Freitas cumulus scheme in the 12 km parent domain, while convection was explicitly resolved in the 4 km nested domain. A summary of the parametrization schemes can be seen in Table 3.2.

Table 3.2: Physical parameterization schemes used in the WRF simulations.

Model Process	**Parameterization Scheme**
Microphysics	Thompson Aerosol-Aware Scheme (Thompson and Eidhammer, 2014)
Planetary Boundary Layer	Yonsei University (YSU) Scheme (Hong et al., 2006)
Surface Layer	MM5 Similarity Surface Layer Scheme (Jiménez et al., 2012)
Land Surface Model	Noah Land Surface Model (Chen and Dudhia, 2001)
Shortwave Radiation	RRTMG Scheme (Iacono et al., 2008)
Longwave Radiation	RRTMG Scheme (Iacono et al., 2008)
Cumulus Parameterization	Grell–Freitas Scheme (12 km domain only) (Grell and Freitas, 2014)

3.2.3 Initial and Boundary Conditions

WRF simulations were initialized and forced using analysis data from the Global Forecast System (GFS). The GFS is a global numerical weather prediction model operated by the National Centers for Environmental Prediction (NCEP) that provides atmospheric analyses and forecasts on a regular latitude/longitude grid (NCEP, 2004). The dataset used in this study had a horizontal resolution of approximately 0.25°and included atmospheric variables on multiple pressure levels and various land surface fields all of which are necessary for WRF initialization.

Initial atmospheric and land surface conditions for the simulations were taken from the 0000 UTC 21 June 2023 GFS. Boundary conditions were updated every 6 hours using subsequent GFS analyses, consistent with the forcing interval specified in the WRF configuration. The data was then processed using the WRF Preprocessing System (WPS), which includes the programs `geogrid`, `ungrib`, and `metgrid` to interpolate the global analysis fields to the model domains. The `real.exe` program was then used to vertically interpolate these fields to the WRF terrain and generated the `wrfinput` and `wrfbdy` files used for model initialization.

3.3 Case Study Overview: 21 June 2023 Severe Weather Event

The convective event examined in this study occurred between 21-22 June 2023 and produced widespread severe weather across eastern Colorado and the central high plains. During the afternoon and evening hours, numerous supercells and clusters of organized convection pop-corned up along the Front Range before propagating eastward into the High Plains. These storms produced large hail, damaging winds, and several tornadoes. In Washington County alone, approximately 37 tornadoes were documented, with 27 of these produced by a single slow-moving supercell thunderstorm. Several of these tornadoes reached significant intensities, with at least three rated EF2 and characterized by peak winds of around 118 mph. One of the most significant tornadoes was rated EF3 and occurred near Granada, Colorado. Additional severe storms produced large hail across the Denver metropolitan area, including a notable high impact cell near the Red Rocks Amphitheater that produced approximately 2-inch hail and injured nearly 100 concert attendees (US Department of Commerce, 2024). This case is particularly useful for examining land–atmosphere interactions because storm initiation occurred in a region characterized by strong surface heating and heterogeneous land surface conditions along the East side of the Rocky Mountain Range.

3.3.1 Synoptic Setup

The large-scale synoptic environment on this day was very favorable for organized convection. Moderate to strong atmospheric instability was present across eastern Colorado, with Convective

Available Potential Energy (CAPE) values exceeding 3000 J kg^{-1} in the pre-convective environment. Vertical wind shear was substantial, with shear (0-6 km) values of approximately 13-15 m/s, sufficient to support organized supercell convection. Southerly low level flow transported warm, moist air northward from the southern plains into eastern Colorado. The westerly flow aloft provided the shear necessary for the organized storms. In addition, daytime surface heating across the high plains contributed to boundary-layer destabilization. These ingredients supported the development of the intense thunderstorms that eventually rolled into the Nebraska and Kansas.

To look at the synoptic elements in more detail, the pressure level of 500 hPa from the ERA5 reanalysis data was chosen. Within an ingredients-based approach to convection, this level is used to diagnose the presence of large-scale lift. In Fig. 3.2, there is an apparent Western US trough with strong southwesterly flow. The overlay of the absolute vorticity and wind barbs shows the strong potential for ascent towards the regions of cyclonic vorticity advection (CVA). Additional areas for CVA include the minima and maxima of the absolute vorticity over the northeast corner of Colorado. The domain for this project, and specifically Colorado, is east and downstream of the trough with a consistent southwesterly flow which is a good precursor for the rising motion associated with convection, indicating that the ingredient of lift is present in this environment.

Continuing to build the synoptic picture, it is important to take a look at the large-scale moisture transport into the region, not taking the perturbed soil moisture into account. This corresponds to the moisture ingredient within the ingredients-based framework. At the 850 hPa pressure level, the overlay of the specific humidity and wind barbs show the presence of lower level moisture. In Fig. 3.3, there is a distinct moisture field visible as a vertical band as dark blue. The southerly wind barbs crossing this moisture field indicate active moisture advection, with the moisture boundary reaching into Eastern Colorado. Importantly, this moist air is being advected upslope in eastern Colorado, which further contributes to boundary-layer moistening. The path of the synoptic moisture transport here shows that the southerly flow transports moist air from the Gulf into the central Plains ultimately supporting boundary layer moistening and instability, demonstrating that sufficient moisture is available for convection.

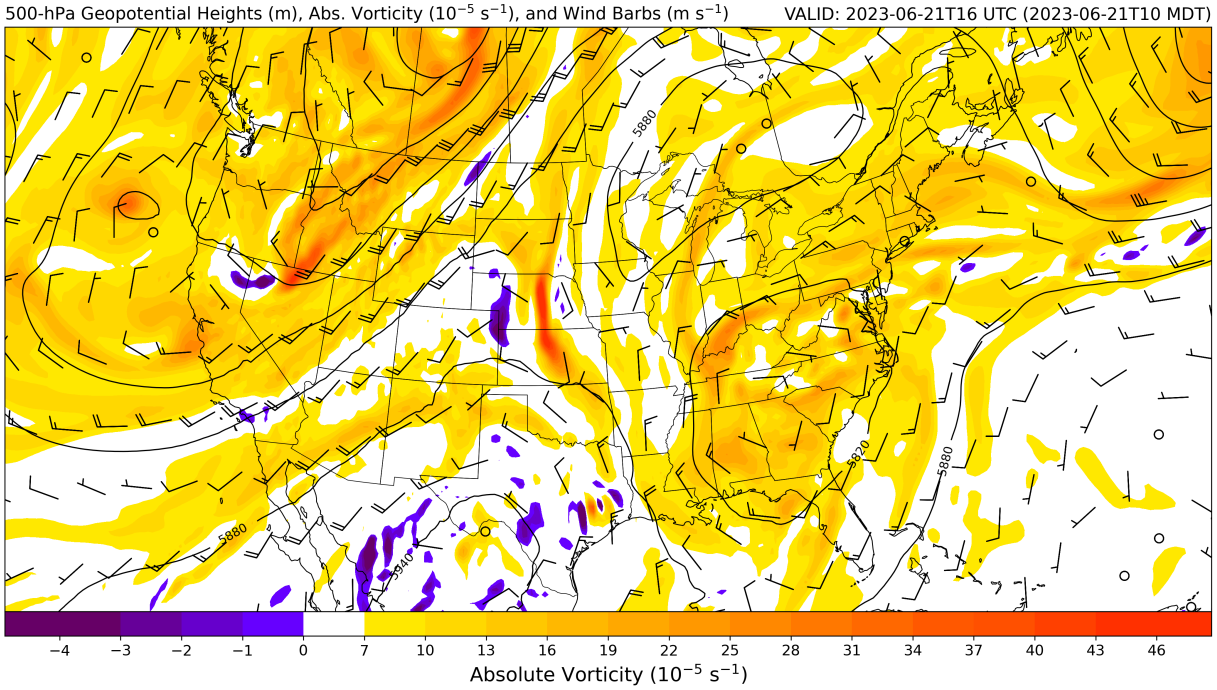


Figure 3.2: ERA5 500 hPa Absolute Vorticity and wind barbs at 16Z, or 1000 MDT, on 21 June 2023

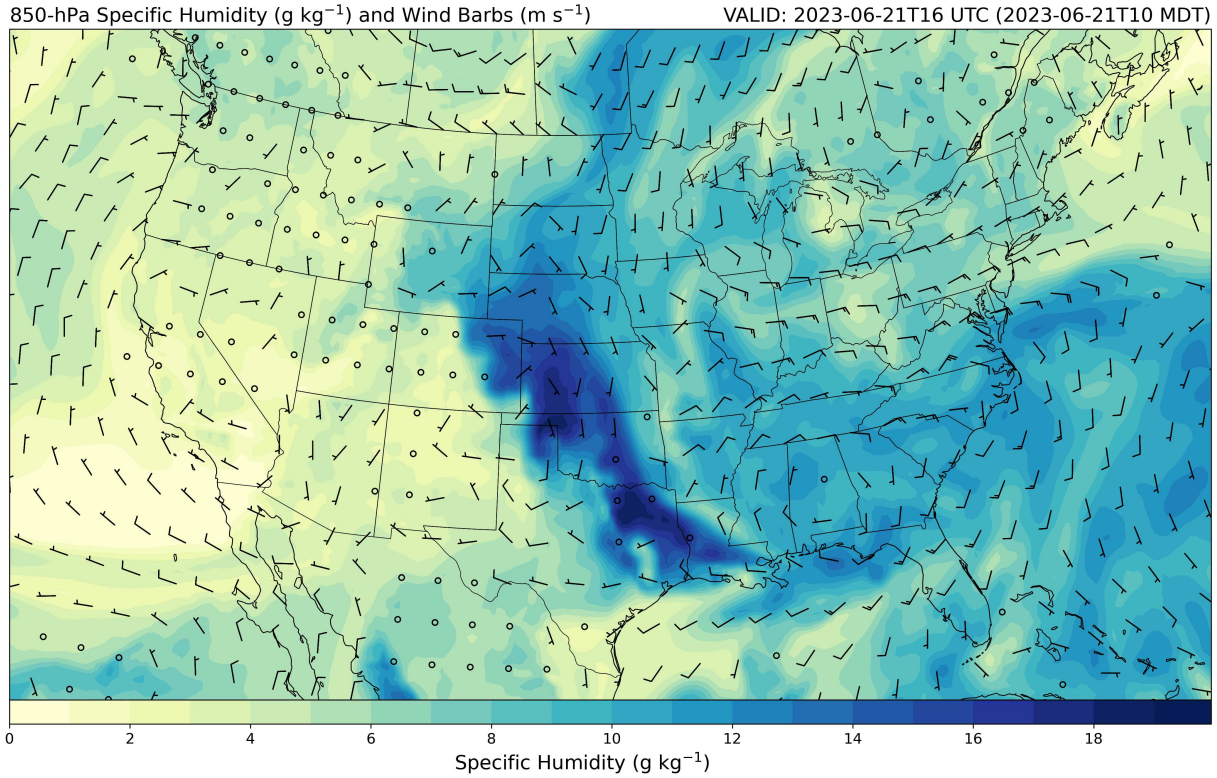


Figure 3.3: ERA5 850 hPa Specific Humidity and wind barbs at 16Z, or 1000 MDT, on 21 June 2023

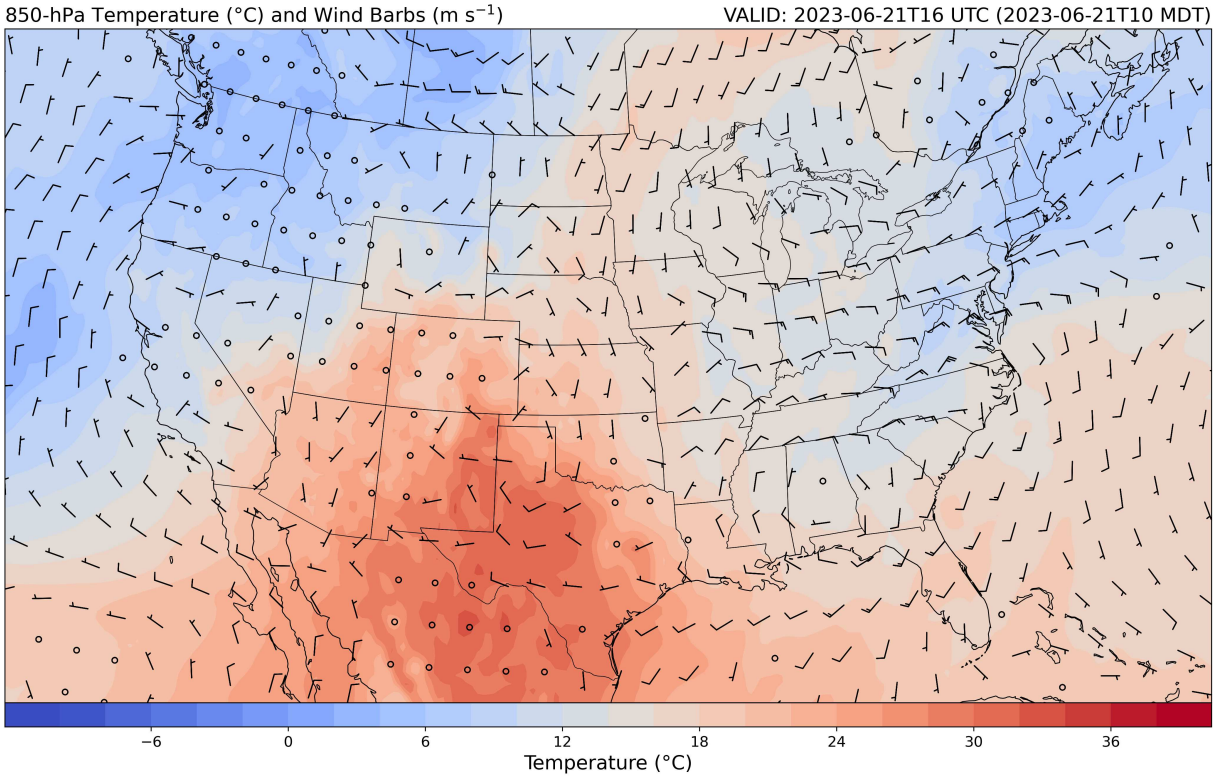


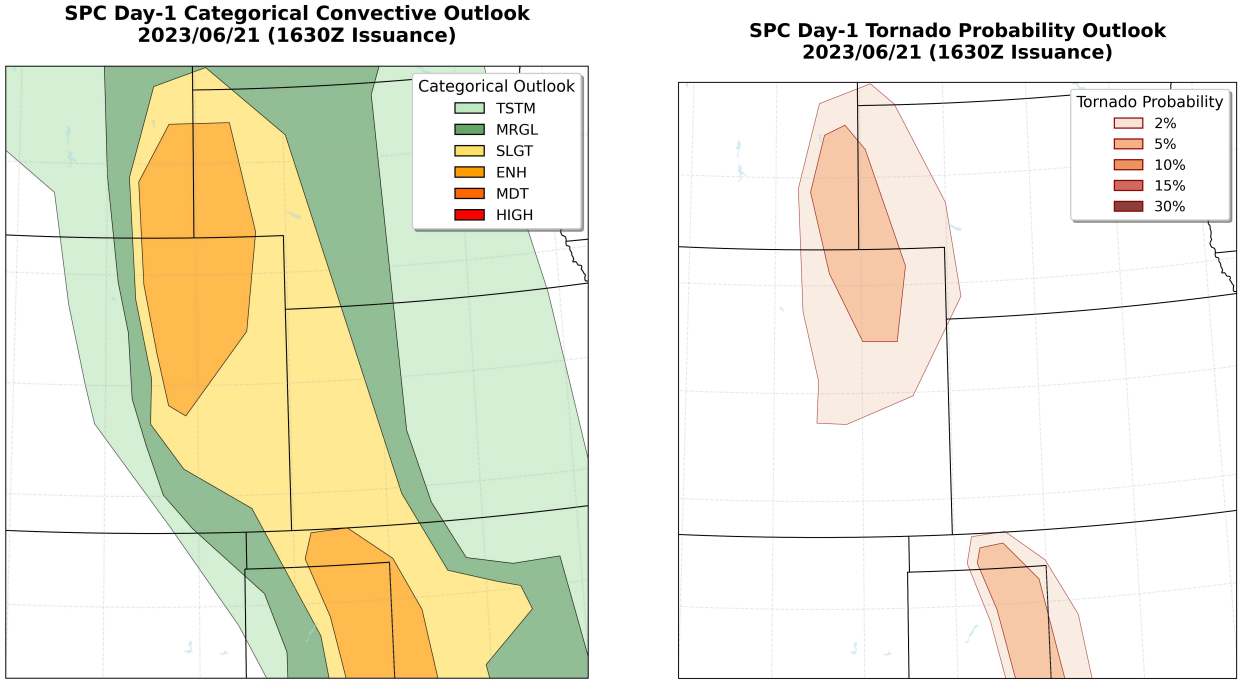
Figure 3.4: ERA5 Temperature advection at 850 hPa at 16 UTC, or 1000 MDT, on June 21st 2023

In Fig. 3.4, the background temperature gradients are shown with the Southwest receiving the warmest temperature. This figure taken in conjunction with the specific humidity moisture transport, shows that the airmass over Colorado has a warm boundary layer and the moisture is being fed into that warm air which is leading to a building of CAPE. Within the ingredients-based approach, this represents the instability component, as the combination of warm temperatures and increasing moisture supports the development of convective available potential energy. Given this favorable large-scale environment, soil moisture can modulate how convection initiates and evolves, by influencing these ingredients through changes in surface fluxes and boundary layer development.

3.3.2 Convective Outlook

The Storm Prediction Center issued its Day-1 Convective Outlook at 1630 UTC on 21 June 2023, which classified an "Enhanced Risk" of severe thunderstorms across numerous portions of the central plains and highlighted the potential for severe weather (Figure 3.5). This outlook

was issued in response to the favorable large-scale environment described above. The Enhanced Risk category indicates a favorable synoptic and mesoscale environment for deep convection, with particular concern for organized supercell activity.



(a) Categorical outlook

(b) Tornado probability

Figure 3.5: SPC Day-1 Convective Outlook issued at 1630Z on 21 June 2023 (Enhanced Risk). Left: categorical severe weather outlook. Right: tornado probability outlook.

3.4 Experiment Design

All WRF simulations shared identical initial and boundary conditions and differed only in their soil moisture fields. The working hypothesis is that imposed soil moisture gradients modify the partitioning of surface sensible (H) and latent (LE) heat fluxes, thereby altering the Bowen ratio. Drier soils favor larger sensible heat fluxes, deeper growth of the boundary layer, and enhanced low level mixing, while wetter soils enhance latent heat flux and suppress daytime boundary layer deepening. Horizontal gradients in surface heating then may induce mesoscale pressure gradients and convergence zones capable of modulating convection initiation timing and location.

3.4.1 Soil Moisture Perturbation Experiments

A suite of idealized WRF experiments were conducted to isolate the role of soil moisture heterogeneity on convection initiation and overall storm development. All simulations share identical atmospheric initial and boundary conditions and differ only in their soil moisture fields. Soil moisture perturbations were applied to all four Noah soil layers prior to model initialization by modifying the climatological soil moisture fields before writing to the WRF input files. Soil moisture gradients were selected to test mechanisms associated with differential surface heating and mesoscale circulations arising from land surface heterogeneity, along with using context from the previous literature.

Soil moisture values in NLDAS are provided in units of kg m^{-2} and were converted to volumetric soil moisture (m^3 m^{-3}) by dividing by the product of layer depth and the density of water (1000 kg m^{-3}). All layers were processed independently; however, the imposed perturbations were applied consistently across all four soil layers to preserve vertical coherence and avoid discontinuities.

The resulting volumetric soil moisture climatology was spatially interpolated to the WRF outer and inner domain grids and inserted into the `wrfinput_d01` and `wrfinput_d02` files generated by `real.exe`. This climatological soil moisture field serves as the control land surface state and represents "typical" June soil moisture conditions over Colorado. All soil moisture processing and manipulation were performed using a Python workflow within a Jupyter Notebook environment. Regridding was performed independently for each WRF domain using a bilinear interpolation, which helped to ensure consistency with the nested domain configuration while preserving the large-scale spatial structure of the climatological soil moisture fields.

Linear gradients were selected because they provide a controlled surface forcing mechanism, allowing for a more clear interpretation of resulting mesoscale circulations. The gradient orientation was chosen relative to the prevailing westerly flow to assess whether convergence develops preferentially along cross flow or along flow heterogeneity boundaries (Tournay, 2016). The

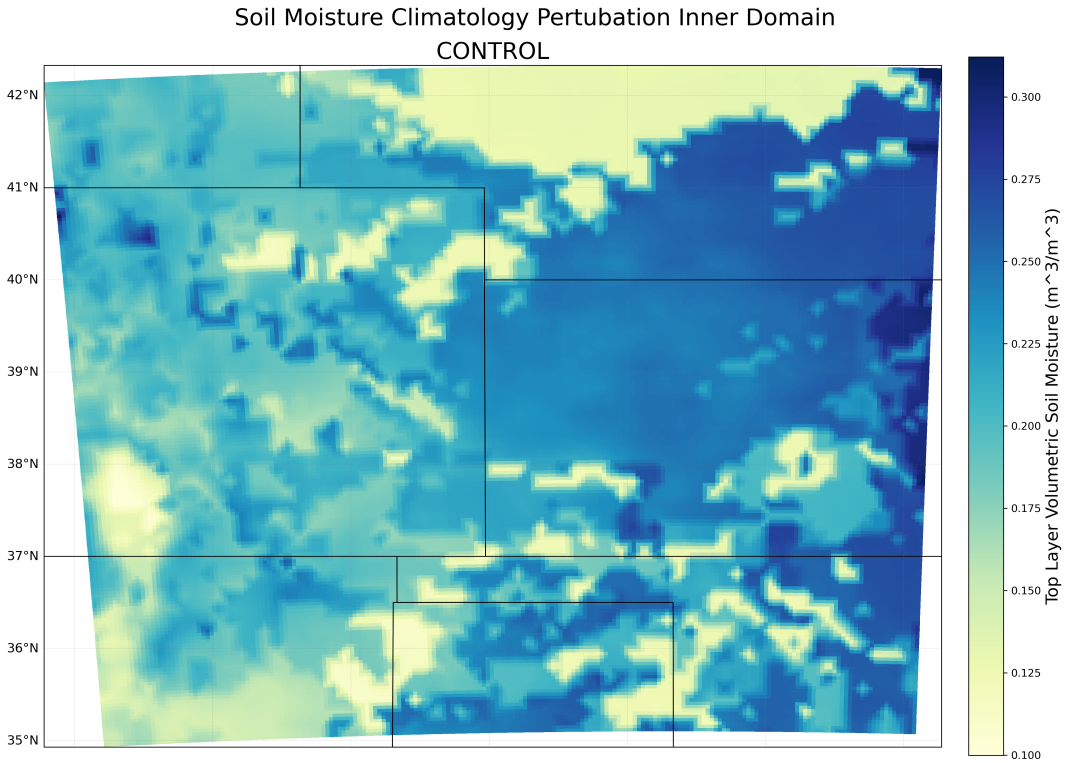


Figure 3.6: Example of the Top Layer of the Climatological Soil Moisture

narrower box variants were designed to increase the rate of soil moisture change (and thereby increasing the magnitude of surface flux gradients).

The climatological maximum and minimum volumetric soil moisture values for each layer were used to define the endpoints of the imposed linear gradients in each experiment, ranging linearly from the minimum value to the maximum value or vice versa at each respective layer 3.6. The imposed soil moisture contrasts fall within the range of observed variability derived from the climatology across the model domain. However, the original soil moisture also exhibits a natural west to east gradient across the region. Conditions are typically quite dry on the leeward side of the Rockies, with soils gradually becoming moister farther east toward the central plains of Colorado. Topographic features that influence this soil moisture distribution are also evident in the natural landscape Fig. 3.7. For example, terrain features such as the Cheyenne Ridge and the Palmer Divide interact with the regional flow to induce dynamically driven features like the Denver Convergence Vorticity Zone (Szoke and Shaw, 1984).

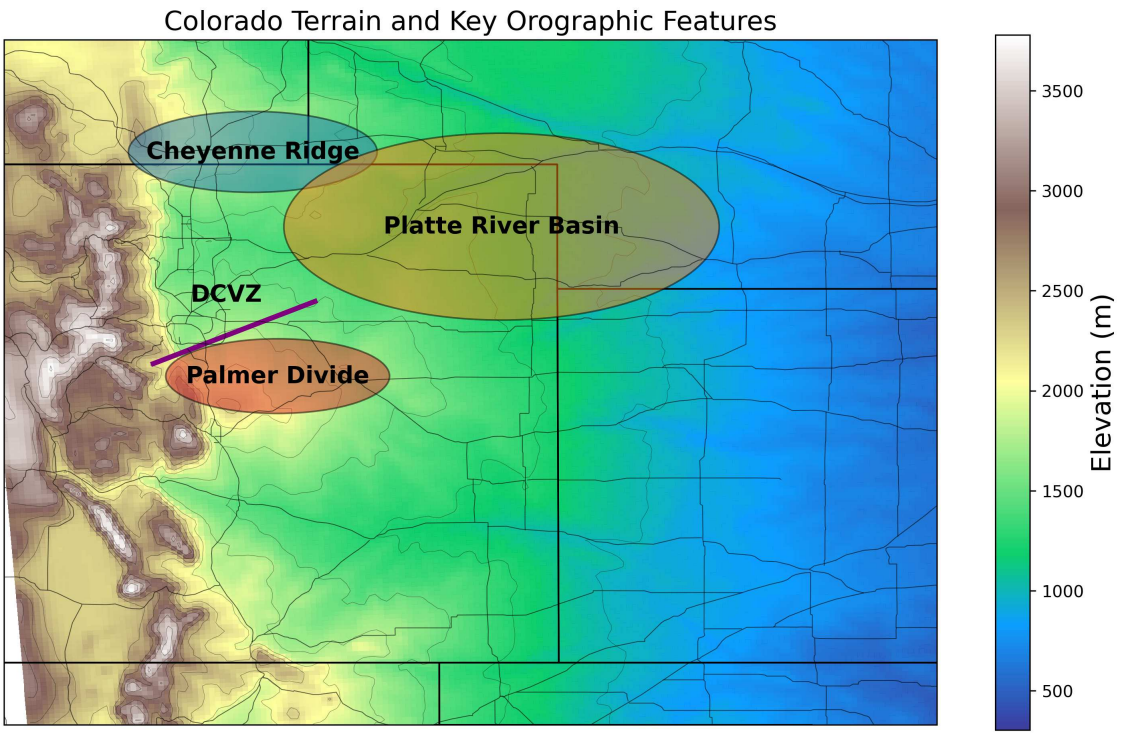


Figure 3.7: Colorado elevation in meters from WRF CONTROL file overlaid with major roads and Key Orographic Features. Including, the Northern Cheyenne Ridge, The Platte River Basin, the Denver Convergence Vorticity Zone, and the Southern Palmer Divide.

These topographic variations also intersect with major hydrological features, including the Platte River basin. Together, these natural land surface characteristics help shape the background soil moisture state across the region at all soil depths. In some of the experiments, the imposed soil moisture perturbation opposes this natural gradient, which may lead to outcomes that may differ from what is expected based solely on the background state. In other simulations, the imposed gradient aligns more closely with the natural west to east tendency, potentially reinforcing the background pattern and amplifying the resulting response relative to more extreme but less physically consistent perturbations.

In the GFS run experiment, the background soil moisture was not altered and used as a baseline to compare the modeling to the observations for this case study. The CONTROL experiment simply ran with the created soil moisture climatology, the climatology that is used as a basis for the subsequent perturbation experiments.

In experiment 1 (referred to as EX_1 WET→DRY), a linear moist to dry soil moisture gradient was imposed over a rectangular region in northeastern Colorado bounded by latitudes 39.0°–41.0°N and longitudes 105.5°–102.0°W.

For each soil layer, volumetric soil moisture values varied linearly from the climatological maximum on the western edge of the box to the climatological minimum on the eastern edge. Linear blending was applied along the box boundaries to minimize sharp discontinuities in soil moisture Fig. 3.8.

A subset experiment (EX_1_2) was conducted using the same gradient orientation as EX_1 but with a reduced longitudinal width. Bounding the box by latitudes of 39.0°–41.0°N and longitudes 104.25°–101.25°W. This experiment isolates the impact of gradient magnitude by increasing the spatial rate of change in soil moisture while maintaining the same range of values.

Experiment 2 (EX_2 DRY→WET) reverses the soil moisture gradient applied in EX_1, with soil moisture increasing from west to east across the same spatial domain. This configuration imposes a soil moisture distribution that contrasts with the typical climatological gradient across the Colorado Front Range, where drier conditions generally prevail east of the mountains due to oro-

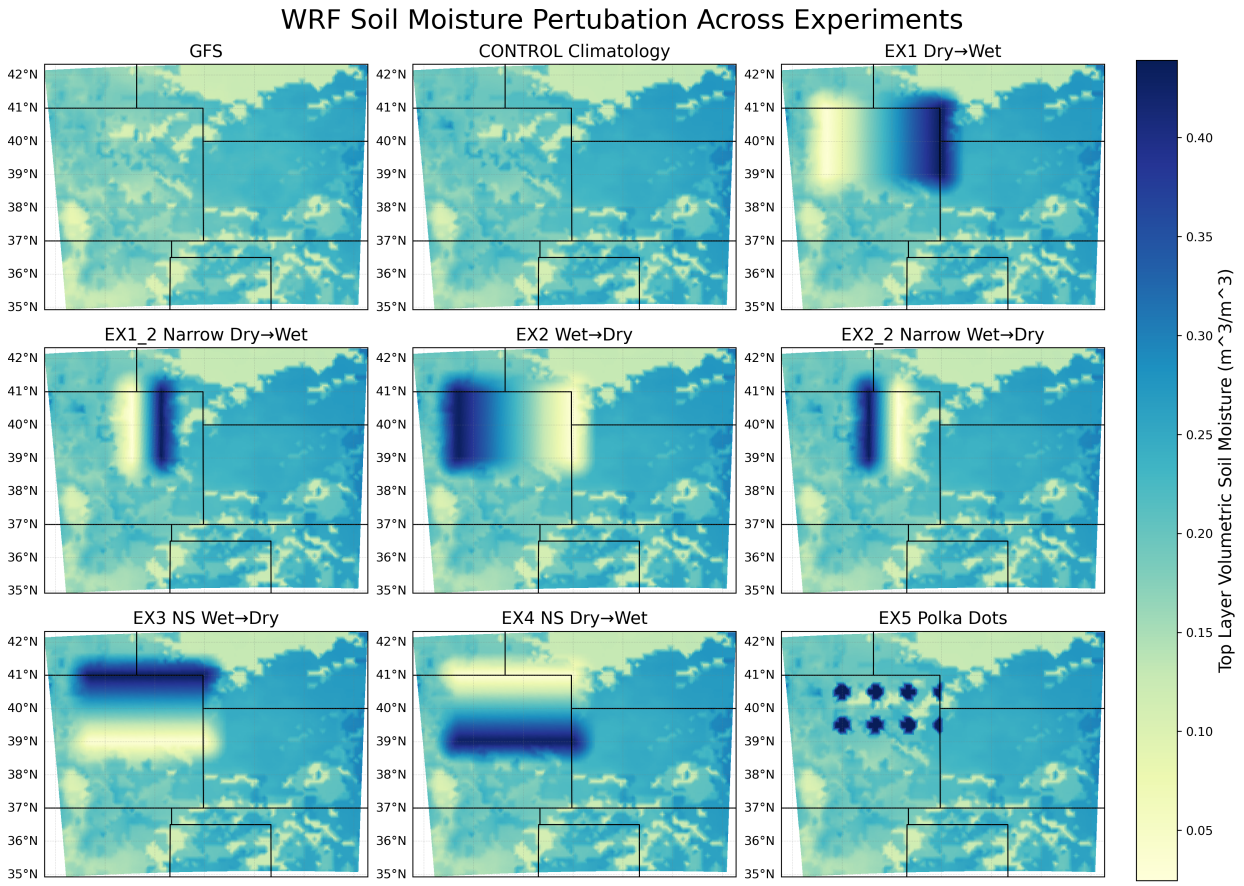


Figure 3.8: Multi-panel Figure showing all the Soil Moisture Perturbation boxes on the top layer of the soil moisture field in WRF for all 8 experiments.

graphic precipitation patterns and regional climate controls. A sharpened-gradient run (EX_2_2) was also performed using a reduced box width to enhance gradient strength.

Experiments 3 and 4 (EX_3 and EX_4) apply linear soil moisture gradients oriented in the meridional direction, spanning north-to-south and south-to-north, respectively. These experiments assess the sensitivity of convective evolution to gradient orientation under predominantly westerly flow conditions.

To approximate the effects of center-pivot irrigation, an additional experiment (EX_5 POLKA DOTS) was conducted in which localized circular regions of enhanced soil moisture were imposed in a repeating spatial pattern. Each irrigated region was represented by an idealized circular feature with a diameter consistent with the horizontal resolution of the WRF domains. While simplified, this configuration captures the spatial heterogeneity associated with irrigated agricultural landscapes in CO. While the imposed irrigation pattern is idealized, it is intended to represent land surface heterogeneity smaller than this scale rather than replicate individual agricultural fields.

3.5 Evaluation Metrics and Analysis Methods

Model performance was evaluated using both temporal and spatial metrics. The initiation of convection was identified in WRF output using simulated composite reflectivity exceeding 40 dBZ and compared against MRMS observations. The threshold of 40 dBZ was chosen off the bases for convective storms (Hubbert et al., 1998). Timing differences and spatial correspondence were assessed across all experiments to evaluate sensitivity to soil moisture perturbations.

In a study utilizing CHILL Radar data, a threshold of 55 dBZ was chosen to look at the development of hailstones. In the figures and analysis, contours were selected ranging from 20 dBZ to 60 dBZ. For this case, the threshold of 40 dBZ was chosen for its ability to fall in between the intensity of convection to be a signature that last throughout the modeling period Hubbert et al. (1998).

There were a total of 9 experiments across 3 different perturbed soil moisture domains. The relative groupings were made to keep the regions or local maximums/minimums together within

the same spatial scale of the altered soil moisture. The resulting analysis was done by grouping as a good way to compare the wet to dry regions, within the same size soil moisture perturbation rectangle. The relative groupings and their respective soil moisture perturbation areas are listed below:

Group	Experiments	LAT/LON Bounds of SM Perturbation
Grouping #1	EX_1, EX_2	[38.3°, 41.7°N], [-106.2°, -101.3°W]
Grouping #2	EX_{12}, EX_{22}	[38.3°, 41.7°N], [-104.8875°, -102.6215°W]
Grouping #3	EX_3, EX_4	[38.3°, 41.7°N], [-106.2°, -101.3°W]

Table 3.3: Experiment groupings based on soil moisture perturbation rectangle.

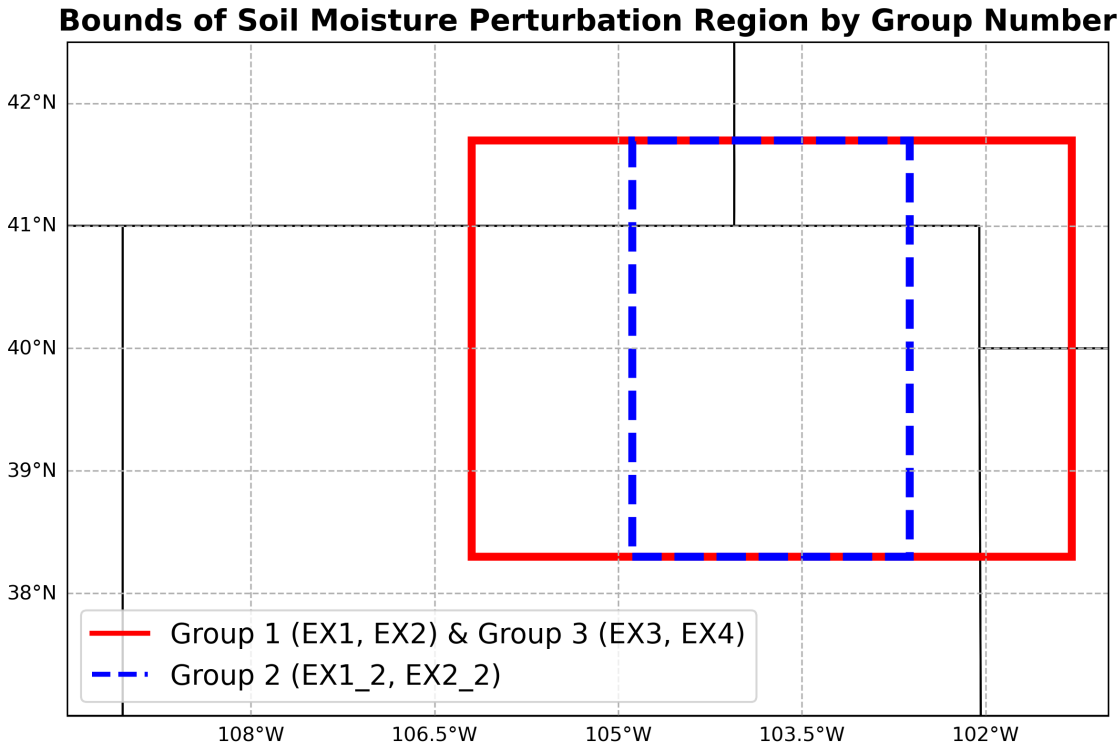


Figure 3.9: Soil Moisture perturbation region used in WRF experiments.

The perturbations were made within a strict box of the Colorado border, but to avoid a sharp gradient from the edge of the domain, there was a linear "fading" effect applied to the edge regions of the domain. Therefore, the bounds of the groupings are made out to include the fade as a way to account for any recorded result over any area different from the control. Within the groupings, comparisons were drawn from the included experiments. A method repeatedly used and will be

seen in the discussion section, is selecting a small box within the altered SM domain and averaging across to analyze. Specifically this method was used to compare the meteorological qualities of the air mass in the hours before and after convection initiation.

As for tracking the cold pools and the differences in the overall storm paths, a derived centroid-based tracking was derived and used in python. The main cells of interest were those that interacted with the altered surface conditions over the domain of perturbation. So, the storm tracking was limited to the bounds of southern Wyoming, Colorado and slightly into Western Nebraska and Kansas and was limited to the main hours of convection and development. The tracking was also restricted to the main hours of convective development (hours 24-36) to focus on the most active storm period.

Within this region, all grid cells exceeding a specified reflectivity threshold of 40 dBZ were identified as being "convective storm pixels". If none of the grid cells exceeded the threshold, then that time step was skipped. On the other hand, when multiple storm objects were present, the largest region by number of grid cells was selected as the "primary" storm feature. To avoid tracking weak convection, this object also had to exceed a minimum size of 100 grid cells. The storm location was then defined using a reflectivity weighted centroid; meaning grid cells with higher reflectivity contributed more strongly to the final position.

This process was repeated at each time step, and the resulting centroid positions were connected in time to form a storm track. While this is a relatively simple tracking approach (rather than a full system tracking algorithm), it provides a good estimate of storm motion during the time window and within the domain. Specifically, it is able to show areas where the convection initiates, holds strong reflectivity signals, and where the system ends at hour 36.

Overall, this simplified method allows for a tailored comparison of storm propagation pathways and timing across the different soil moisture perturbation experiments overlaid with the theta-e perturbations.

3.5.1 Statistical Methods

To quantify the impact of imposed soil moisture gradients, differences between each perturbation experiment and the control simulation were computed for key thermodynamic and dynamical variables. Here X, represents the meteorological variable of interest:

$$\Delta X = X_{\text{experiment}} - X_{\text{control}} \tag{3.1}$$

The difference between the two was then analyzed in the context/units of the respective variable to also find the percent difference from the climatology.

The initiation of convection (CI) timing was defined as the first model hour in which composite reflectivity exceeded 40 dBZ within the imposed soil moisture perturbation region. To assess spatial preferences in CI, the number of grid cells exceeding 40 dBZ was computed separately over the wet and dry subregions of each perturbation rectangle at selected hours surrounding initiation.

Storm intensity was looked at using the total number of grid cells exceeding 40 dBZ as the limit determined for a convective cell. The assessment of storm morphology and organization through time was made qualitatively using composite reflectivity timeseries evolution and potential temperature cold pool evolution. Differences in CI frequency between wet, dry, and control simulations were compared within each experiment grouping to identify shifts in convective preference.

Spatial averages of various thermodynamic and surface variables were computed over rectangular regions corresponding to the wet and dry portions of each soil moisture perturbation experiment.

The thermodynamic structure was evaluated using composite skew-T profiles averaged over grid cells identified by the 40 dBZ reflectivity mask during the primary convective period. The averaging boxes here were selected over regions that were qualitatively picked in spots where strong convection was initiated. The boxes spanned 5 pixels by 5 pixels and the centered latitude/longitude are listed in 3.4. Surface energy partitioning was examined through analysis of sensible heat flux (H), latent heat flux (LE), and the Bowen ratio (H/LE), focusing on the differences between wet and dry perturbation regions.

Grouping	LAT/LON Target of Averaging Box
Grouping #1	[39.33°N, -102.76°W]
Grouping #2	[39.74°N, -103.48°W]
Grouping #3	[41.41°N, -104.91°W]

Table 3.4: Latitude and longitude targets of the averaging box for Skew-T analysis by grouping.

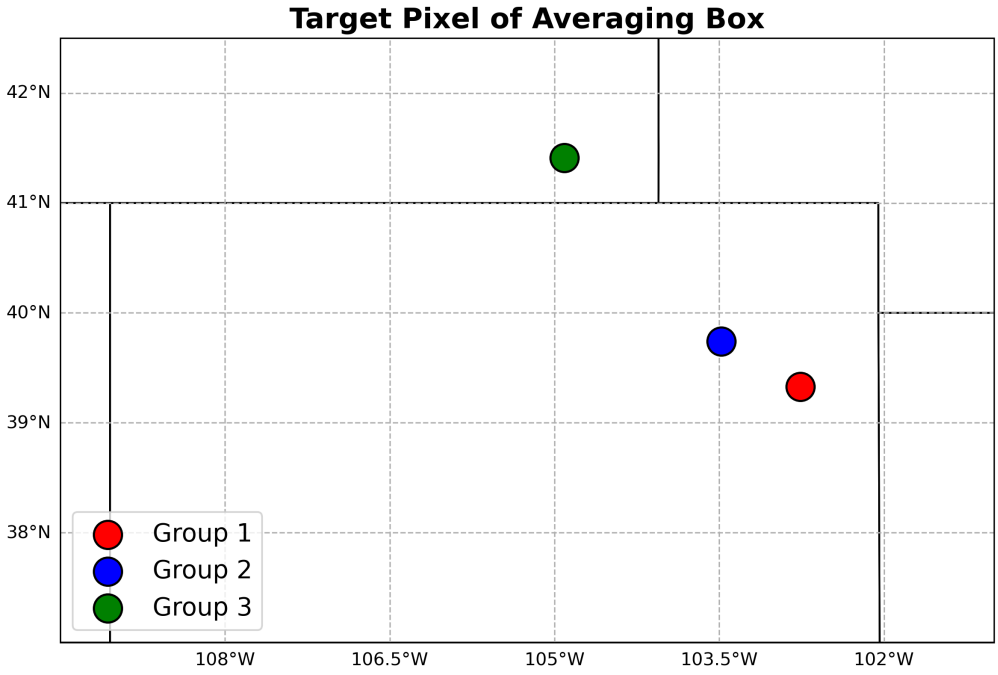


Figure 3.10: Center target pixel of the averaging box used for Skew-T analysis.

Temporal analysis focused on forecast hours 18-36, which encompassed the pre-initiation and mature convection stages. Differences between experiments were evaluated based on the magnitude, spatial coherence, and temporal persistence of responses relative to the control simulation, as reference in the beginning of this section. A response was considered more "robust" when the sign and spatial location of the response were consistent across the different perturbation configurations (West/East and North/South) and persisted for more than one model output time in this case-study.

Because this study examines a single severe weather case using deterministic convection-permitting simulations, formal statistical significance testing was not performed. Instead, this study was evaluated based on the response across experiment groupings, reproducibility between West-/East and North/South configurations, and the physical consistency with established mesoscale dynamics.

Chapter 4

Results

4.1 Overview of Soil Moisture-Atmosphere Response

This chapter discusses how the imposed soil moisture gradient modified the initiation of convection, thermodynamic structure, and storm morphology across all three experiment groupings. The hypothesis here is that the soil moisture gradients, both in their orientation and length, generate differential surface fluxes that change the boundary layer evolution, and ultimately control the timing and location of deep convection.

Across all the experiment groupings, a consistent response is observed... the initiation of convection preferentially occurs over the dry portion of the soil moisture, even though the available moisture at the surface is reduced. This response suggests that there is a dynamical forcing at play that dominates the act of initiating convection among these simulations.

Dry soils reduce the latent heat flux and enhance sensible heat flux, thereby increasing the Bowen ratio and leading to stronger boundary-layer warming. Assuming there is fixed net radiation locally, reduced evaporative cooling requires an increase in the sensible heating through the surface energy balance. The resulting increase in the surface potential temperature deepens the mixed layer and establishes a horizontal temperature gradient between the adjacent wet and dry patches. Through hydrostatic balance, the warmer atmospheric column over the dry region becomes less dense and expands vertically, which then lowers the surface pressure relative to the cooler column over the wet patch. The associated horizontal pressure gradient force drives the low-level flow toward the dry region, producing mesoscale convergence. By mass continuity, horizontal convergence ($\nabla \cdot \mathbf{V} < 0$) is necessarily accompanied by positive vertical motion. This dynamically forced ascent locally weakens the convective inhibition by lifting parcels toward their level of free convection (LFC), and then shows a favoring the initiation of convection over the dry perturbation regions.

In contrast to this, the wet soils enhance the latent heat flux and boundary-layer moisture while suppressing sensible heating. Although there is increased near-surface water vapor mixing ratio (q_v), lowered lifted condensation level (LCL), and possibly increased CAPE, the reduced thermal contrast limits the strength of the hydrostatically induced pressure gradients and associated mesoscale convergence. As a result, the dynamical forcing necessary to overcome convective inhibition is overpowered.

4.1.1 Evaluation of the Climatology against the Observed

It is important to have some real-world validation to these idealized experiments, or at least know the steps to insure the application is trusted for further work. Here, the comparison can be made with the soil moisture climatology run and the actual observations made via radar during the event.

Using data from the NLDAS dataset, the June 2023 soil moisture percentile within the nested domain is shown in Fig. 4.1. During June 2023, much of the Great Plains region exhibited below average soil moisture percentiles, while the North Platte River Basin showed above average values. This spatial pattern differs modestly from the long-term climatology used to initialize the CONTROL run. While the soil moisture for June 2023 falls within the range of the constructed climatology, the spatial heterogeneity of the observed soil moisture distribution alone is sufficient to introduce differences between the climatology and control runs. It is important to note, however, that soil moisture is only one of many factors governing the development of convection. Synoptic forcing, mesoscale boundaries, and the thermodynamic environment of the specific event all contribute to the observed convective response, and are not replicated by a climatological initialization. So, exact agreement between the climatology run and the observed event is not expected, but the comparison between the two helps to contextualize what the model does in a realistic soil moisture regime.

In Fig.4.2, the reflectivity of the the composite MRMS and the GFS run WRF resolution from 2000 MDT, 2300 MDT, and 0200 MDT, show similar shape in the storm's morphology. The major

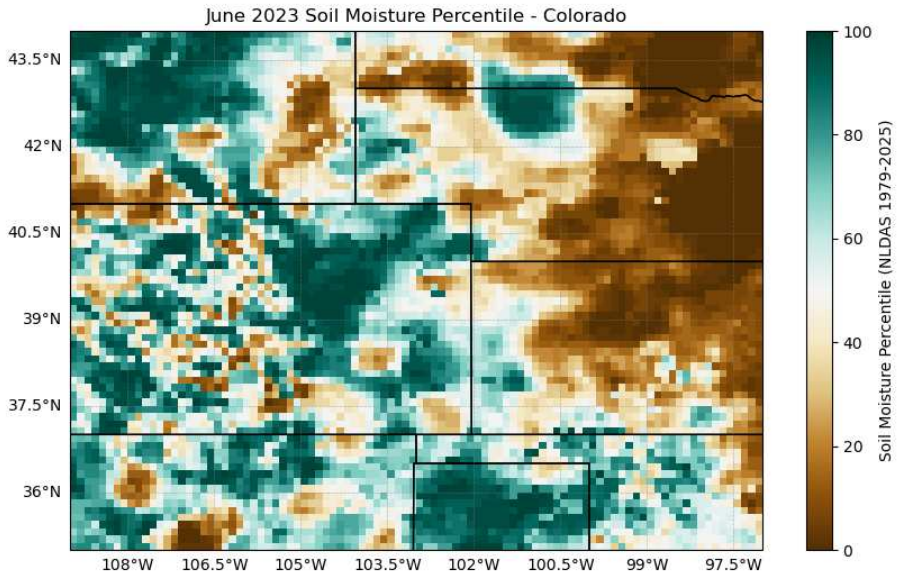


Figure 4.1: NLDAS resolved Soil Moisture Percentile against a climatology created from 1979-2025 across the US in June of 2023

difference are likely due to the difference between MRMS's 1 km resolution and the chose 4 km inner domain WRF resolution. So it is expected that the WRF reflectivity field appears smoother, with the individual convective cells being less resolved and finescale reflectivity structures (bright bands, hail cores) blurred by interpolation to the coarser grid.

In a qualitative comparison of the reflectivity, the areas with the most amount of difference between the observed day and the GFS run are in the Northeastern part of Colorado. There is also a difference in the magnitude of the reflectivity with the WRF runs being consistently more widely spread intense while the MRMS shows a more concentrated intensity. The GFS run produces reflectivity fields that are consistently more widely distributed and spatially extensive than MRMS observations, particularly in northeast Colorado. Maximum reflectivity values remain comparable (both over 60 dBZ), but the GFS run shows a broader swath of mid-level reflectivity (40-55 dBZ) extending further North and East of the primary convective core than observed.

Similarly, Convection initiation occurs at approximately the same time in both the GFS run and observations (around 1500-1600 MDT), suggesting that the large-scale atmospheric forcing and boundary-layer destabilization are well-represented.

To reinforce the validity of the model, it is useful to compare modeled accumulated precipitation against observations. As shown in Fig.4.3, the maximum precipitation magnitude is similar between the two datasets, differing by 16 mm. The spatial distribution shows some differences, with the observations exhibiting a slightly more southern extension of precipitation along the lee of the mountain range. Both datasets capture a diagonal Southeast oriented band of light precipitation extending into western Kansas and northern Oklahoma. However, the observed precipitation displays a more concentrated swath along the lee of the mountains and further South, suggesting that the real storms may have been more tightly organized than the model.

4.1.2 Surface Energy Partitioning using the Bowen Ratio

In WRF's output file there are variables called HFX = "UPWARD HEAT FLUX AT THE SURFACE" and LH = "LATENT HEAT FLUX AT THE SURFACE" and at night HFX $<$0. If there is downward sensible heat flux in WRF that can mean a few things; the surface cooler than air, there is nocturnal stabilization, or the downward turbulent mixing of heat (Sun et al., 2003). The latent heat can be very small during the sunset and when there is a small LH, the Bowen ratio explodes towards infinity. This study is focusing on the pre-convective change in the daytime boundary layer, not nighttime turbulence. So the Bowen ratio at night is not very meaningful, which means the only region of interest as part of the results, is the daytime partitioning of sensible and latent heat release of the surface.

Differences in the surface flux were most apparent during the pre-convective sunlight hours (0600–1900 MST). Following convective initiation and associated cloud development, both the sensible and latent heat fluxes rapidly decreased across all simulations, consistent with reduced surface radiative forcing under cloud cover (Ghausi et al., 2023).

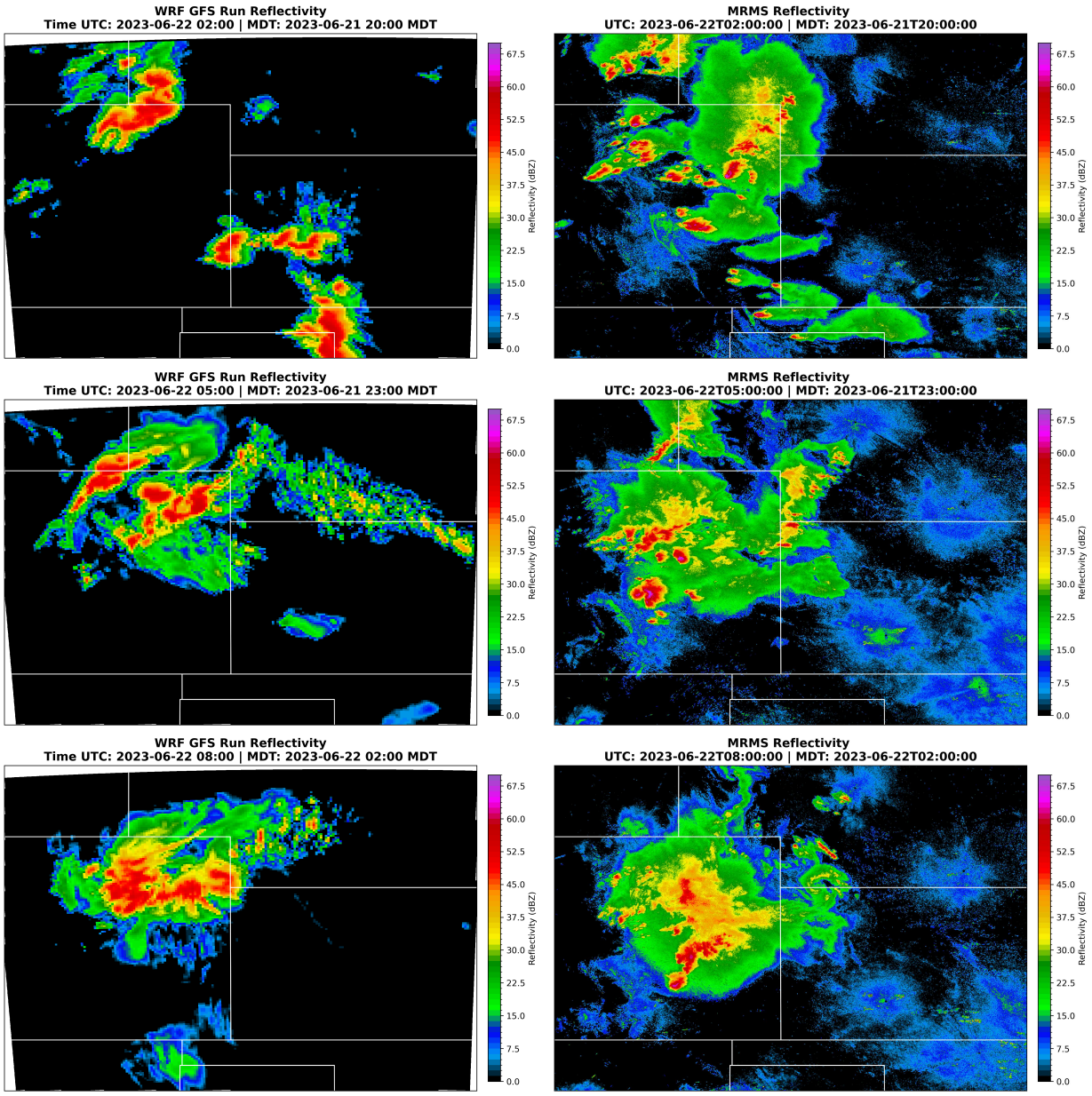


Figure 4.2: Comparison of the reflectivity from the modeled output and observed radar reflectivity at 2000 MDT, 2300 MDT, on June 21st and 0200 MDT on June 22nd, WRF REFD_MAX from the GFS Run (left) MRMS Composite Reflectivity (right)

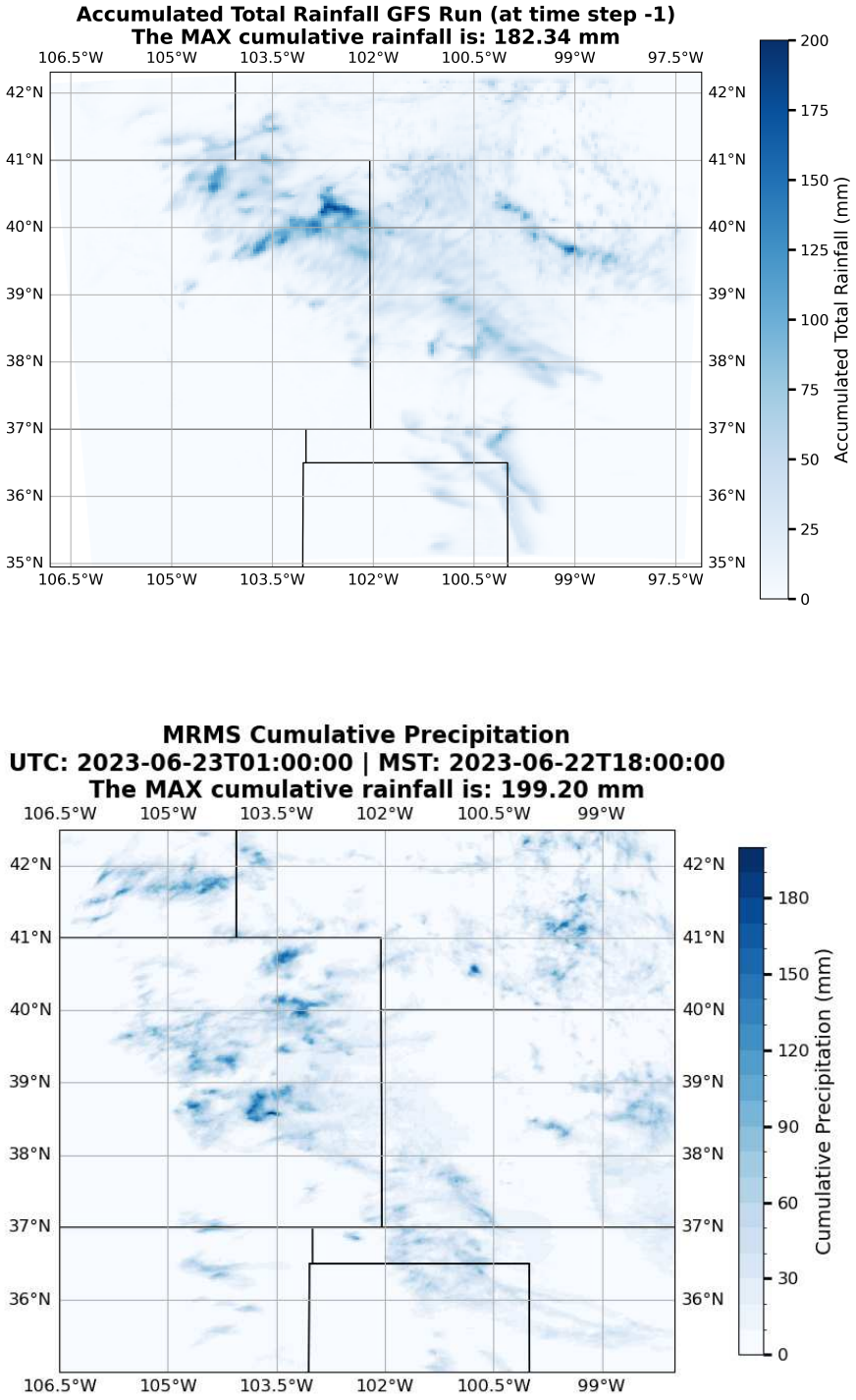


Figure 4.3: Accumulated precipitation (mm) of the GFS run with the GFS soil moisture (left) MRMS observed Cumulative Precipitation in the nested domain (right)

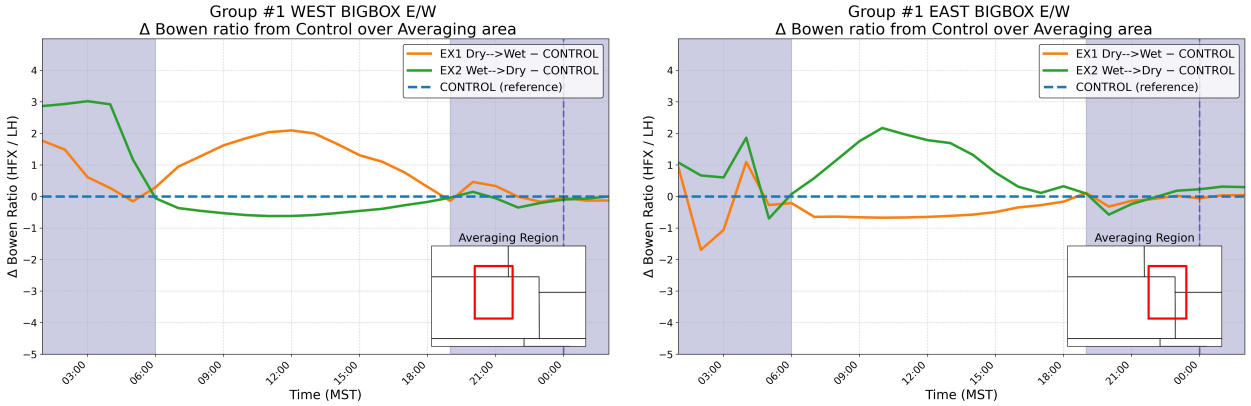


Figure 4.4: Time series of the Bowen ratio (β = HFX/LH) departure from the CONTROL run averaged over the western (left) and eastern (right) sub-regions of the soil moisture perturbation zone for Grouping #1 (E/W gradient, large patch). The zero line corresponds to the CONTROL climatological simulation, such that positive departures indicate a shift toward greater sensible heat flux relative to the control, while negative departures reflect enhanced latent heat flux. Shading denotes nighttime hours (1900-0600 MST), during which the Bowen ratio is not physically meaningful.

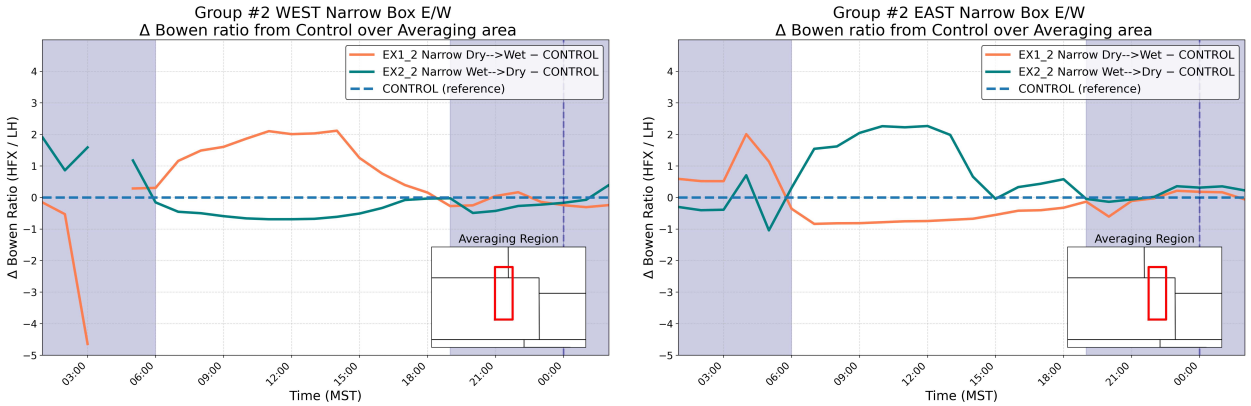


Figure 4.5: As in Figure 4.4, but for Grouping #2 (E/W gradient, narrow patch), averaged over the western (left) and eastern (right) sub-regions.

Figure 4.4, Figure 4.5 and Figure 4.6 show the time series evolution of the domain averaged Bowen ratio for each soil moisture perturbation region relative to the control run. Because the difference from the control run is plotted, positive deviations from the CONTROL line (higher β) indicate that the Bowen ratio is larger than in the climatological soil moisture simulation. This corresponds to a greater proportion of sensible heat flux relative to latent heat flux at the surface. Conversely, when the time series falls below the CONTROL line, the Bowen ratio is reduced

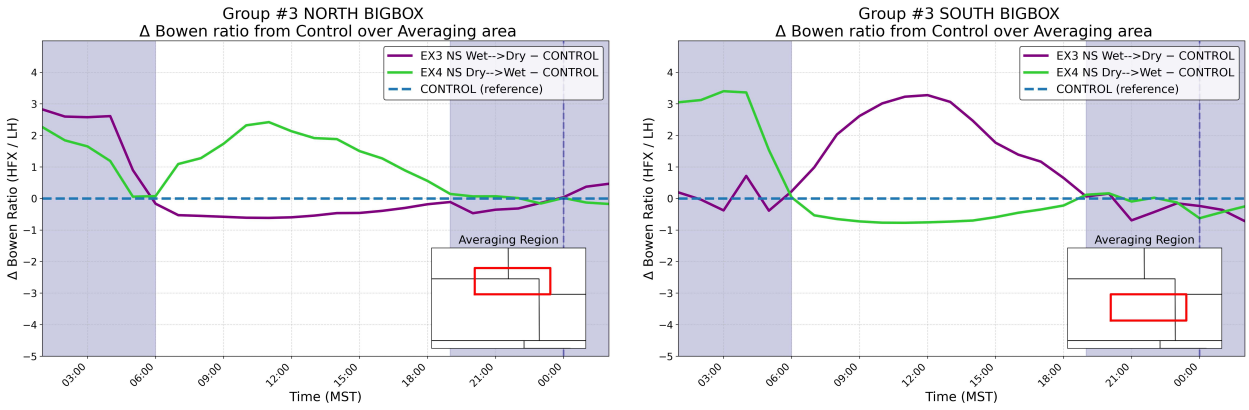


Figure 4.6: As in Figure 4.4, but for Grouping #3 (N/S gradient), averaged over the northern (left) and southern (right) sub-regions.

relative to the control simulation, indicating a larger contribution of latent heat flux compared to sensible heat flux (refer back to Figure 2.1).

Across all experiment groupings the dry perturbation regions exhibit consistently higher Bowen ratios during the daytime hours, reflecting a shift in the surface energy balance toward sensible heat flux. In contrast, wet perturbation regions had lower Bowen ratios due to the enhanced latent heat flux associated with increased soil moisture and evaporative effects.

The largest differences between the groupings occurred during the mid morning into the early afternoon (approximately 1000–1600 MST), when solar radiation and turbulent mixing within the boundary layer are strongest (Stull, 1988). During this period, the dry perturbation simulations produced substantially higher sensible heating (and higher β), leading to a stronger boundary layer warming and more rapid growth relative to the control and wet simulations.

These differences in the surface energy partitioning can strongly influence the evolution of the boundary layer during the day. Higher Bowen ratios over dry soil promote deeper and warmer mixed layers, while lower Bowen ratios over wet soil favor cooler and boundary layers with higher relative humidity. As the mixed layer deepens over the dry perturbation regions, the resulting horizontal temperature gradients can strengthen mesoscale circulations and enhance low-level convergence along the soil moisture boundary region.

The time period of the maximum Bowen ratio separation between experiments occurs several hours prior to the onset of convection initiation (0700-1200 MST). This suggests that land atmosphere interaction during the pre-convective boundary layer growth can play a role in determining where the convective initiation ultimately occurs in the Colorado Front Range.

4.2 The Initiation of Convection

Convection initiation (CI) refers to the onset of deep moist convection, which occurs when a lifted parcel acquires sufficient buoyancy to overcome convective inhibition (CIN) and reach its level of free convection (LFC), thereby releasing the available convective available potential energy (CAPE) stored in the environment. CI is the primary focus of these experiments because land surface conditions, particularly spatial variability in soil moisture, can modify the boundary layer temperature and moisture through differential surface fluxes (covered in the previous section). These modifications influence the strength of mesoscale convergence and the magnitude of CIN, directly affecting whether and where sufficient lifting exists to realize CAPE and trigger deep convective development.

To look at the role soil moisture gradients have in CI, simulated composite reflectivity was analyzed alongside the imposed soil moisture perturbation fields for each experiment grouping. Additional diagnostics, including histograms that relate CI frequency and timing to the soil moisture gradient magnitude. All in an effort to try and quantify the major differences between the wet, dry, and control simulations.

Figure 4.7 summarizes the spatial distribution of convection initiation within the soil moisture perturbation region for each of the experiment groupings. For each case, the number of pixels exceeding a reflectivity threshold of 40 dBZ was computed separately over the imposed wet and dry subregions at four selected hours surrounding the onset of convection. The mean volumetric soil moisture (m^3/m^3) within each subregion is shown in black text at the bottom of the last histogram grouping to provide context for the relative magnitude of the soil moisture contrast.

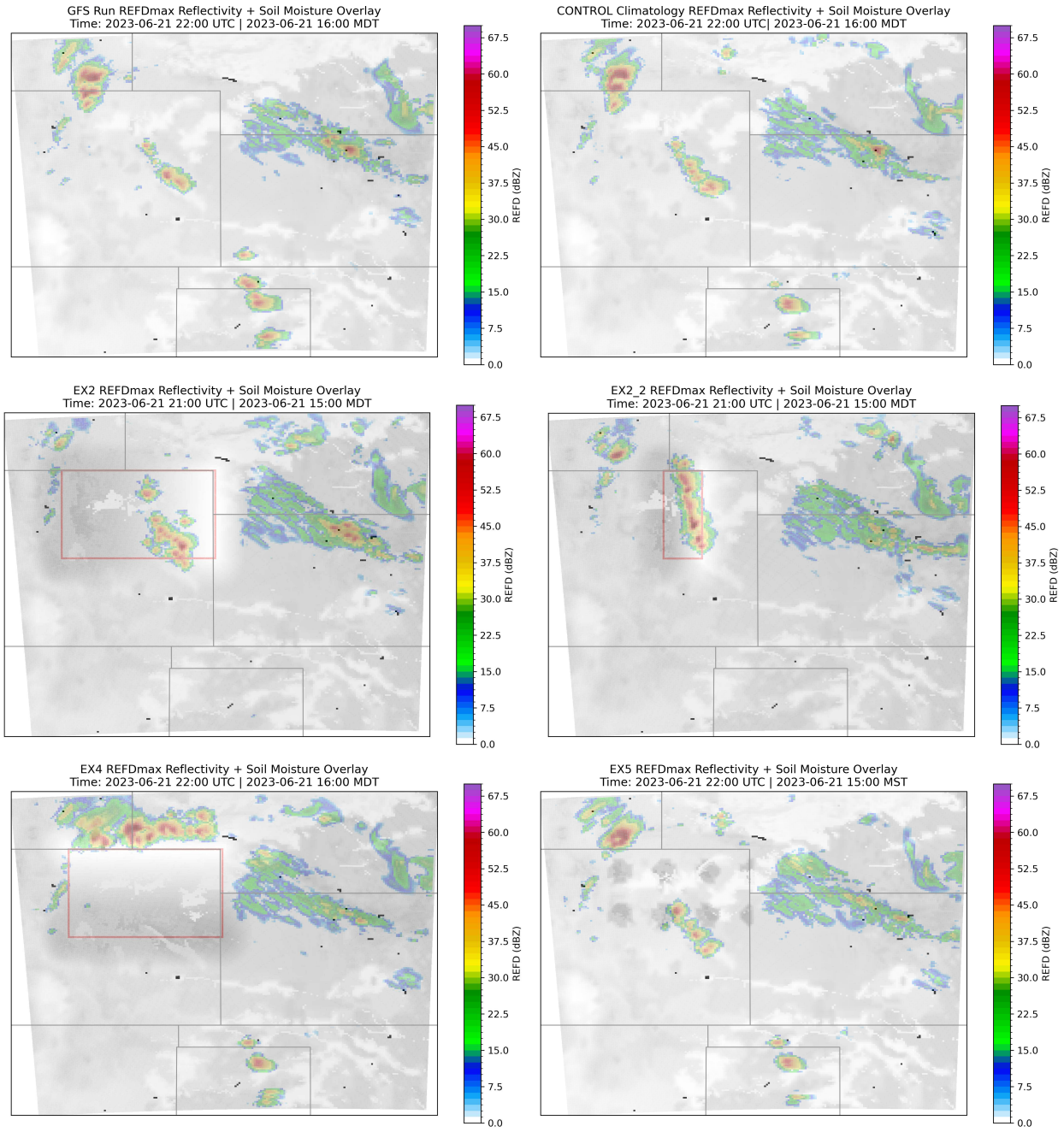


Figure 4.7: Hours of developed convection initiation (1500 MDT or 1600 MDT) overlaid with reflectivity and Soil Moisture gradients from each of the groupings and EX_5

In Fig. 4.7, the GFS run and the CONTROL run show similar reflectivity maps with small differences in the size and magnitude of the initial cells. With the GFS run showing generally a larger number of cells at 1600 MDT, along with the cells being slightly more intense and widespread. However, across all of the perturbation experiment groupings, CI preferentially occurs over or

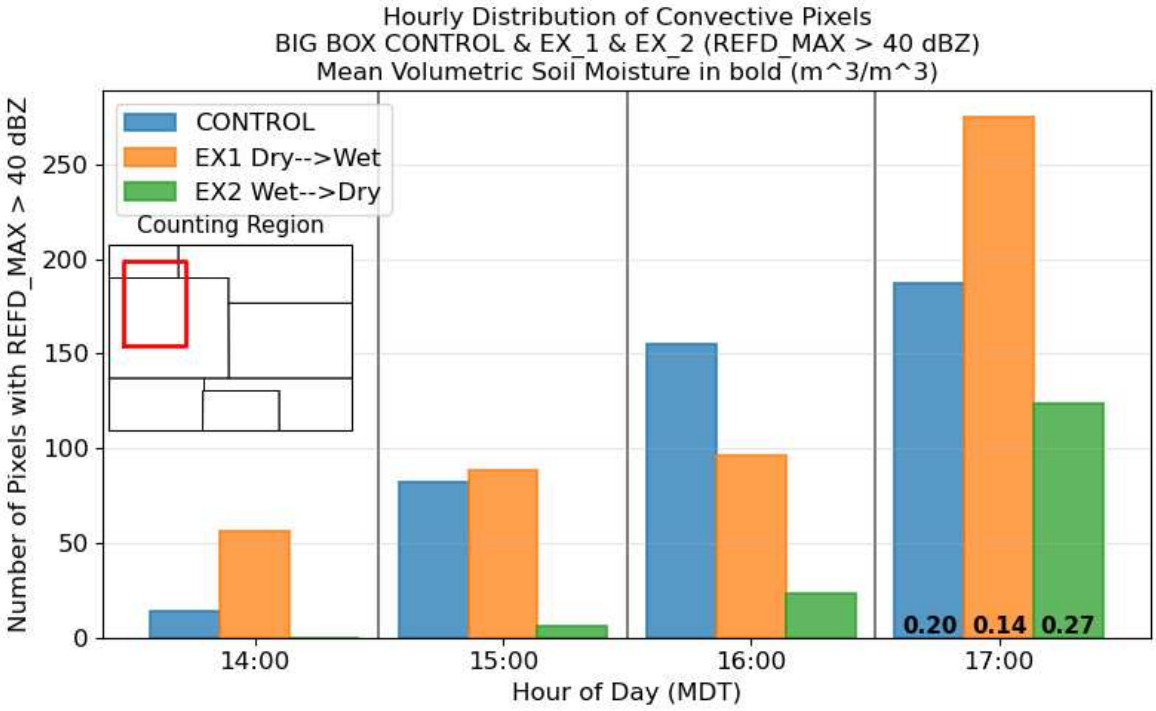
near the dry soil moisture subregion, consistent with the dynamical forcing mechanism discussed previously. In EX_2 (Wet $\rightarrow$ Dry, big box), convection develops earlier and more organized over the dry subregion relative to the control, suggesting that the enhanced sensible heating and resulting mesoscale convergence along the soil moisture boundary are sufficient to overcome CIN and realize CAPE ahead of the control simulation. EX2_2 (Wet $\rightarrow$ Dry, narrow box) shows a similar preference for CI over the dry region, though the signal is somewhat weaker, consistent with the reduced spatial scale of the forcing and the smaller Bowen ratio departures seen in Grouping #2.

In EX_4 (North/South, Dry $\rightarrow$ Wet, big box), the preferred CI location shifts accordingly with the orientation of the gradient, further supporting the role of the soil moisture boundary in anchoring where CI occurs. EX_5 (Polka Dots) produces a more spatially diffuse convective response, wherein multiple small dry patches each generate localized convergence over the 4 hours, resulting in a broader distribution of CI locations compared to the previous patch experiments. Relative to the control run, all of the perturbation experiments show either earlier initiation, a greater number of convective pixels over the dry subregion, or both.

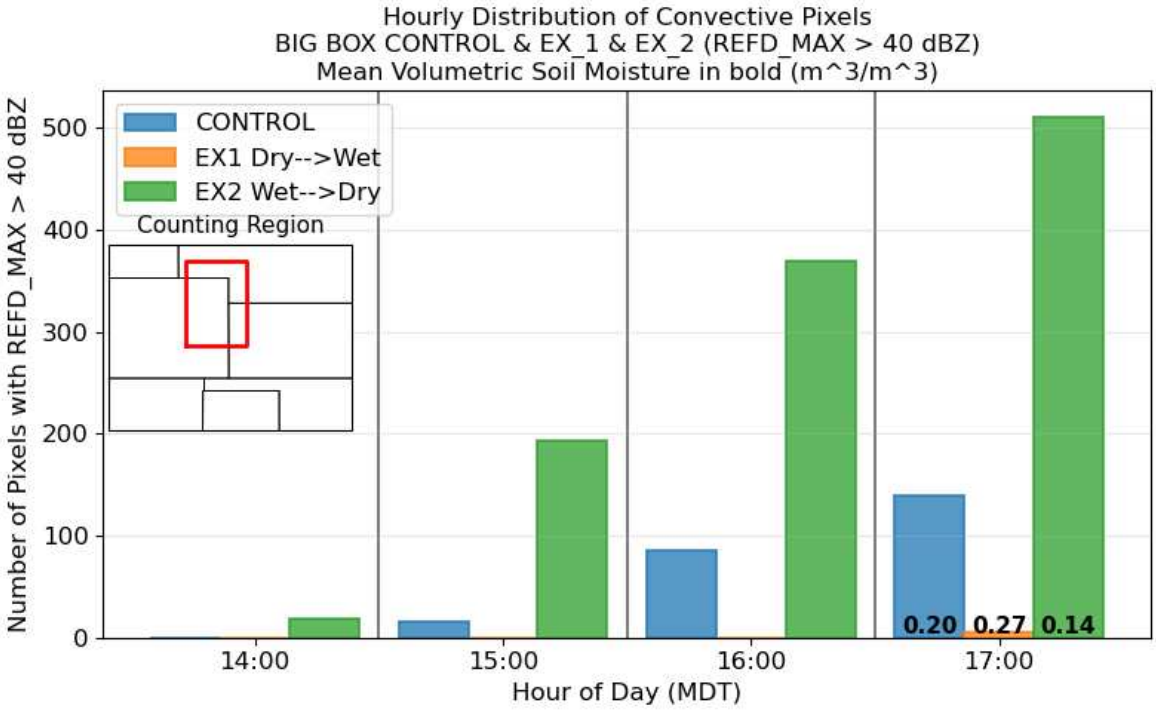
Figure 4.8 shows the West and East configurations for Group 1, or the large rectangle. Across all four analyzed hours, the distribution of pixels > 40 dBZ is consistently skewed toward the dry perturbation rectangle in both the East and the West. Despite the dry region having lower mean soil moisture than the wet rectangle, this analysis indicates that CI preferentially occurred over the unnaturally dry portion of the imposed gradient for grouping #1.

The preference for CI over the dry subregion persists across both the selected West and East domains, suggesting that the result is not tied to a single location or storm track. Instead, the response appears robust to the placement of the soil moisture perturbation and is consistent with a mechanism in which the enhanced sensible heating over the dry patch strengthens mesoscale convergence and reduces convective inhibition locally.

Figure 4.9 shows a similar response to Group 1, but with a narrower soil moisture perturbation region and a reduced model domain (half the size of Group 1). This configuration was designed to

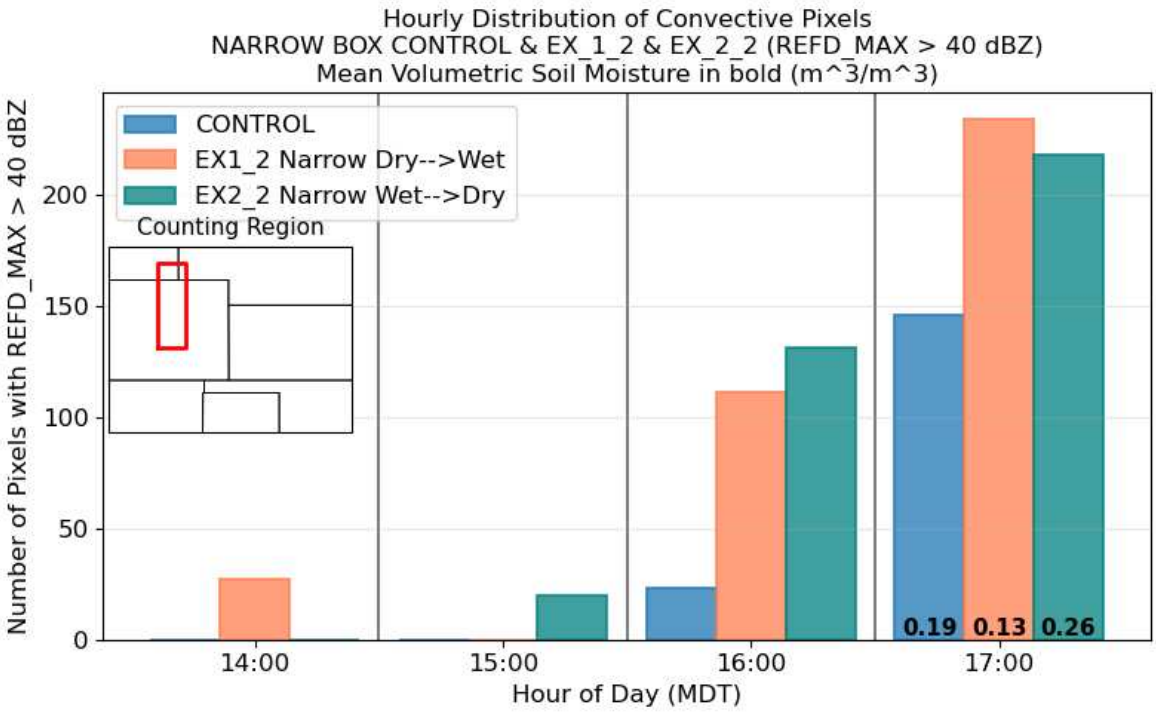


(a) West configuration.

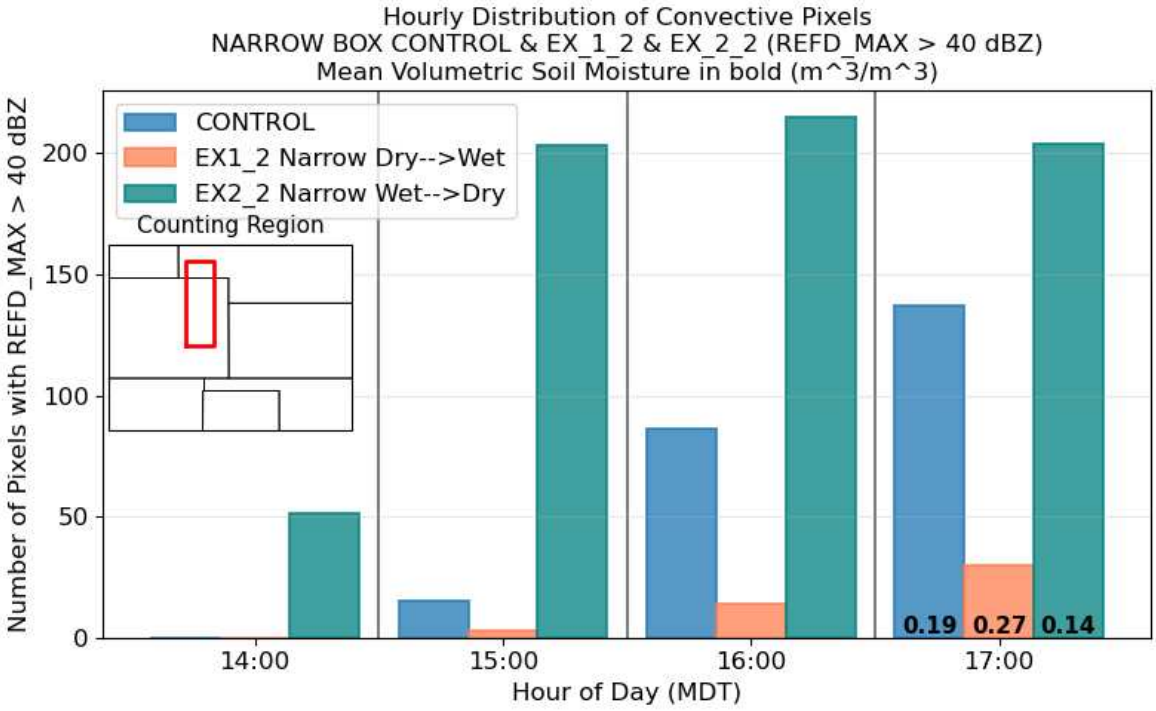


(b) East configuration.

Figure 4.8: Convective initiation diagnostics for Group 1. Histograms show the number of pixels exceeding 40 dBZ over the wet and dry soil moisture perturbation rectangles at four selected hours. Mean soil moisture in each rectangle is shown beneath each panel.



(a) West configuration.



(b) East configuration.

Figure 4.9: Convective initiation diagnostics for Group 2 (E/W gradient, narrow patch). Histograms show the number of pixels over 40 dBZ over the dry and wet soil moisture perturbation, for West(top) and East(bottom) configurations. Mean volumetric soil moisture within each subregion is shown in black.

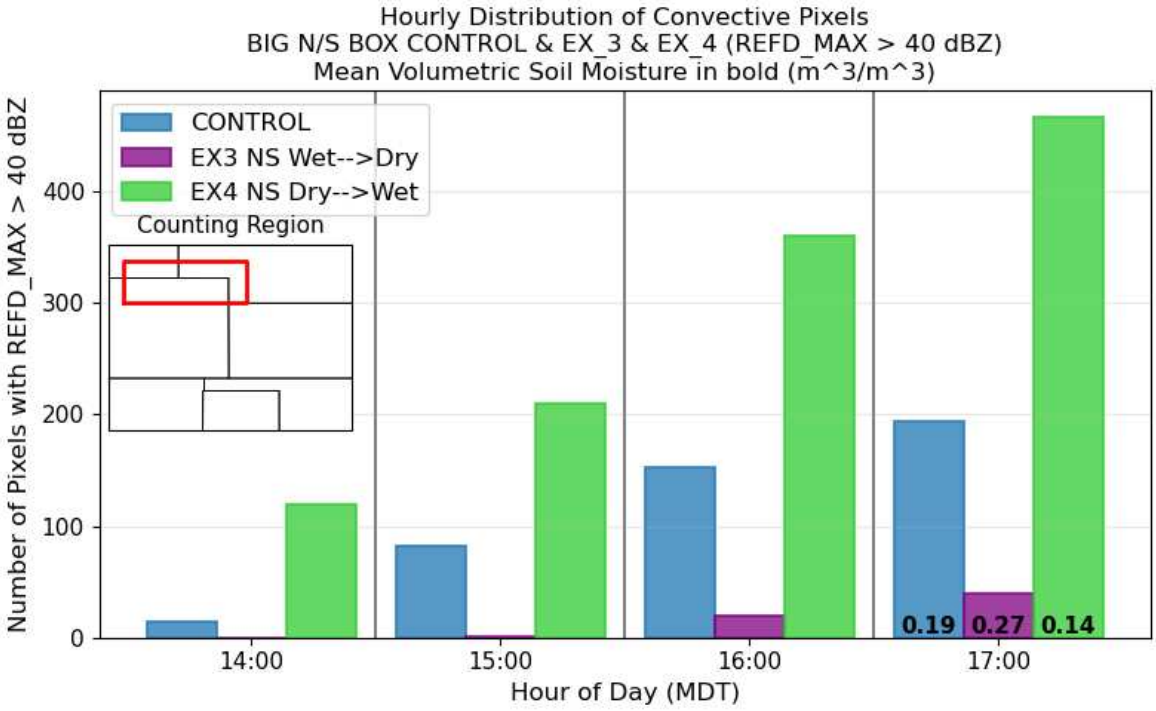
test whether changes in the soil moisture gradient magnitude and spatial scale produce a predictable change in the intensity and spatial distribution of convection.

Although the total number of pixels exceeding 40 dBZ is reduced relative to Group 1, the same overall pattern is evident: high-reflectivity pixels occur more frequently over the dry perturbation region than over the wet region. The control simulation generally falls between the dry and wet cases, indicating that the imposed soil moisture heterogeneity systematically shifts convective initiation toward the dry subregion.

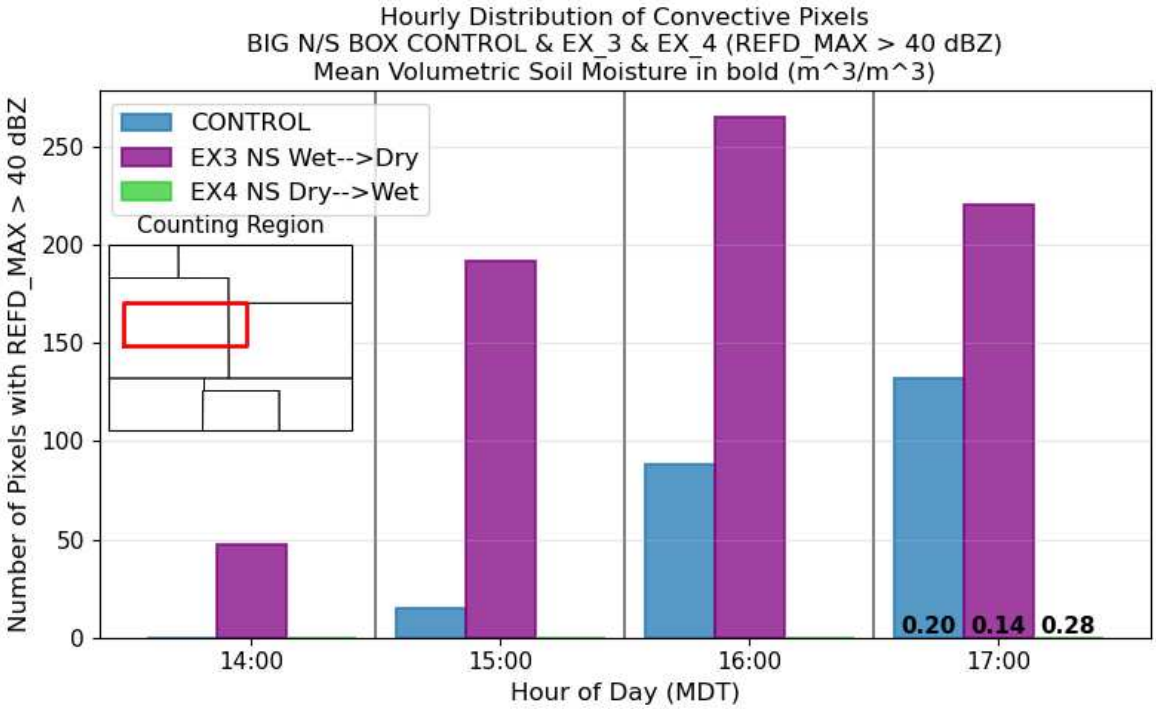
A comparison between the West and East configurations suggests differences in the timing of convective development. The West configuration exhibits a greater number of pixels > 40 dBZ later in the simulation period, whereas the East configuration shows elevated counts earlier in the day. This timing offset reflects differences in the evolution of convective inhibition across the two configurations, which can alter when the imposed surface forcing becomes sufficient to trigger deep convection.

Figure 4.10 presents the North and South configurations for Group 3, where the soil moisture gradient is oriented meridional rather than zonally. Despite the change in gradient orientation, the preferential CI signal over the dry subregion is maintained. The control simulation again falls between the dry and wet perturbation cases, consistent with the pattern established in Groupings #1 and #2. The consistent response across different gradient orientations suggests that the mechanism anchoring CI to the dry subregion (the differential sensible heating and the resulting mesoscale convergence) is not sensitive to the orientation of the soil moisture boundary relative to the large scale flow.

Across all three experiment groupings and spatial configurations, CI is consistently favored over the dry soil moisture subregion despite its reduced moisture availability. The control simulation consistently falls between the dry and wet perturbation cases in terms of the convective pixel count. This confirms that the imposed soil moisture heterogeneity is the primary driver of the shifts in CI location. Taken all together, these results indicate that the dominant control on CI is not simply the availability of boundary layer moisture, but rather the dynamical response to surface



(a) North configuration.



(b) South configuration.

Figure 4.10: Convective initiation diagnostics for Group 3 (N/S gradient). Histograms show the number of pixels exceeding 40 dBZ over the dry and wet soil moisture regions, for the North (top) and South (bottom) configurations. Mean volumetric soil moisture within each subregion is shown beneath each panel.

heterogeneity. And specifically, the differential sensible heating that drives mesoscale convergence along the soil moisture boundary and provides the lifting necessary to realize CAPE and overcome CIN.

4.3 Convective Available Potential Energy & Inhibition

Convective Available Potential Energy (CAPE) and Convective Inhibition (CIN) represent the thermodynamic potential for, and resistance to, deep convection. These metrics are used here to assess how land–atmosphere interactions associated with soil moisture perturbations can modify atmospheric instability and the likelihood of convective initiation across the experiment simulations. CAPE represents the vertically integrated buoyant energy available to an air parcel lifted from the boundary layer to its level of neutral buoyancy. CIN represents the negative buoyant energy that must be overcome for a parcel to reach its level of free convection (LFC).

To diagnose the thermodynamic mechanisms associated with the soil moisture perturbations, composite skew-T log-p profiles were constructed for each experiment and analyzed by grouping.

Across Grouping #1 (Figures 4.11, 4.12, and 4.13), at 1000 MDT, the area-averaged skew-T profiles reveal clear thermodynamic differences consistent with the imposed soil moisture perturbations. The dry perturbation experiment (EX_2 Wet$\rightarrow$ Dry) exhibits the warmest near surface temperature (23.5°C) and lowest relative humidity (71.4%), producing the lowest LCL (792 hPa) and the highest CAPE (3350 J/kg) with the weakest CIN (-19 J/kg) of the three experiments. In contrast, the wet perturbation (EX_1 Dry$\rightarrow$ Wet) shows a cooler, more moist boundary layer (T2m_2m 2m = 20.8°C, RH = 87.3%), a higher LCL (831 hPa), reduced CAPE (3059 J/kg), and stronger CIN (-38 J/kg), consistent with evaporative cooling and boundary layer moistening suppressing thermal instability. The CONTROL falls between the two perturbation cases across all diagnostics (CAPE = 3175 J/kg, CIN = -27 J/kg, LCL = 803 hPa). Notably, despite the dry experiment having the lowest near-surface moisture, it produces the highest CAPE and weakest CIN, indicating that the enhanced sensible heating and deeper mixed layer more than compensate for the reduced boundary layer moisture in terms of thermodynamic instability.

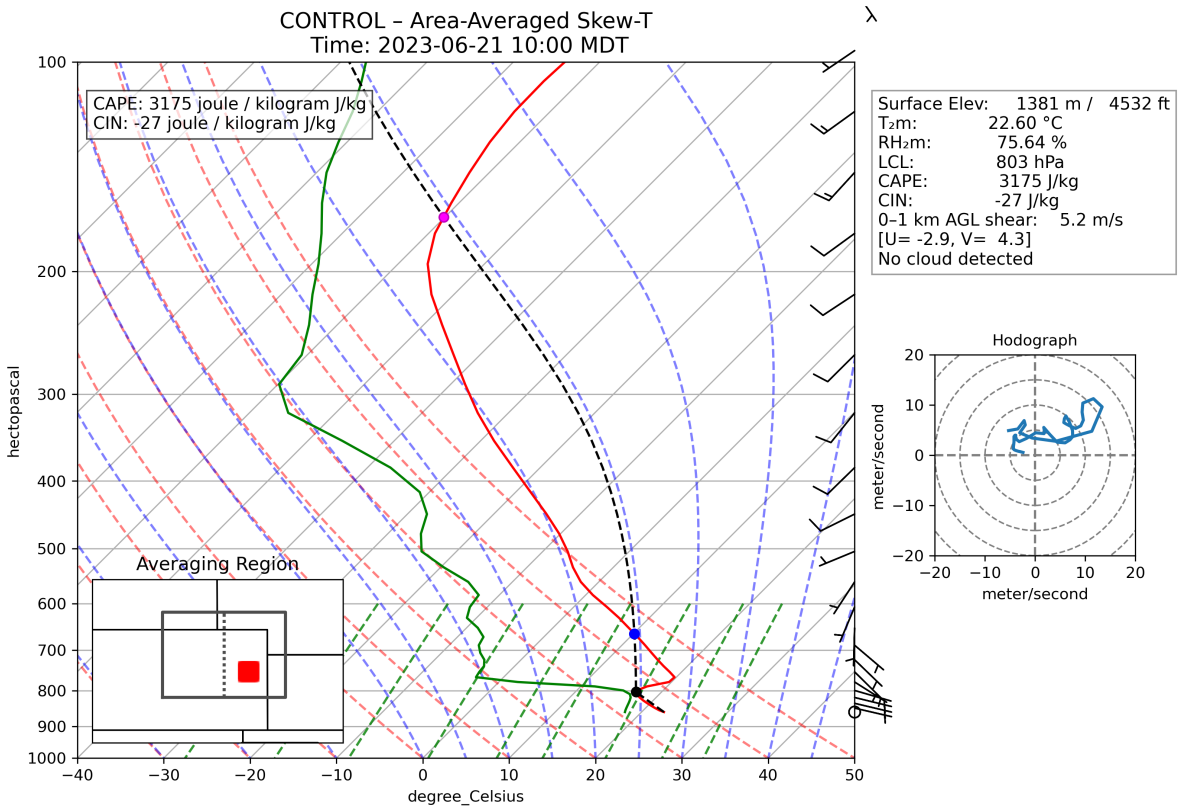


Figure 4.11: Area-averaged Skew-T log-p profile at 1000 MDT for the CONTROL simulation, Grouping #1 (E/W gradient, large patch), centered on the observed CI region. Solid red and green lines show temperature and dewpoint. The dashed black line shows the lifted parcel profile. Filled circles indicate the LCL (black), LFC (blue), and EL (magenta). Key thermodynamic diagnostics are annotated in the upper left and right of each panel.

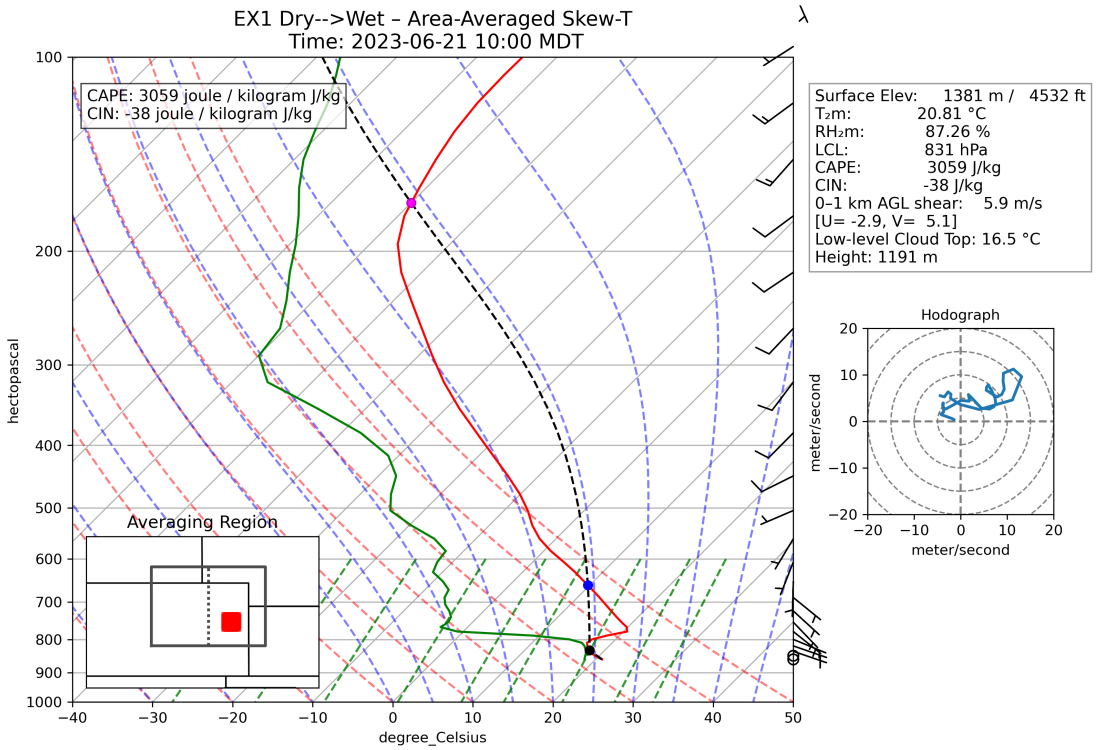


Figure 4.12: As in Figure 4.11, but for EX_1 Dry→Wet.

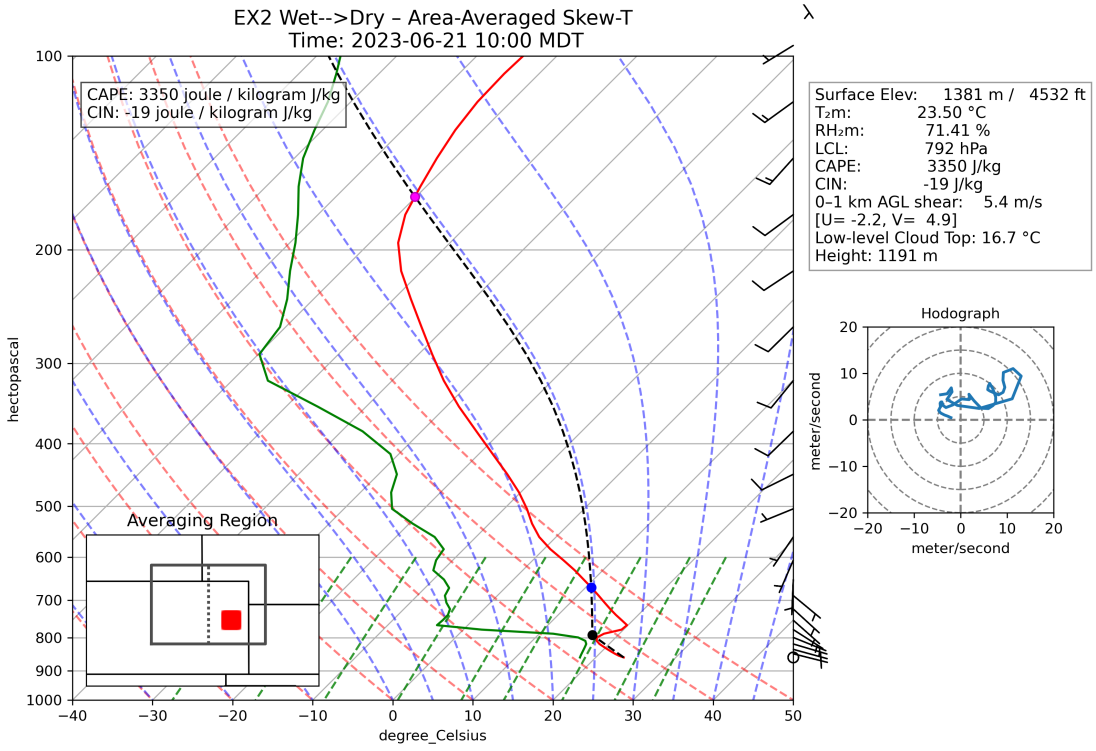


Figure 4.13: As in Figure 4.11, but for EX_2 Wet→Dry.

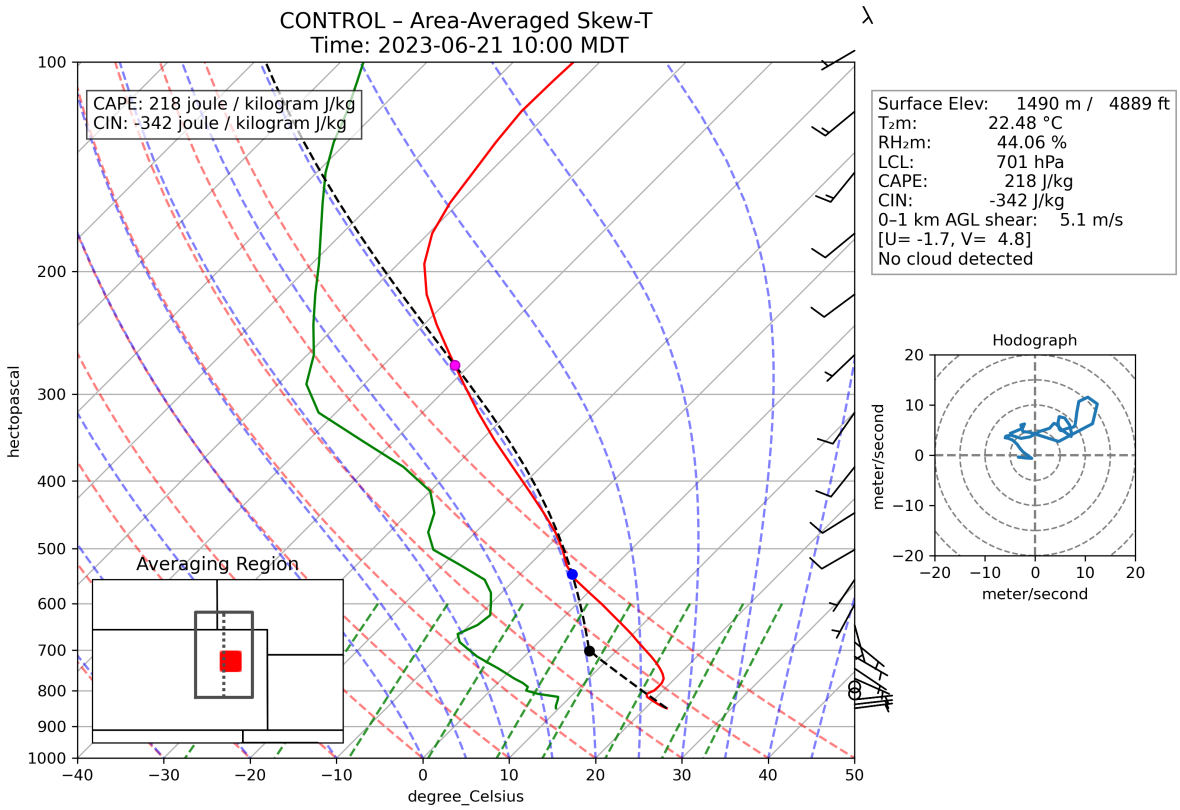


Figure 4.14: Area-averaged Skew-T log-p profile at 1000 MDT for the CONTROL simulation, Grouping #2 (E/W gradient, narrow patch), centered on the observed CI region. Solid red and green lines show temperature and dewpoint. The dashed black line shows the lifted parcel profile. Filled circles indicate the LCL (black), LFC (blue), and EL (magenta). Key thermodynamic diagnostics are annotated in the upper left and right of each panel.

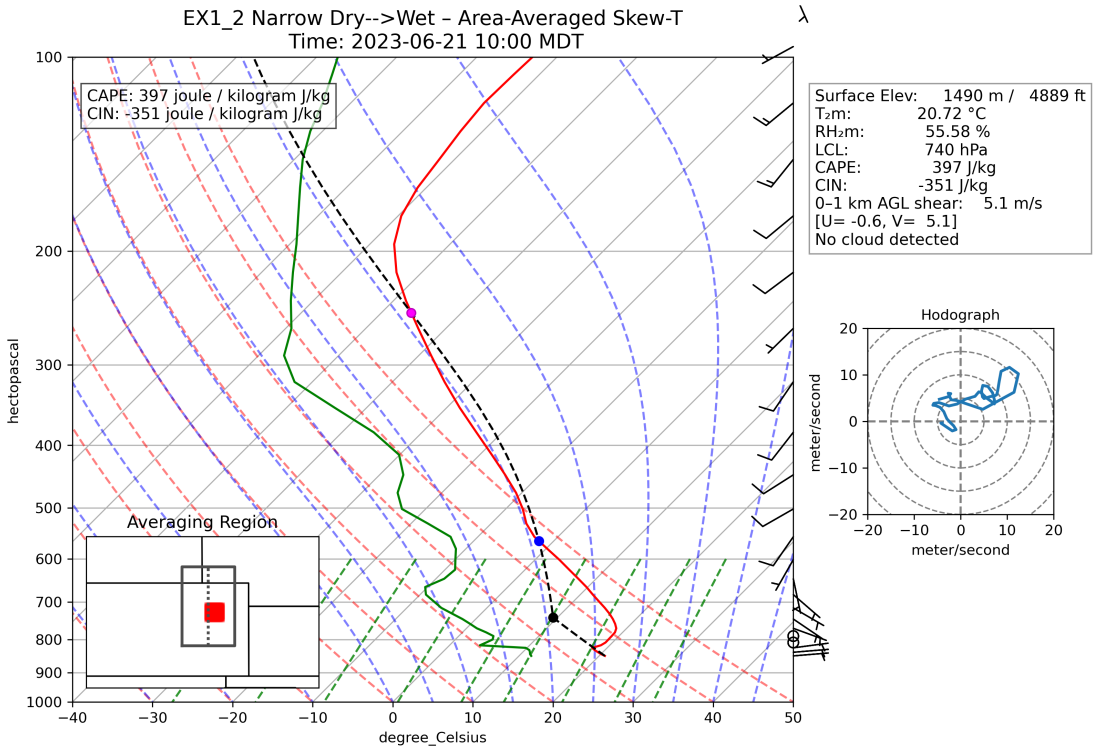


Figure 4.15: As in Figure 4.11, but for EX1_2 Narrow Dry→Wet.

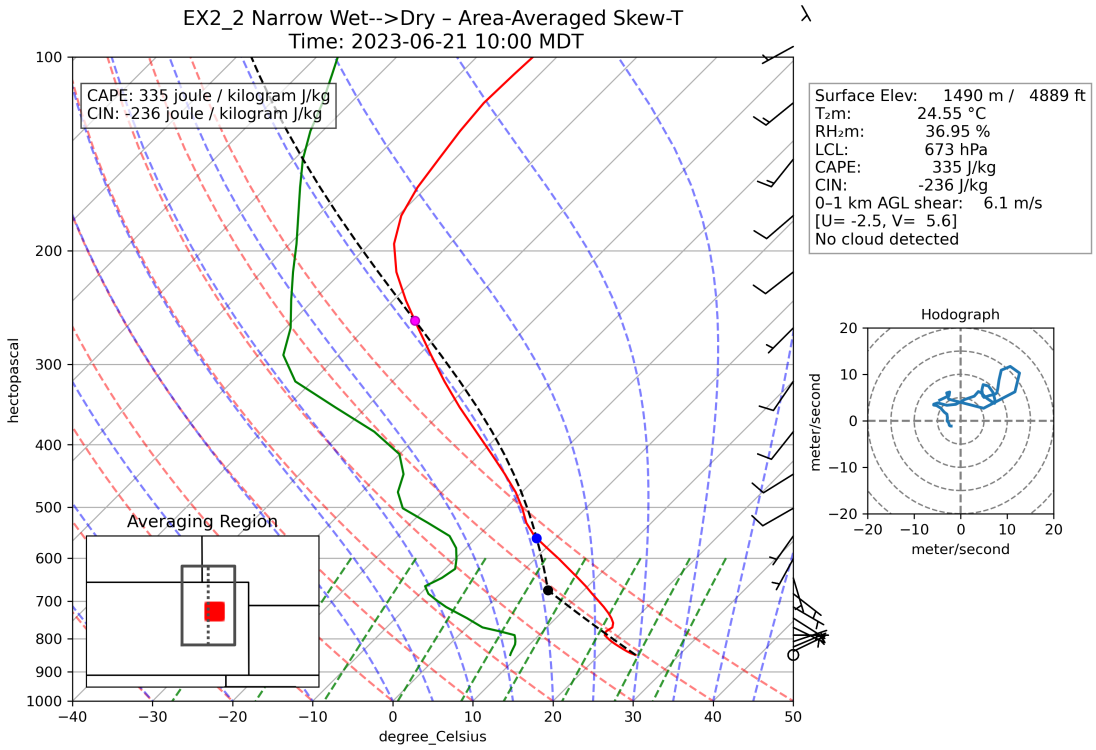


Figure 4.16: As in Figure 4.11, but for EX2_2 Narrow Wet→Dry.

For Grouping #2 (Figures 4.14, 4.15, and 4.16) the thermodynamic environment sampled by Grouping #2 differs substantially from Grouping #1, reflecting the higher surface elevation of the averaging region (1490 m vs. 1381 m) and a drier ambient environment. CAPE values are considerably lower across all experiments (218–397 J/kg) and CIN is substantially stronger (-236 to -351 J/kg), indicating a more strongly capped atmosphere at this location. The dry perturbation (EX2_2 Wet→ Dry) again produces the warmest surface temperature (24.6°C), lowest RH (37.0%), and lowest LCL (673 hPa), but here exhibits lower CAPE (335 J/kg) than the wet perturbation (EX1_2: 397 J/kg), with an intermediate CIN (-236 J/kg). The wet perturbation shows a cooler, more moist profile (T2m_2m 2m = 20.7°C, RH = 55.6%) and higher LCL (740 hPa), but stronger CIN (-351 J/kg). The CONTROL exhibits the highest CIN (-342 J/kg) and lowest CAPE (218 J/kg) of the three. These results suggest that in the drier, more elevated environment sampled by Grouping #2, the thermodynamic pathway to CI is more strongly inhibited across all experiments, and the differences in CAPE between wet and dry perturbations are less consistent than in Grouping #1. This is consistent with the dynamical forcing, rather than thermodynamic destabilization — being the primary driver of CI in this grouping.

Grouping #3 (Figures 4.17, 4.18, and 4.19) profiles are drawn from the highest elevation averaging region (1913 m), and show intermediate CAPE values (916–1052 J/kg) with moderate CIN (-159 to -188 J/kg) relative to the other groupings. Unlike Groupings #1 and #2, the thermodynamic separation between the wet and dry perturbation experiments in Grouping #3 is small. The wet perturbation (EX_3 Wet→ Dry) shows slightly higher CAPE (1052 J/kg) and weaker CIN (-159 J/kg) than the dry perturbation (EX_4 Dry→ Wet: CAPE = 916 J/kg, CIN = -188 J/kg), with the CONTROL falling between (CAPE = 1024 J/kg, CIN = -168 J/kg). Near-surface temperatures are similar across all three experiments (16.7–17.6°C), and LCL heights are nearly identical (738–756 hPa), suggesting that the soil moisture perturbation has a more limited influence on the thermodynamic structure at this location and orientation. The notable feature of Grouping #3 is the stronger 0–1 km AGL shear (8.6–9.0 m/s) relative to Groupings #1 and #2 (5–8 m/s), which may

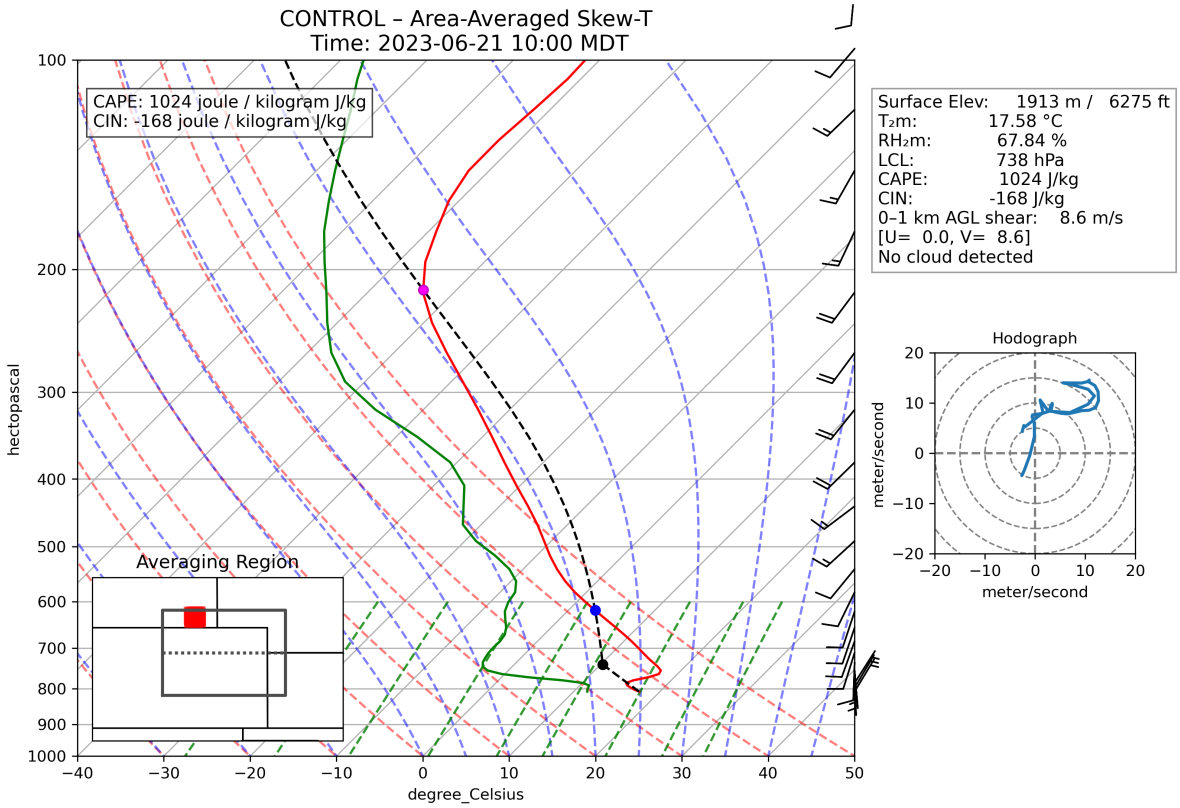


Figure 4.17: Area-averaged Skew-T log-p profile at 1000 MDT for the CONTROL simulation, Grouping #3 (N/S gradient, large patch), centered on the observed CI region. Solid red and green lines show temperature and dewpoint. The dashed black line shows the lifted parcel profile. Filled circles indicate the LCL (black), LFC (blue), and EL (magenta). Key thermodynamic diagnostics are annotated in the upper left and right of each panel.

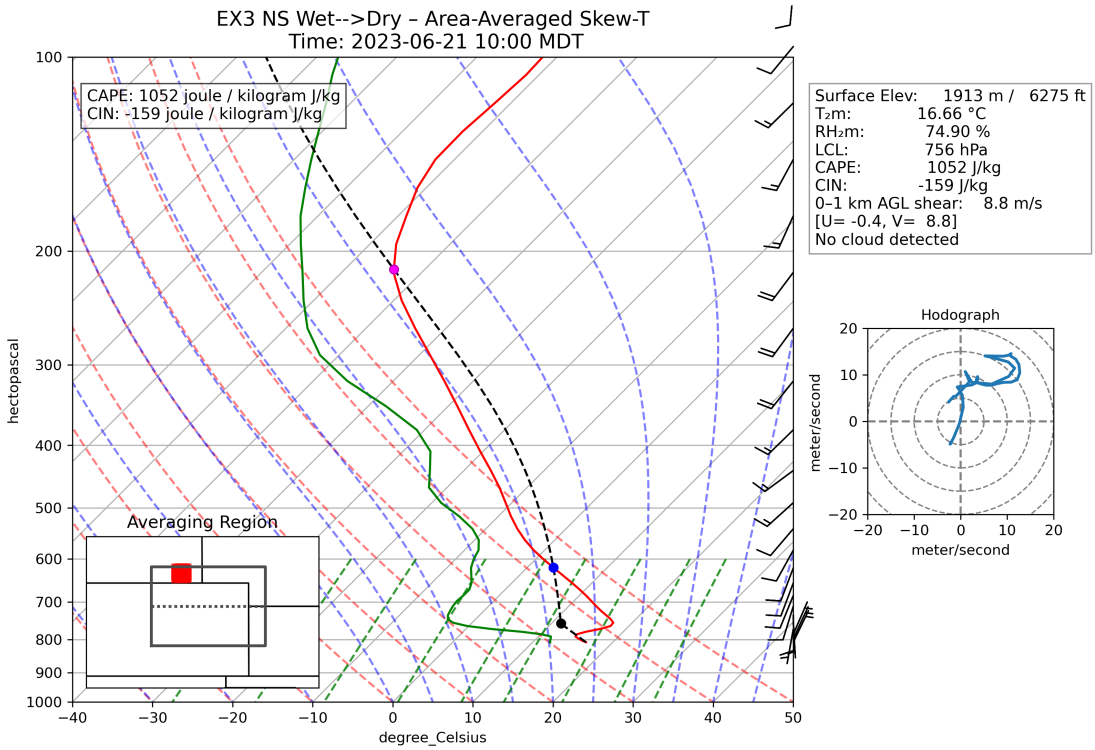


Figure 4.18: As in Figure 4.11, but for EX_3 N/S Wet→Dry.

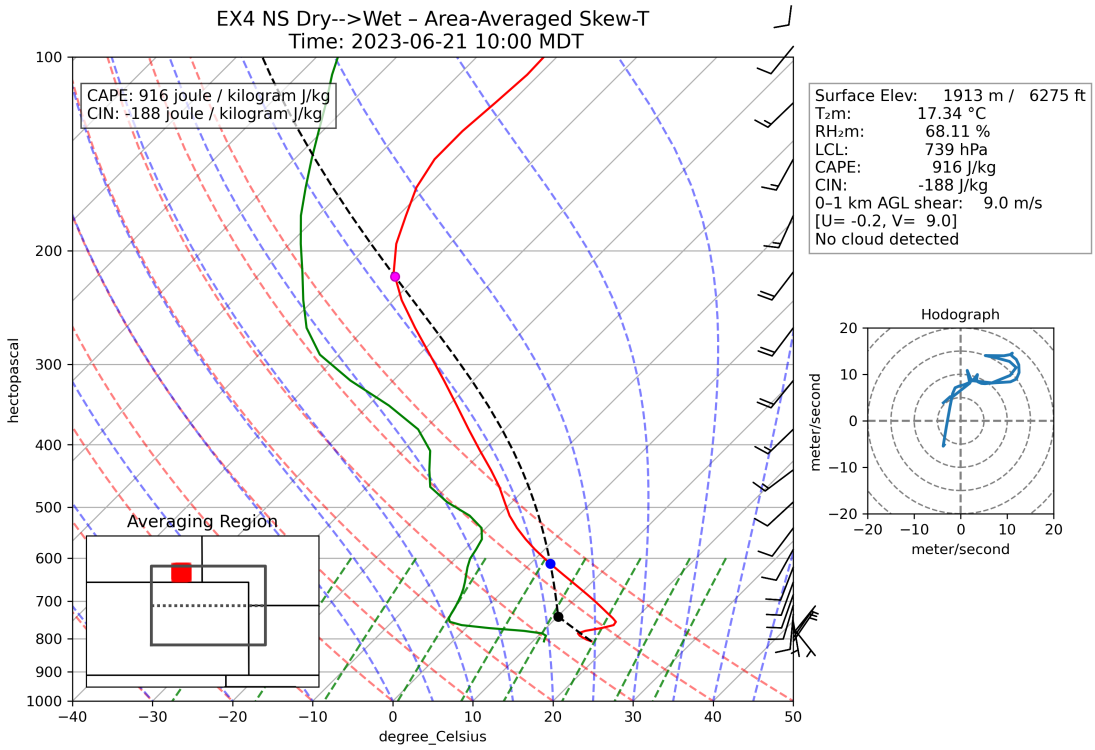


Figure 4.19: As in Figure 4.11, but for EX_4 N/S Dry→Wet.

contribute to storm organization following CI but does not appear to be the primary discriminator between experiments.

These skew-T diagnostics across all three groupings reveal that the soil moisture perturbations consistently modify the near surface thermodynamic structure in a physically coherent manner... the dry perturbations produce warmer, drier boundary layers with lower LCLs and generally higher CAPE, while wet perturbations create cooler, moister profiles with higher LCLs and stronger CIN 4.1. However, the magnitude of these thermodynamic differences varies quite a bit with the ambient environment of the averaging region. With Grouping #1 showing the clearest separation between experiments and Grouping #3 showing the least. Across all groupings, the thermodynamic differences alone are not fully sufficient to explain the preferential CI over dry soil regions and in several cases the wet perturbation experiments maintain comparable or even slightly higher CAPE than their dry counterparts. But from the earlier analysis it is known that here the CI still favors the dry subregion. This points again to the dominant role of dynamical forcing, specifically the mesoscale convergence driven by differential sensible heating, in determining where parcels are lifted to their LFC and CAPE is realized. Cloud cover can modulate the surface energy budget and boundary layer evolution in ways that interact with both the thermodynamic and dynamical pathways to CI. So before examining the convergence and vertical motion fields directly, the distribution of low level clouds in the pre-convective environment is considered as the next clue.

Table 4.1: Summary of area-averaged Skew-T thermodynamic diagnostics at 1000 MDT for each experiment and grouping, centered on the observed convection initiation region.

Group	**Experiment**	**T_{2m} (°C)**	**RH (%)**	**LCL (hPa)**	**CAPE (J kg^{-1})**	**CIN (J kg^{-1})**
None	GFS	21.1	72.5	780	2302	−87
#1	CONTROL	22.6	75.6	803	3175	−27
	EX1 Dry→Wet	20.8	87.3	831	3059	−38
	EX2 Wet→Dry	23.5	71.4	792	3350	−19
#2	CONTROL	22.5	44.1	701	218	−342
	EX1_2 Dry→Wet	20.7	55.6	740	397	−351
	EX2_2 Wet→Dry	24.6	37.0	673	335	−236
#3	CONTROL	17.6	67.8	738	1024	−168
	EX3 Wet→Dry	16.7	74.9	756	1052	−159
	EX4 Dry→Wet	17.3	68.1	739	916	−188

Across all groupings, the wet perturbation experiments exhibit lower near-surface temperatures and higher dewpoint temperatures relative to the dry perturbation experiments, which is consistent with an evaporative cooling and boundary-layer moistening response. Conversely, the dry perturbation experiments consistently show higher surface temperatures and reduced dewpoints, indicative of enhanced sensible heating and a drier boundary layer. These changes near the surface strongly influence the structure of the boundary layer and the magnitude of CAPE and CIN. The skew-T profiles provide a useful too for identifying whether changes in instability are primarily driven by boundary-layer moistening, changes in lapse rate, or differences in the strength and height of the capping inversion.

The largest thermodynamic separations between experiments are most evident in Groupings #2 and #3. For Grouping #2, a clear difference is evident in the depth and structure of the boundary layer, defined here as the layer between approximately 1000–700 hPa. In EX_{12} (dry-to-wet), the averaged profile exhibits a shallower mixed layer and a reduced temperature–dewpoint spread in the lowest levels, suggesting a lower lifted condensation level (LCL) and potentially a lower cloud base. Additionally, EX_{12} displays the strongest capping inversion near $\sim$800 hPa before converging toward a similar mid-level structure as the other experiments. This indicates that the primary thermodynamic differences across Grouping#2 are concentrated in the lowest levels and are likely tied to land surface driven modifications of boundary-layer moisture and stability.

A counterintuitive result emerges from Grouping #2: the wet perturbation experiment (EX1_2) produces *higher* CAPE (397 J kg^{-1}) than the dry perturbation (EX2_2: 335 J kg^{-1}), yet convection still preferentially initiates over the dry region. This reversal of the typical Grouping #1 pattern provides compelling evidence that thermodynamic instability, while important, is not the primary discriminator of the convection initiation location. Instead, dynamical forcing (via surface pressure gradients and low-level convergence) dominates.

For Grouping #3, the largest differences emerge with increasing height above the boundary layer. In particular, EX_4, which is averaged over the dry portion of the perturbation region, exhibits a more saturated layer between approximately 700–600 hPa. This result is notable, as the expecta-

tion would be that the wet perturbation experiments produce the most saturated low-level profiles through enhanced surface evaporation. One possible explanation is that the averaging region, defined by early and intense convective initiation, preferentially samples locations where convection has already initiated and where moistening aloft may reflect storm-driven processes (e.g., entrainment, vertical transport, or mesoscale moisture convergence), rather than direct boundary-layer moistening by the land surface. Therefore, while soil moisture perturbations primarily modify thermodynamic structure in the lowest levels, differences above the boundary layer in Grouping #3 may be influenced by convective feedbacks and the location of the averaging region relative to the evolving storm environment

4.3.1 Low-level Clouds

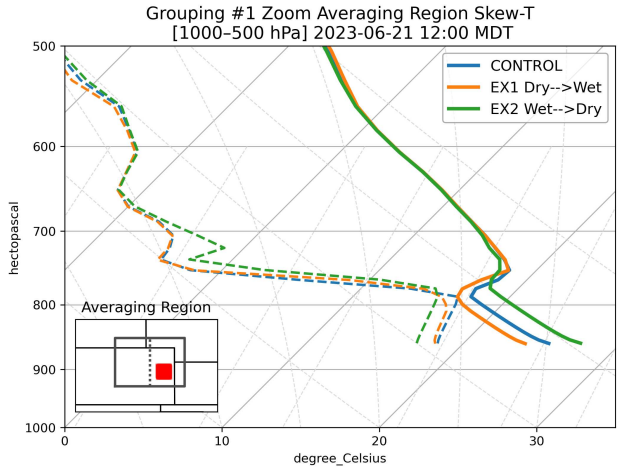
When looking at the conditions of the atmosphere before and after convection initiation, one of the helpful markers for the moisture is the presence or absence of low-level clouds. So the analysis here is being done to see how the pre-convection conditions of the atmosphere were taking physical shape.

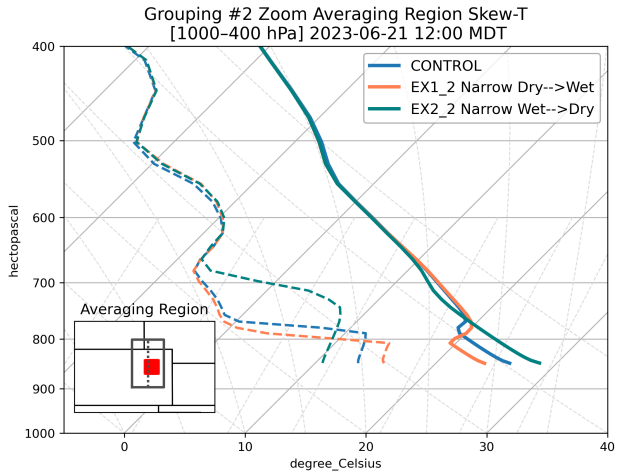
Across all the experiments, the early morning cloud formation remained relatively shallow. But in WRF, there are many variables we can use at different vertical levels to help make a more complete picture of the early morning clouds.

- QCLOUD (WRF variable): cloud water mixing ratio in kg/kg
- CLDFRA (WRF variable): represents the fraction of grid cells covered by clouds

Regardless of experiment grouping, the amount of difference seen does not begin to appear until after sunrise. The conditions prior to sunrise are not "activated" because there is not nearly as much evapotranspiration taking place. After sunrise, the differences in the low-level clouds and their dissipation is slight, with the most amount of difference seen around the transition region or soil moisture.

When the lower portion of the skew-T profiles where isolated, similar trends emerge across all experiment groupings; the wet and dry perturbation simulations generally sandwich the control





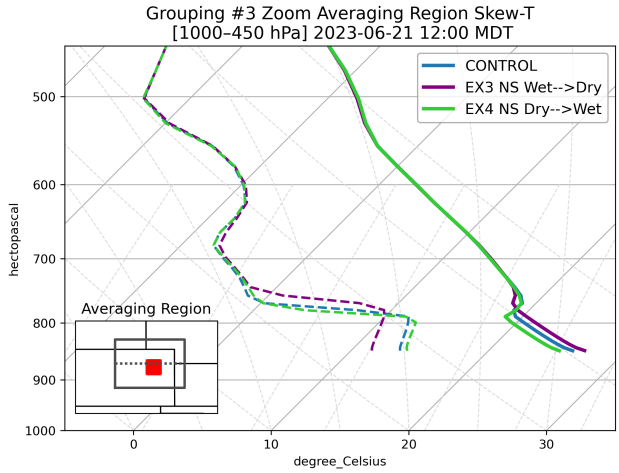


Figure 4.20: Composite bottom-layer skew-T log-p profiles at $t = 0$ h averaged over the region of strongest convective initiation (CI) signal for each soil moisture perturbation grouping.

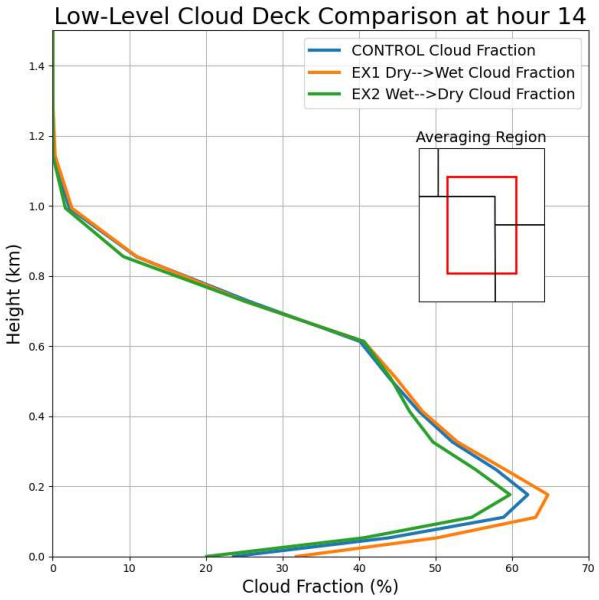
run, with the control profile falling between the two experiments (Fig. 4.20). The skew-T profiles shown here are spatially averaged over the region of earliest and most intense convective initiation, defined using a 40 dBZ reflectivity threshold. As a result, the averaging region tends to favor the drier portion of the soil moisture perturbation rectangle, which should be considered when looking at differences between wet and dry perturbation runs.

In looking at the averaged cloud fraction over the soil moisture perturbation regions, there are differences in the average percent of clouds covering the region, but no apparent differences in the average height of the cloud deck (Fig.4.21). Limited to the synoptic conditions of the day chosen, the presence of low-level clouds was biased to the Eastern part of the state. So when comparing where the low-level clouds sat, the E/W gradient groupings (#1,#2) were realistically limited to the Eastern parts of the perturbation domains for the early morning hours. For the North/South gradient, both the North and South region showed similar differences so the region with the higher average cloud fraction was chosen for comparison.

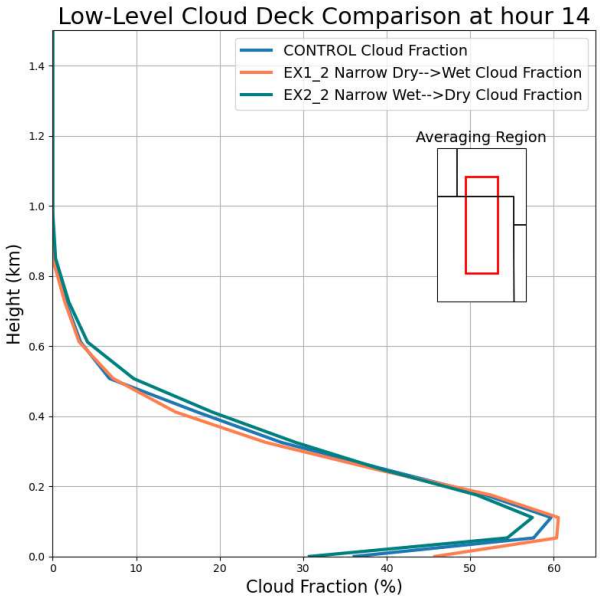
Visually seen in the comparisons between the $QCLOUD$, there exist very small differences in the cloud cover between the northern and southern region for Grouping #3. Specifically, in the middle of the Northern half there appears to be slightly more low level cloud cover more West in EX_3 over the "wet" region (Fig. 4.22). Among the 3 groupings, these differences are commonly seen over the vertical midline of all the perturbation boxes, suggesting that the presence of low level clouds may be induced from the orographic forcing of the mountains.

Additional analysis was done to find the cloud top temperature (CTT). Here, a warmer CTT means the tops of the clouds are lower in the atmosphere, while a colder CTT signifies deeper and more intense convection because the clouds reach higher altitudes. To investigate the presence of low-level clouds in the pre-convection hours, the CTT was spatially mapped alongside outlines of the soil moisture perturbation regions.

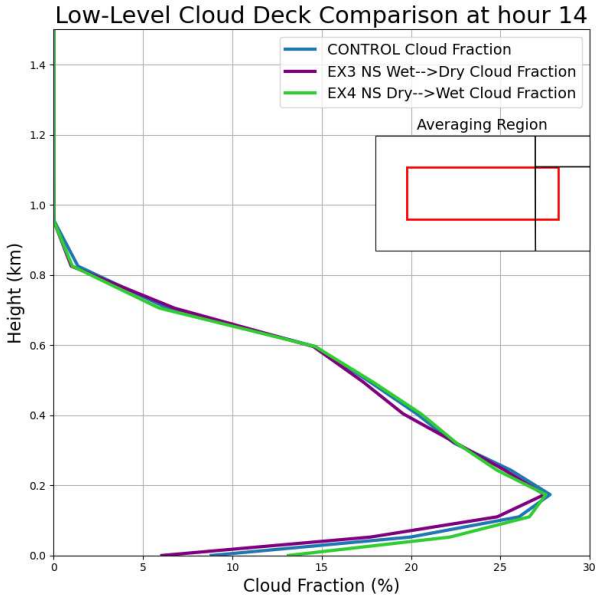
The results show that more intense convection corresponds to colder cloud tops, providing another way to identify where convective initiation occurs. In the early morning hours, there appears to be little variation in cloud distribution except over the areas where the soil changes its



(a) Grouping #1 at 0800 MDT over the Eastern Domain



(b) Grouping #2 at 0800 MDT over the Eastern Domain



(c) Grouping #3 at 0800 MDT over the Southern Domain

Figure 4.21: Comparison of the averaged cloud fraction at 0800 MDT in %. Top row: Groups #1 and #2. Bottom row: Group #3.

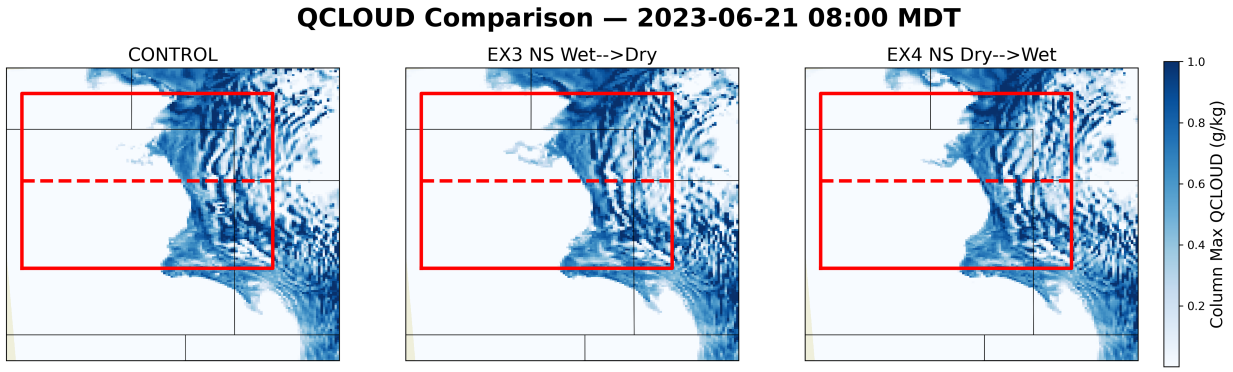


Figure 4.22: Grouping #3 Comparison of the cloud water mixing ratio at 0800 MDT in g/kg.

moisture profile, corresponding to either the vertical or horizontal dashed red line (Fig.4.24, 4.23). The extent of low-level clouds depends on the gradient: in the E/W wet to dry cases (Groups #1 and #2), the early morning clouds extend further into the wet regions. This extended cloud coverage coincides with areas of steep topography, suggesting that orographic effects may also play a role. In particular, upslope flow along the Front Range during the early morning driven by differential heating at sunrise can enhance cloud formation over elevated terrain, contributing to the observed distribution of low-level clouds (Whiteman, 2000).

The wet regions generally show more consistent cloud coverage, with fewer cloud free gaps. In the N/S soil moisture gradient cases, a similar pattern appears: clouds are more prevalent over wet areas, but this same result into the transitional region is not observed. This comparison suggests that the early morning low-level cloud distribution is more strongly influenced by the topography and presence of wet soils than by the orientation of the soil moisture gradient itself. Implying that the orographic effects and injection of moisture are dominating where the clouds are forming rather than a dynamical effect from the gradient in soil moisture itself.

4.4 Storm Morphology

Storm morphology describes the structural characteristics and organization of convective storms, including the intensity, and the longevity. In the analysis of this study, it is evaluated to determine how variations in land surface conditions may effect storm path and evolution. There are numer-

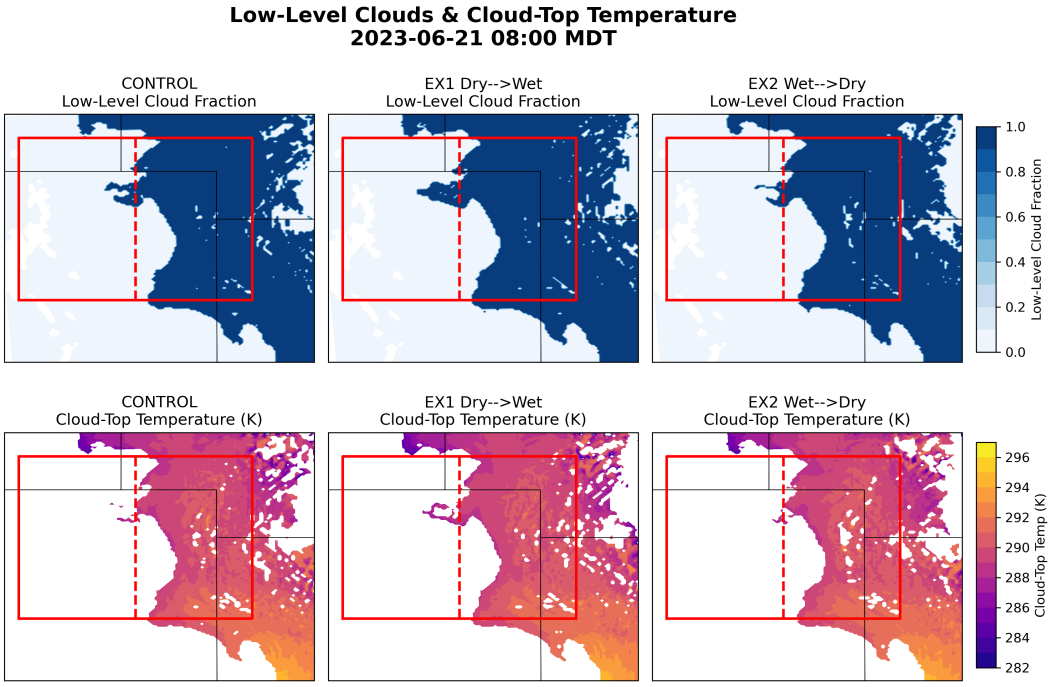


Figure 4.23: Grouping #1 Cloud fraction (blues) and the cloud top temperature between 1000–700 hPa at 0800 MDT.

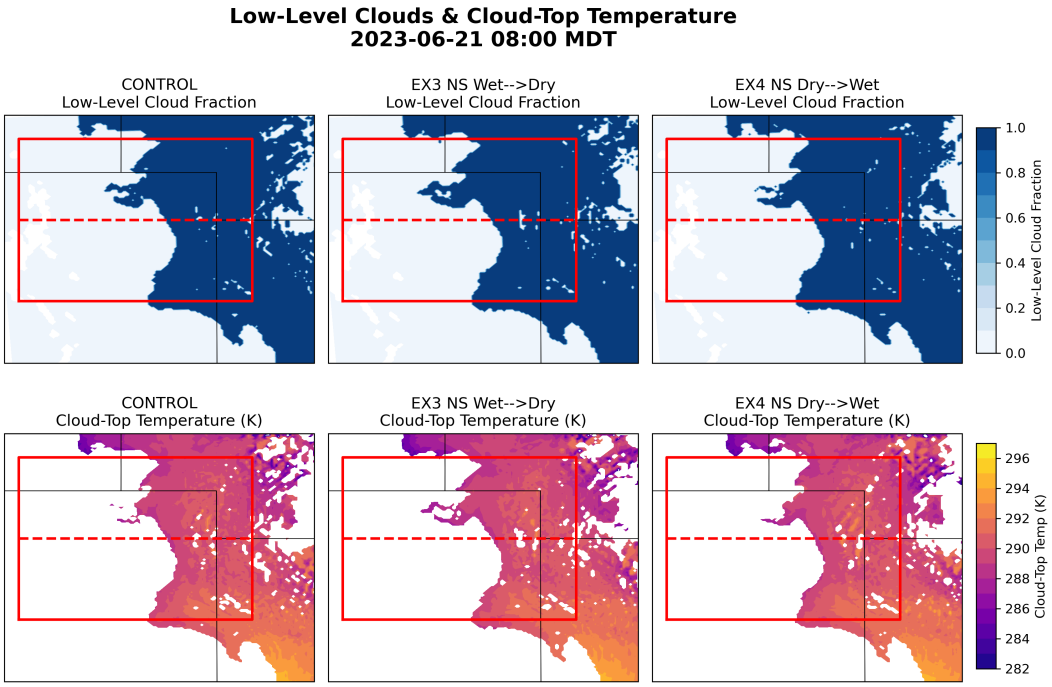


Figure 4.24: Grouping #3 Cloud fraction (blues) and the cloud top temperature between 1000–700 hPa at 0800 MDT.

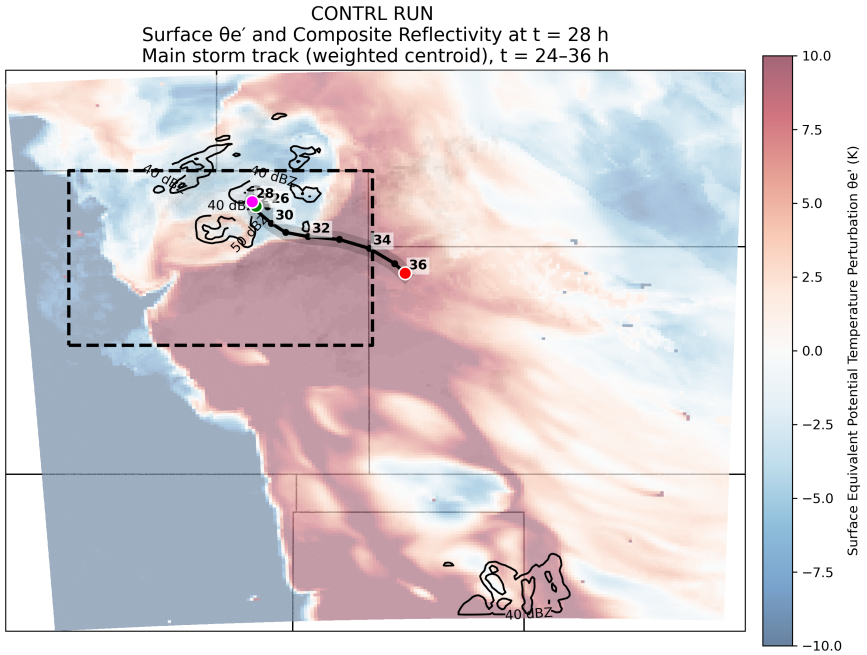


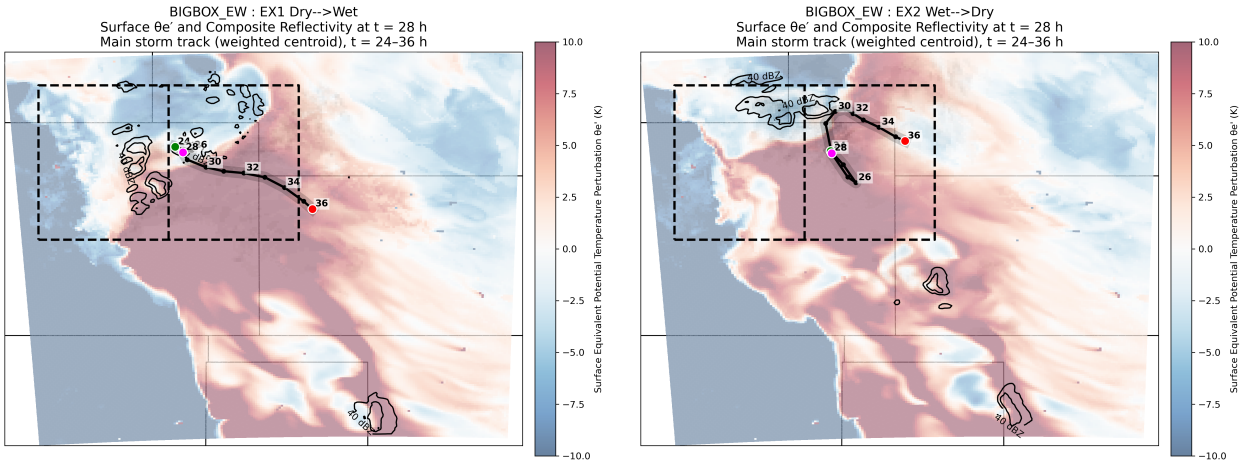
Figure 4.25: Storm track of the CONTROL Run from hours 28-36 of the forecast, with overlaid surface equivalent potential temperature

ous centroid-based tracking methods available to WRF output files in python. but for this purpose and context, a simple centroid-based approach was written to track the system, which is better for storms that undergo splitting, merging, and expansion. By averaging the storm's centroid, a generalized storm track can be made that captures the overall evolution of the system despite meteorological changes.

The CONTROL run provides a baseline of the storm morphology and propagation throughout the convective period for this study (Fig. 4.25). The primary convective system develops along the Front Range before propagating southeastward into eastern Colorado and western Kansas. The centroid-based track reveals that the storm maintains a relatively coherent structure through the evening hours, with the strongest reflectivity cores generally aligned along the leading edge of the southeastward-moving system. Regions of low surface equivalent potential temperature (θ_e) remain collocated with areas of sustained convection, indicating the importance of boundary-layer moisture and instability in maintaining storm intensity. While the overall trajectory is governed by

the synoptic-scale environment, localized variations in storm intensity and propagation appear tied to mesoscale thermodynamic gradients.

For Grouping #1, both perturbation experiments exhibit similar large-scale southeastward propagation compared to the CONTROL run, but notable differences in the location and persistence of convective development (Fig. 4.26). In EX_1 (Wet $\rightarrow$ Dry), stronger reflectivity cores preferentially develop along the drier eastern portion of the perturbation region, where enhanced sensible heating promotes stronger boundary-layer destabilization. In contrast, EX_2 (Dry $\rightarrow$ Wet) shows a more spatially distributed convective structure, with storm development extending further into the wetter regions where increased moisture availability contributes to higher θ_e. Although the overall storm track remains similar between the two experiments, the organization and reinforcement of convection differ, suggesting that the orientation of the soil moisture gradient impacts where convective cells intensify and persist.



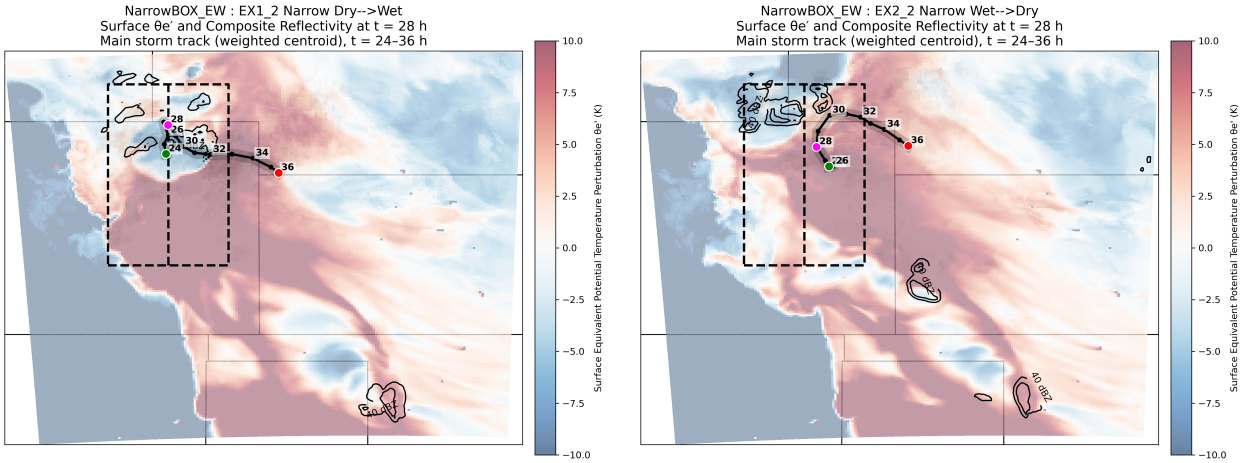
(a) EX_1: Wet $\rightarrow$ Dry (Grouping #1)

(b) EX_2: Dry $\rightarrow$ Wet (Grouping #1)

Figure 4.26: Convective initiation and cell development over dry perturbation regions for Grouping #1, highlighting the reinforcement of storm intensity and cold-pool formation.

At hour 28 of the forecast window (2200 MDT), an overlay of the theta-e perturbation and contours of reflectivity above 40 dBZ clearly shows the storm's shape. Using the centroid-based method, the storm track is plotted as a continuous black line, with some hourly points appearing intermittent due to differences in reflectivity thresholds. Most of the activity occurs between hours

24–36 (1800–0600 MDT), capturing the core period of storm development. The general morphology and southeastward propagation of the system are illustrated in Figures 4.27a and 4.27b (Grouping #2), which show the centroid-based tracks and reflectivity contours. Comparison of



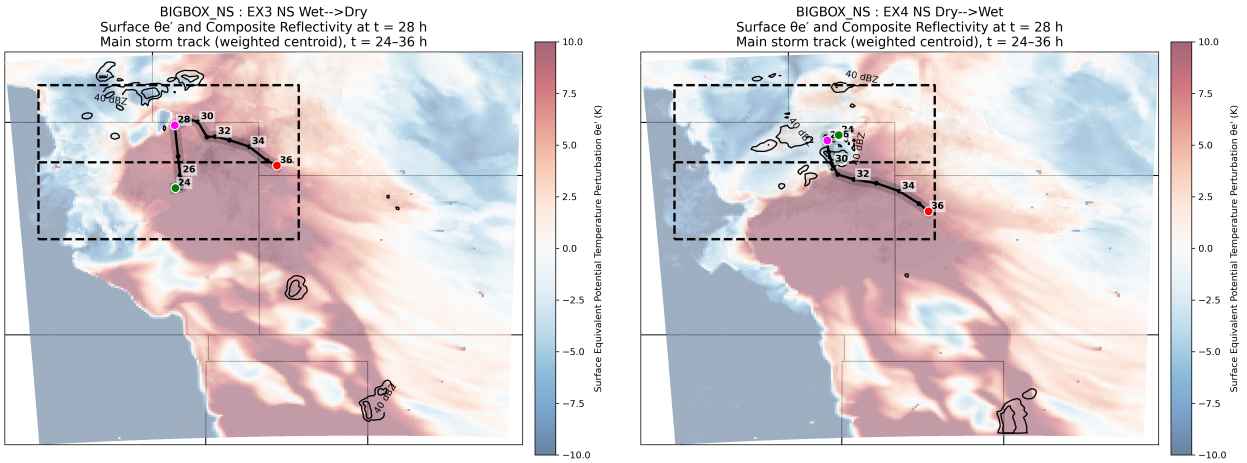
(a) EX1_2: Dry → Wet (Grouping #2)

(b) EX2_2: Wet → Dry (Grouping #2)

Figure 4.27: Centroid-based storm tracks and reflectivity contours for Grouping #2, showing the overall storm morphology and track.

storm tracks across runs reveals both similarities and differences. While the final storm location on June 22 is largely determined by the synoptic setup and initial conditions, the pathway the system follows is influenced by soil moisture patterns. As demonstrated in the previous section, convective initiation preferentially occurs over drier regions, a tendency reflected in the higher magnitude portions of the storm track. In both west to east soil moisture gradients (Groupings #1 and #2), initiation occurs around hours 18–20, but significant reflectivity is not observed until hour 24. Once convection is established, the storm path becomes more defined, often lingering in the northeast corner of the dry perturbation regions. The reinforcement of convective initiation and subsequent cell development is evident in Figures 4.28b and 4.28a (Grouping #3), highlighting how dry regions enhance storm intensity and cold-pool formation.

Despite these differences, the overall morphology and southeastward trajectory of the storms remain consistent. The synoptic setup drives the end points to western Kansas and southwestern Nebraska, showing the dominant role of large-scale forcing. However, soil moisture variations



(a) EX_3: Wet → Dry (Grouping #3)

(b) EX_4: Dry → Wet (Grouping #3)

Figure 4.28: Convective initiation and cell development over dry perturbation regions for Grouping #3, highlighting the reinforcement of storm intensity and cold-pool formation.

influence where initiation occurs and how the storm evolves, with theta-e perturbations providing insight into which convective cells intensify and which dissipate. This underscores the nuanced interplay between land surface conditions and storm development.

4.5 Precipitation

Analysis of the cumulative precipitation was conducted for each experiment to evaluate how soil moisture perturbations influence the downstream impacts of convective storms, particularly in terms of rainfall placement and intensity. While the primary focus of the results has to do with the initiation of convection, precipitation provides an good measure of storm evolution and surface impact. So therefore it is a useful diagnostic for how differences in storm development translate to hydrologic impacts. In such idealized simulations, such as the ones in this study, one might expect clearer and more systematic shifts in precipitation patterns associated with the imposed soil moisture gradients.

However, the results indicate that precipitation was highly localized and varied from region to region, with differences in accumulation more closely tied to storm track and morphology than to the direct influence of the soil moisture perturbations. Despite the lack of a strong signal, the analysis reinforces an important point: even small shifts in storm evolution can lead to differences

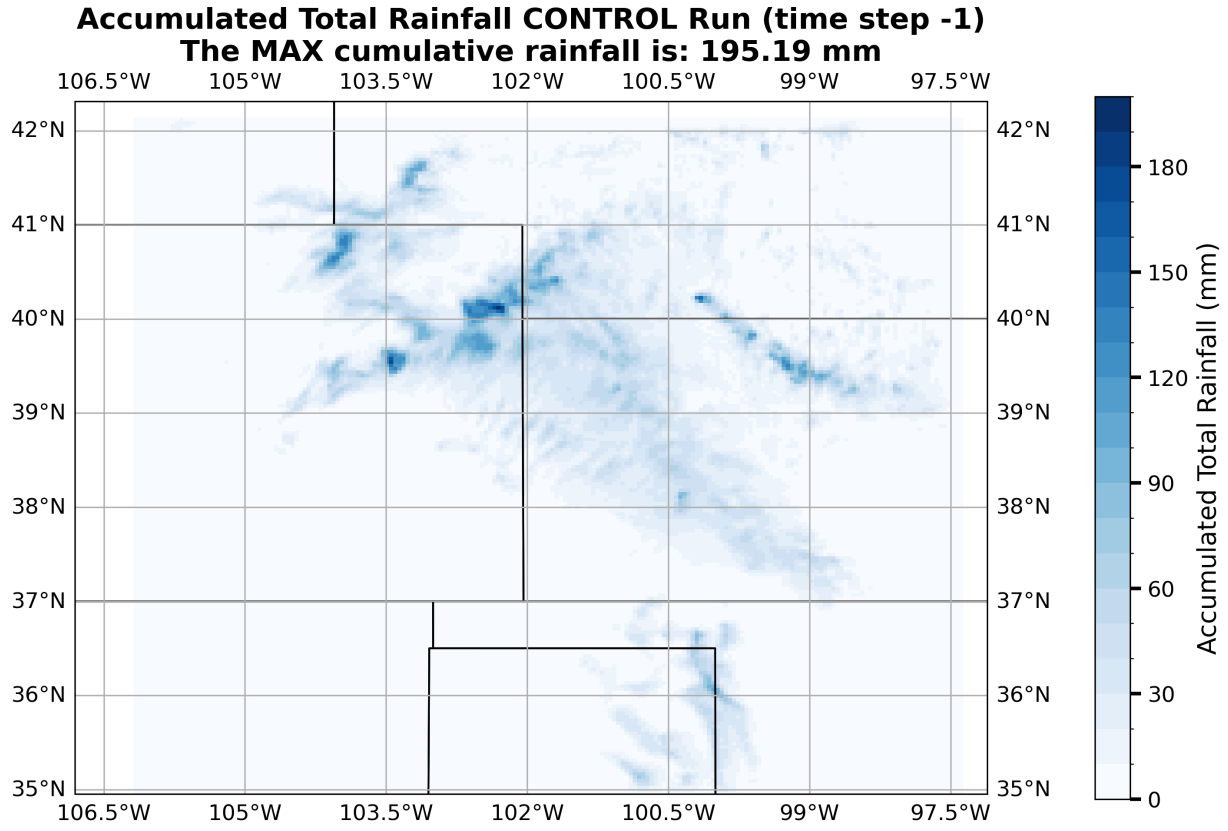


Figure 4.29: Accumulated precipitation from the CONTROL climatology run

in where the most intense rainfall occurs. If these idealized scenarios were realized in nature, these differences could result in substantially different impacts across Eastern Colorado, despite similar large scale storm environments during the 21–22 June 2023 event.

The CONTROL run (Fig. 4.29) shows a swath of accumulated precipitation in dark blue extending from the Front Range of Colorado into western Kansas, consistent with the southeastward propagation of the primary convective system. This is also very similar to the structure of the GFS run, reinforcing the validity of this modeling methodology (Fig. 4.3). The highest precipitation totals are tightly confined to the leading lines of convection, with much weaker accumulations in the surrounding regions. The location of maximum accumulated rainfall occurs along the eastern plains of Colorado, reflecting where the mature stage of the organization of convection occurs.

To quantify how the different land-surface perturbations change the spatial distribution of the rainfall, the grid cell location of maximum cumulative precipitation was overlaid onto the inner

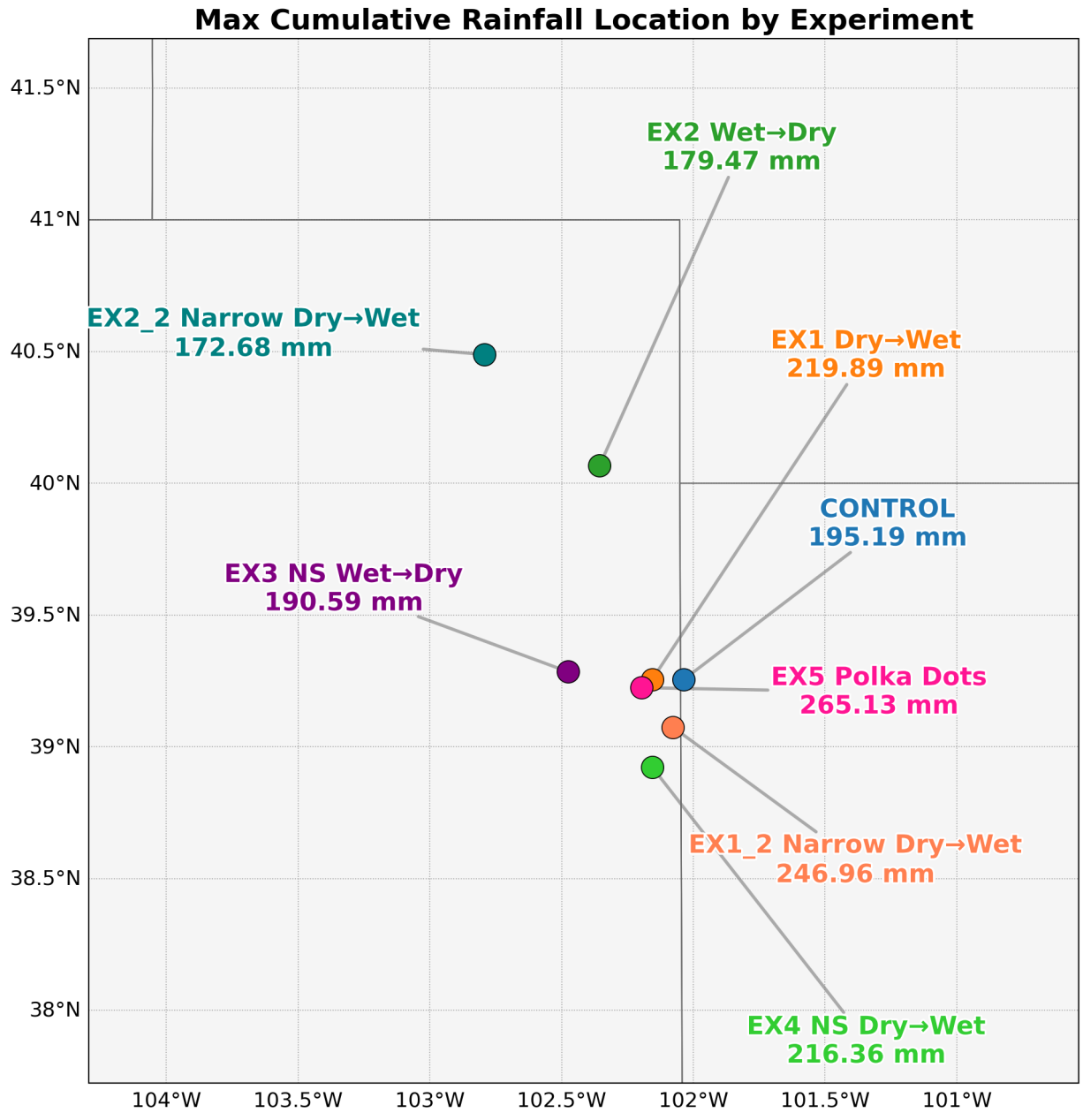


Figure 4.30: Coordinates that record the maximum cumulative rainfall in mm by experiment numbers

domain for each experiment (Fig. 4.30). This diagnostic shows that while all simulations produce broadly similar storm tracks, the exact location of peak rainfall shifts depending on the soil moisture configuration. In particular, East/West gradient experiments (Groupings #1 and #2) tend to displace the rainfall maximum eastward relative to the CONTROL run, consistent with enhanced storm intensification over drier boundary-layer conditions. In contrast, the North/South gradient experiments (Grouping #3) show a stronger meridional spread in the location of peak rainfall, indicating a less constrained convective core and greater sensitivity to mesoscale moisture gradients and terrain influences.

When looking more in depth at the absolute maximum cumulative rainfall and location of maximum rainfall outside of the averaging domain, there are clear differences in both the spatial distribution and magnitude. This type of analysis is important for this experiment's connection to the precipitation totals for the Great Plains.

The following figures were created as an hourly representation of the precipitation averaged over a constant domain box outlined in red. This box was chosen based on the comparison to where a higher concentration of the actual accumulated precipitation fell, as seen in figure 4.30. The goal of this analysis was to look at how the location of max precipitation varied between runs along with the rainfall rate and cumulative rainfall within the box. Across the various soil moisture perturbations, there are some notable differences for discussion; within the averaging region the location of the max precipitation shifts, and the timing of the precipitation (both duration and onset hour) and as a result there are different rainfall rates.

Looking closer at individual experiments compared to the control... it is shown that as the gradient of the difference in soil moisture increased, specifically in EX1_2 the value of the localized maximum precipitation increased from 40 mm to 45 mm. Within the West to East gradients, the location of where the maximum precipitation fell did not change significantly, just in value. However, with the North/South gradient runs, the location of the maximum precipitation seemed be of a larger change, when compared to the actual value of the accumulated rainfall difference from the control. The North to South gradients (EX_3 and EX_4) both shifted the location of the

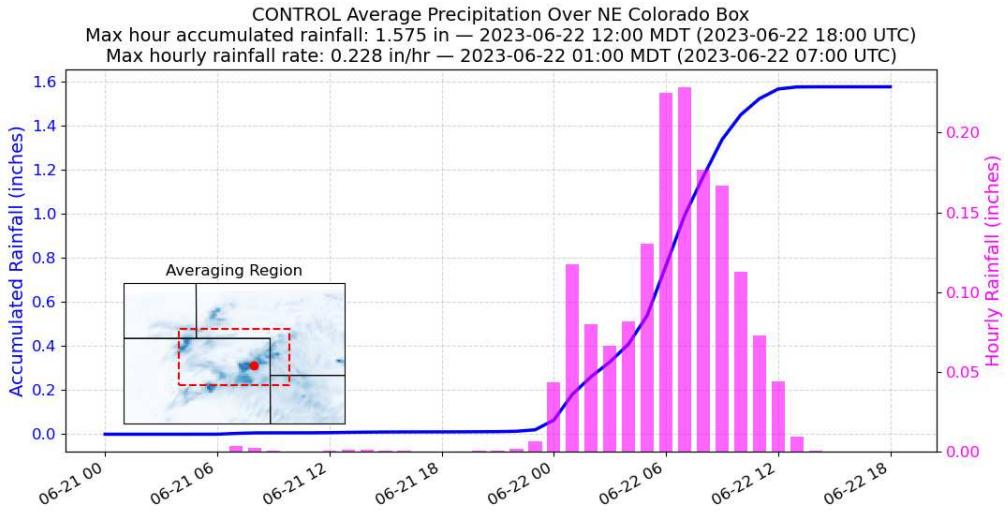


Figure 4.31: Averaged precipitation over the outlined red box for the CONTROL simulation. Hourly rainfall rate is shown over the forecast period, with the maximum precipitation marked by a red dot.

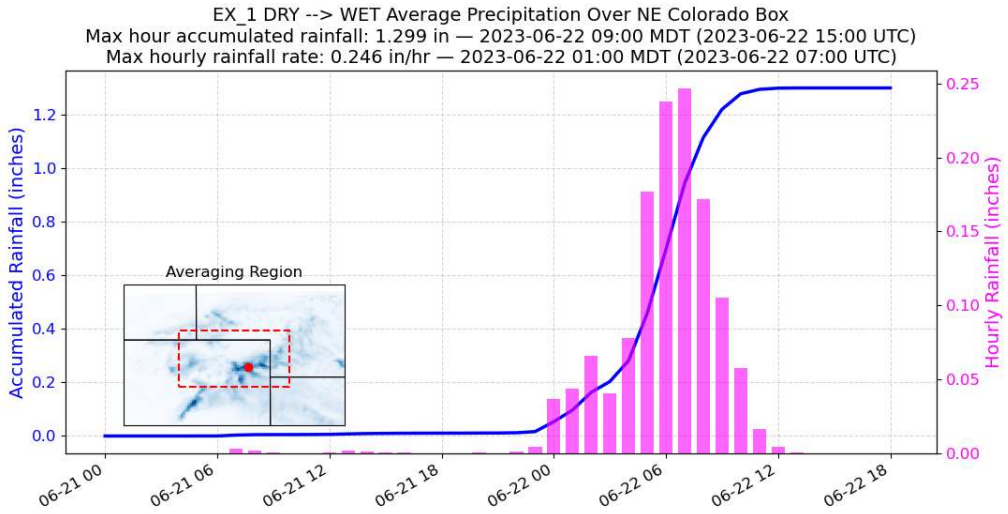


Figure 4.32: Averaged precipitation over the outlined red box for the DRY→WET (EX_1) simulation. Hourly rainfall rate is shown over the forecast period, with the maximum precipitation marked by a red dot.

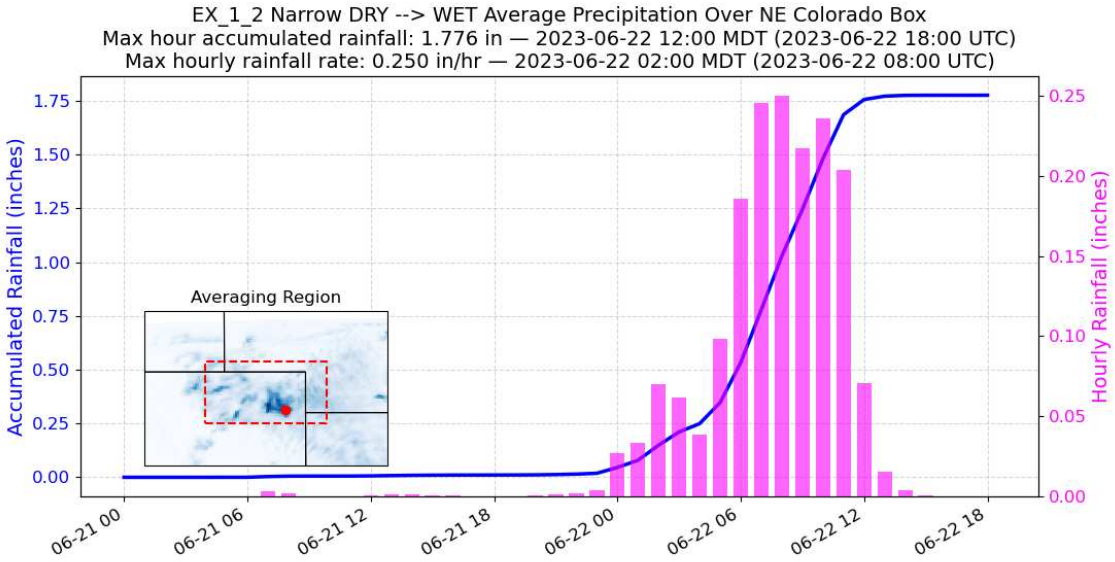


Figure 4.33: Averaged precipitation over the outlined red box for the Narrow DRY→WET (EX_1_2) simulation. Hourly rainfall rate is shown over the forecast period, with the maximum precipitation marked by a red dot.

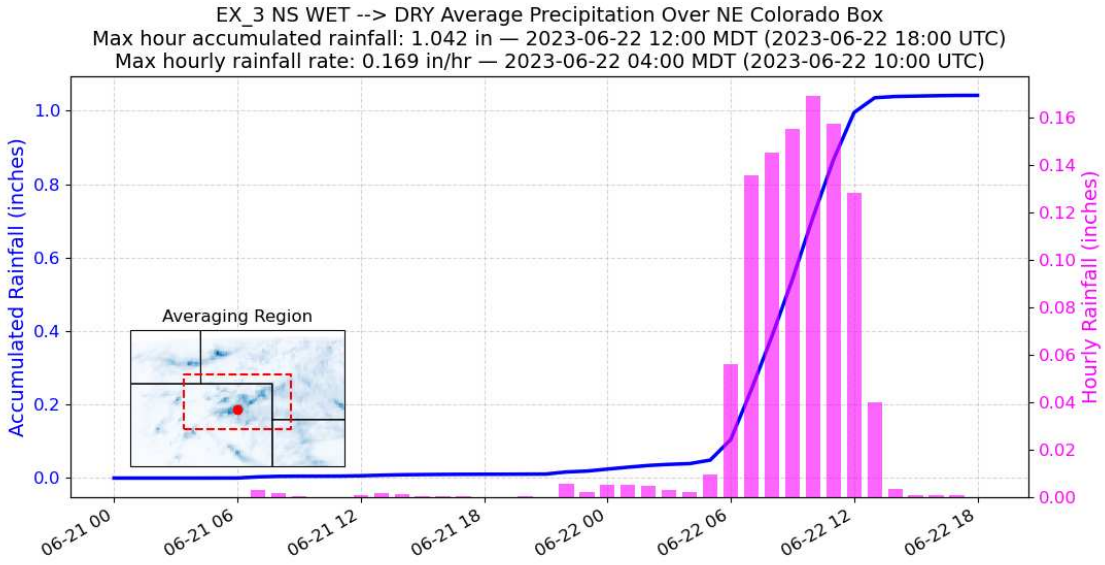


Figure 4.34: Averaged precipitation over the outlined red box for the NS WET→DRY (EX_3) simulation. Hourly rainfall rate is shown over the forecast period, with the maximum precipitation marked by a red dot.

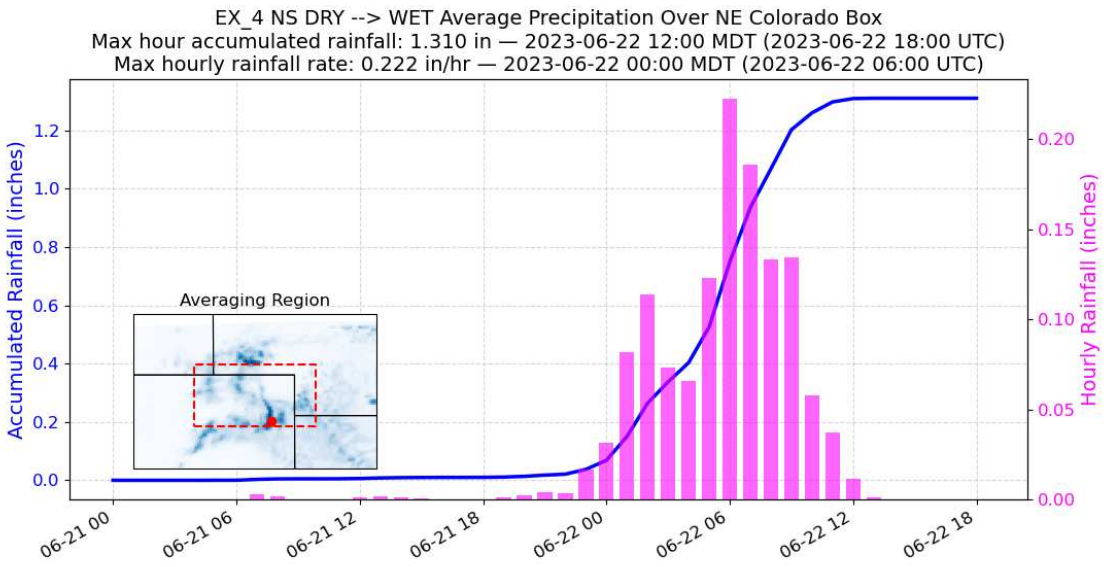


Figure 4.35: Averaged precipitation over the outlined red box for the NS DRY→WET (EX_4) simulation. Hourly rainfall rate is shown over the forecast period, with the maximum precipitation marked by a red dot.

max westward, with EX_4 also shifting south. This is consistent with the analysis of the storm tracks and how the N/S gradients tended to reinvigorate and fight the westerly flow and track back towards the front range later in the forecast run.

It is important to keep in mind that as the storm track shifts, it is expected that the location of where the precipitation falls should change in conjunction. The goal of this analysis, is to examine if there was preferential rainfall over the wet or dry regions or if once convection began, it dominated the near surface effects. As for the rainfall rates, the West/East gradients say the largest spikes in hourly rainfall rates as high as 6.25 mm/hour (EX_1), with 6.35 mm/hour during (EX1_2) exhibiting this rate for multiple hours. Further suggesting that the "steepness" of the gradient matters for the intensity of rainfall.

The timing of maximum accumulated precipitation was largely consistent across simulations, with only EX_1 exhibiting a notable shift of three hours earlier than CONTROL. This earlier peak accumulation likely reflects the influence of a localized high-intensity convective cell within the averaging region that produced a substantial rainfall contribution prior to the typical accumulation maximum observed in the other simulations.

In contrast, the timing of maximum hourly rainfall rate exhibited modest variability across nearly all experiments, with shifts ranging from -1 to +3 hours relative to CONTROL. Although these differences are small, they suggest subtle sensitivities in convective intensity evolution to the imposed soil moisture perturbations. This variability is consistent with differences in convective initiation timing and storm track evolution among the experiments, which can alter the phase of peak rainfall without substantially modifying the overall precipitation structure.

4.6 Surface Pressure Perturbations

These simulations support a mechanism that links the soil moisture heterogeneity to where the convection initiates. Dry soils enhance the sensible heat flux and increase the Bowen ratio leading to stronger near-surface warming and a deeper mixed layer. To maintain the surface energy balance, reduced evaporative cooling exists as a way to counteract the larger sensible heat flux (Stull, 1988).

The simulated perturbation experiments show localized surface pressure anomalies located in the areas with the imposed soil moisture gradients (Figs 4.36, 4.38, 4.37). In both perturbation orientations across all experiments, lower surface pressure develops over the warmer and drier part of the domain, while higher pressure remains over the wetter region. This pattern is consistent with a thermally induced pressure gradient force (PGF) also proposed in previous soil moisture–precipitation feedback studies (Pielke, 2001). Although the current analysis here does not directly calculate the PGF or convergence terms, the accompanying 10m wind and locations where convection initiates suggests that the differential surface heating likely contributed to low-level convergence and ascent over the dry anomaly.

The magnitude of the surface pressure anomalies associated with the soil moisture perturbations ranges from approximately [-0.68 to 0.42 hPa]. The strongest pressure perturbations are consistently collocated with the areas of the maximum edge of the dry-side of the soil moisture perturbation. Indicating that there is direct relationship between the land surface heterogeneity and the strength of the surface pressure response. The associated 10 m wind fields show a consistent response to the surface pressure gradient, with flow directed from higher pressure (wetter) regions

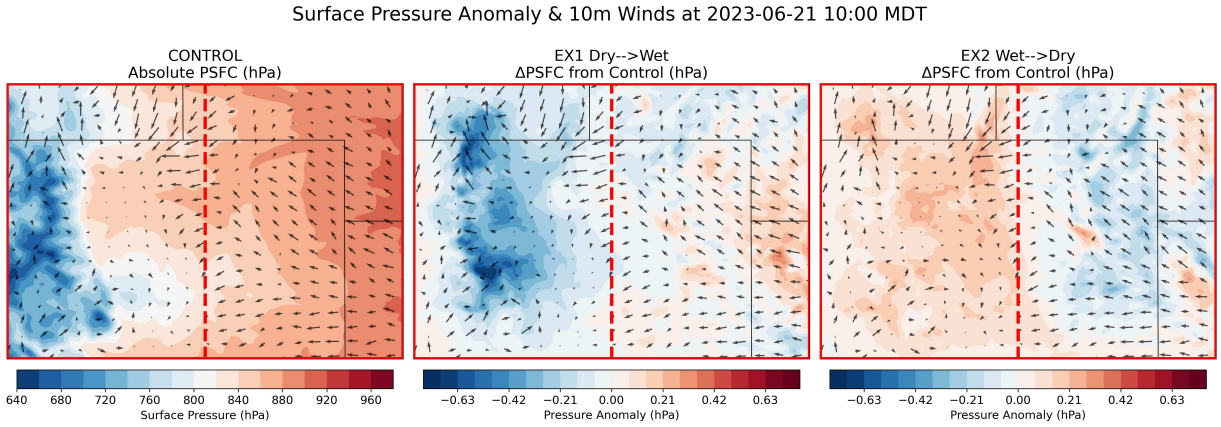


Figure 4.36: Surface Pressure anomaly and the 10 m winds at 1000 MDT from Group #1 comparing the the surface pressure of the control run to the perturbations runs.

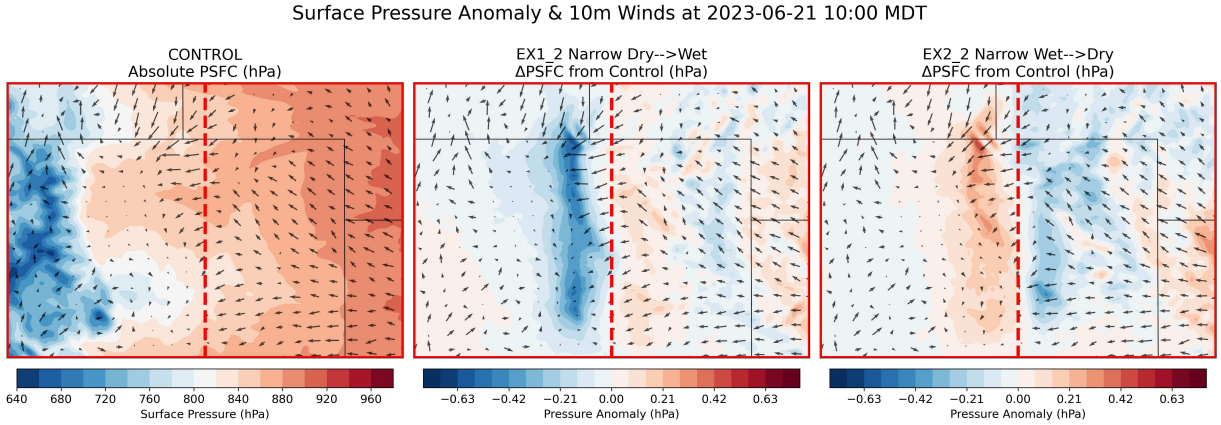


Figure 4.37: Surface Pressure anomaly and the 10 m winds at 1000 MDT from Group #2 comparing the the surface pressure of the control run to the perturbations runs.

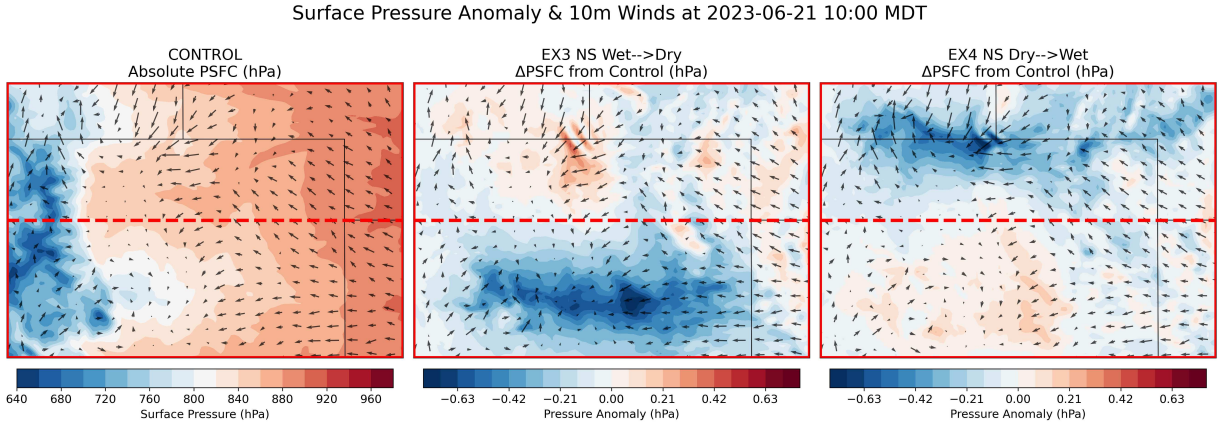


Figure 4.38: Surface Pressure anomaly and the 10 m winds at 1000 MDT from Group #3 comparing the the surface pressure of the control run to the perturbations runs.

toward lower pressure (drier) regions. The magnitude of the wind preaches a maximum values of approximately 14.25 m/s, and is strongest along the soil moisture transition zones where the pressure gradient is maximized.

Relative to the CONTROL simulation, all perturbation experiments exhibit a consistent structure in surface pressure, with lower pressure over the dry and higher pressure over the wet. This contrast is significantly weaker in the CONTROL run, confirming that the pressure perturbations arise directly from the imposed land surface heterogeneity. The alignment between surface pressure minima, low-level convergence inferred from the wind fields, and the locations of convection initiation suggests that the pressure perturbation field plays a key role in pre-conditioning the boundary layer for CI. The initiation of convection preferentially occurs near regions of strongest pressure gradient and convergence so this analysis shows the importance of pre-convection dynamics that set the stage for the storms.

4.7 Surface Divergence Anomaly

To connect how the surface pressure perturbations can impact the dynamical mechanism behind where the storms popped up, the divergence field was plotted from the 10 m level. Additionally, it is important to note that the domain spans a strong East to West orographic gradient: the Front Range and foothills to the west (elevations 3000-4000 m) transition into the High Plains to the east (1000-1500 m) over a relatively short horizontal distance. This gradient drives its own diurnal upslope circulation and associated low-level convergence along the western boundary, independent of soil moisture forcing.

The shading shows 10 m divergence ($10^{-4}\,\mathrm{s}^{-1}$; blue = convergence, red = divergence). Black contours show surface pressure (CONTROL) or ΔPSFC (perturbation panels; dashed = negative, solid = positive). The red rectangle marks the perturbation region; the red dashed line marks the dry/wet transition region. 10 m horizontal divergence, $\frac{\partial u_{10}}{\partial x} + \frac{\partial v_{10}}{\partial y}$, was computed for each experiment and compared against CONTROL and the ΔPSFC anomaly field (Figs. 4.39, 4.41) in the "pre-convection" hours.

The background orographic circulation is visible in the CONTROL panels of Figs. 4.39,4.41 (see also Fig. 3.7) and provides a good baseline against which the perturbation experiments can be compared.

In the Dry→Wet experiments (EX_1, EX1_2), a distinct convergence band develops along the dry to wet interface, coincident with a negative ΔPSFC anomaly, consistent with enhanced sensible heating over the drier surface strengthening the local thermal gradient and driving low level flow. Divergence develops in a weaker pattern, consistent with the return branch of this locally forced circulation. The Wet→Dry experiments (EX_2, EX2_2) show the mirror-image response, with the convergence band shifting to the opposite side of the domain. The same behavior is reproduced along the North to South gradient in EX_3 and EX_4. This consistency across all four configurations, its reversal under gradient reversal, and its distinction from the fixed terrain driven band in CONTROL together indicate that the soil moisture discontinuity generates a locally forced mesoscale circulation superimposed on the domain's background orographic flow. The stronger signal convergence band aligns with the drier sides and negative ΔPSFC contour, and flips between mirrored experiments (EX_1 vs. EX_2; EX_3 vs. EX_4).

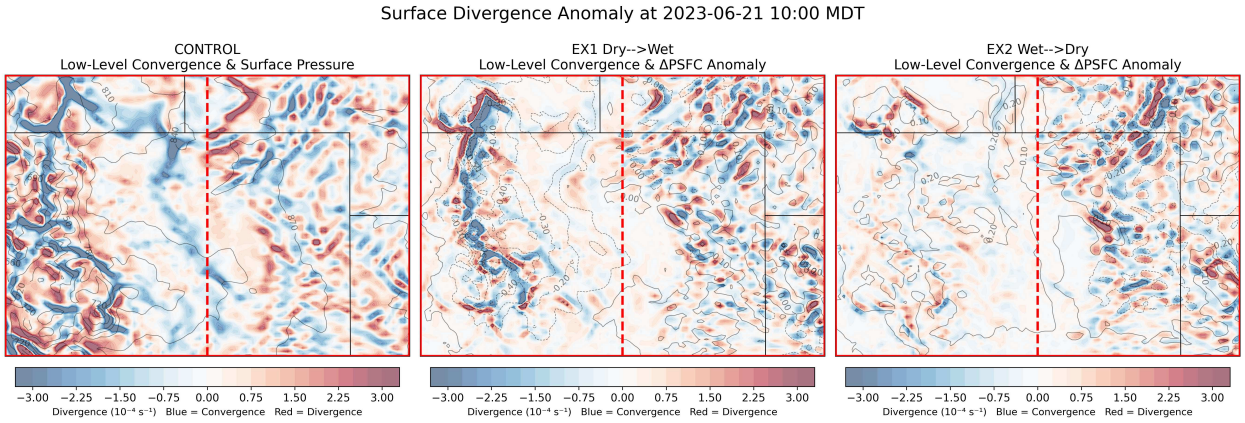


Figure 4.39: 10 m divergence ($10^{-4}\,\mathrm{s}^{-1}$; blue = convergence, red = divergence) for the broad east to west experiments. Left: CONTROL with surface pressure (hPa) contoured. Center: EX_1 (Dry→Wet). Right: EX_2 (Wet→Dry), each with ΔPSFC (hPa; dashed = negative, solid = positive). Red rectangle:perturbation region; red dashed line: dry/wet interface.

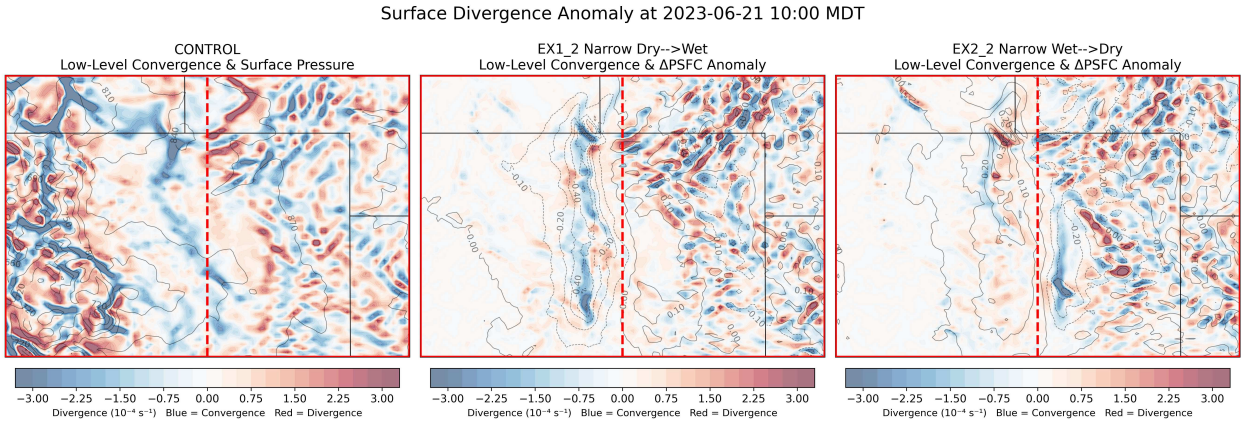


Figure 4.40: As in Fig. 4.39, for the narrow east to west experiments. Center: EX1_2 (Narrow Dry→Wet). Right: EX2_2 (Narrow Wet→Dry).

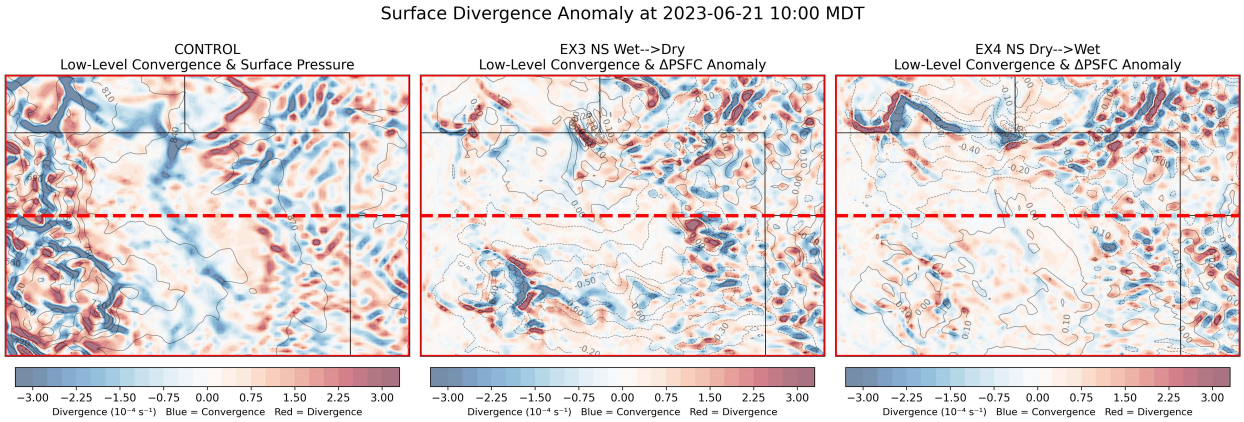


Figure 4.41: As in Fig. 4.39, for the north to south experiments. Center: EX_3 (NS Wet→Dry). Right: EX_4 (NS Dry→Wet). Red dashed line oriented horizontally, marking the north to south dry/wet interface.

Chapter 5

Discussion

5.1 Synthesis of Soil Moisture–Convection Feedback

This study investigated how the imposed soil moisture gradients in the Colorado Front Range have the ability to modify the initiation of convection, thermodynamic structure, and the storm evolution. Across all experiments and their subsequent groupings, a consistent response emerged: the initiation of convection preferentially occurred over the anomalously dry portion of the soil moisture perturbation region. This result was consistent across the perturbation orientation (N/S & E/W) along with the width of the perturbation domain.

This observed dynamical pathway is consistent with conceptual and observation studies of soil moisture precipitation feedback for semi-arid regions (Findell and Eltahir, 2003; Seneviratne et al., 2010). The preferential triggering of convection over the dry regions aligns with previous findings that surface heating gradients can dominate over the moisture availability in determining the CI location. And it is seen under these conditions that the convergence induced by differential heating exerts stronger control on CI than the near surface moisture content.

Also shown in these experiments, is that this dynamical mechanism does not require the CAPE over drier soils to be higher. Instead it depends more on the dynamical lifting to be strong enough to overcome the CIN. Both of these results highlight that in environments with gradient soil moisture, where the storms form depends more on where the air is being dynamically forced up than where the air has the most energy available.

The physical processes inferred from the results of the simulations is summarized in Figure 5.1. Dry soil perturbations enhances the sensible heating and induces pressure gradients, generating low-level convergence and ascent that favors convective initiation despite the reduced moisture availability.

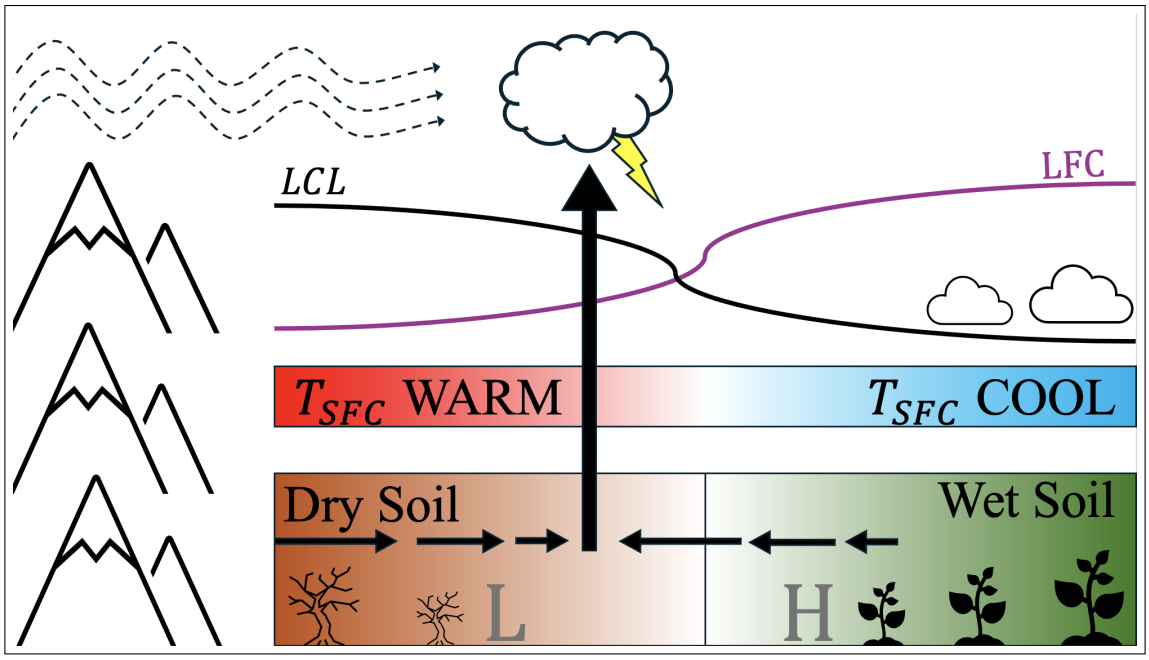


Figure 5.1: Summary of the observed results.

5.2 Thermodynamic vs. Dynamic Controls on Initiation

As expected, the wet soil perturbations did increase the near surface moisture and lowered the lifting condensation levels in all runs. And yet, the CI did not preferentially occur over the wet patches. This distinction highlights the relative importance of the dynamical forcing versus the thermodynamic pre-conditioning. In other words, which is stronger to ultimately produce a cell; the moisture availability at the surface or the thermal dynamics induced by the soil moisture perturbations?

The Skew-T analysis showed that the wet perturbations enhanced the low level dewpoints and in some cases, the CAPE as well Fig. 4.20. However, the reduced sensible heating over the wet soils limited how much the boundary layer could grow. As a result of this, the pressure perturbations and low level convergence were weakened. On the other hand, dry perturbations generated stronger mixed layer warming and had steeper low level lapse rates thereby strengthening the low level convergence and upward vertical motion. From the Skew-T analysis of Grouping #2, the observed result directly supports the idea that the location of convective initiation is determined not

by where the atmosphere is most unstable, but by where the dynamical lifting (convergence-driven ascent) is sufficiently strong to overcome the local CIN.

These findings are consistent with theoretical frameworks distinguishing between thermodynamical control and dynamical control regimes of land–atmosphere coupling (Findell and Eltahir, 2003). In this case, the environment seems to fall within a "convergence-driven" regime in which the local circulations induced by surface heterogeneity dominate over purely a moisture driven instability increases.

The results also underscore the importance of reducing convective inhibition (CIN). Even in environments with large amounts of CAPE, deep convection will not initiate without sufficient lift to reach the level of free convection (LFC). Across all experiments, the drier parts of the soil moisture gradients experienced stronger sensible heating and deeper boundary layer mixing, which likely contributed to a local weakening of CIN. And at the same time, the associated thermally induced circulations promoted low level convergence and upward motion near the dry anomalies. Together, these processes helped determine where convection was initiated. Therefore, the soil moisture patterns mainly determined where storms formed by affecting local lifting and CIN, rather than changing how unstable the atmosphere was overall.

5.3 Role of Orography in Land–Atmosphere Feedback

The Colorado Front Range is a complex environment in which terrain induced circulations interact with the land surface. Differential heating between elevated terrain and the adjacent plains commonly produces upslope flow and mesoscale convergence zones, including features synonymous with the Denver Convergence Vorticity Zone (Szoke and Shaw, 1984).

The soil moisture perturbations were overlaid onto this pre-existing terrain driven circulation area. Surface heating gradients associated with dry soil anomalies may amplify or modulate the natural mountains/plains thermal contrast. The preferential CI over dry perturbations suggests that soil moisture heterogeneity can either reinforce or locally enhance the background orographic convergence signals. Notably, the pressure perturbations induced by soil moisture variations (Fig-

ures 4.36, 4.37, and 4.38) were comparable in magnitude to those from orographic forcing itself, indicating that surface differences exert a meaningful control on the mesoscale circulation. The consistent development of pressure anomalies across all perturbation groupings further suggests that the response is robust to the orientation of the imposed gradient, even though the magnitude of the convective response varies among experiments.

However, terrain likely constrained the spatial expression of the soil moisture feedback. The alignment of initiation zones relative to elevation gradients indicates that land-atmosphere coupling in this region cannot be interpreted independently of orographic forcing. In many cases, convection initiation occurred near locations where the imposed soil moisture boundaries intersected regions already favorable for terrain-induced convergence, suggesting a cooperative interaction between the two mechanisms. The results support a framework in which soil moisture heterogeneity modulates, rather than replaces, the terrain induced circulations.

This interpretation is consistent with the conceptual view that orography establishes the broad-scale location of ascent and convergence, while soil moisture heterogeneity can modify the strength and precise location of where. This suggests a coupled, hierarchical system in which soil moisture feedback and orographic forcing are not competing mechanisms, but actually processes that work together to shape convective behavior in complex terrain environments. Because these experiments were conducted exclusively over the Colorado Front Range, the extent to which these interactions depend on the underlying terrain remains uncertain. Future studies employing flat-terrain or topographically-smoothed simulations would help isolate the relative contributions of land-surface heterogeneity and orographic forcing to convection initiation.

5.4 Special Consideration to EX_5

The experiment that most closely resembles a physical possibility is EX_5. The inspiration here was to mimic irrigation within the constraints of the model resolution. Knowing the presence and practice of pivot irrigation for agriculture in Colorado, it seemed logical to attempt to recreate this clear, real world example of land surface heterogeneity. After running the model with this soil

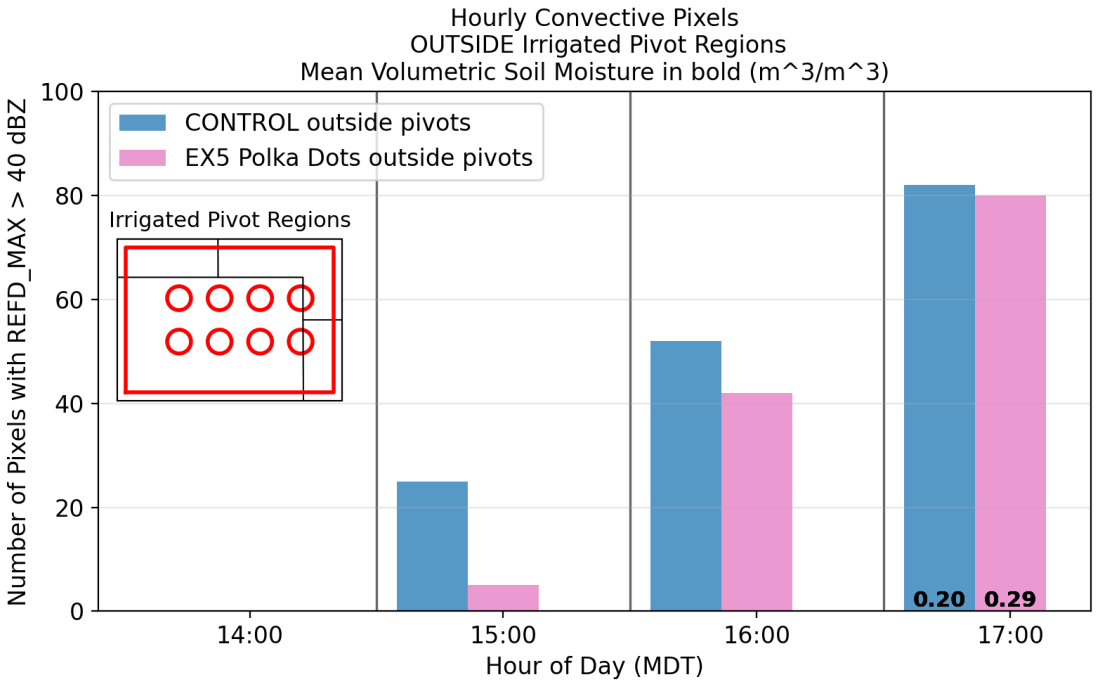


Figure 5.2: Count of convective pixels INSIDE Pivot circles area in the Polka Dot Run vs. the climatology run

moisture pattern, it was not considered in the same pattern-separated groupings. This model run does not explicitly test the magnitude and orientation of the soil moisture gradient but rather, the mechanism of evapotranspiration and low level convergence to convection. Due to it's appearance, EX_5 is logically referred to as the polka dot run.

For this section, the discussion will center around the results seen from experiment 5, and how this can be extrapolated to the possible real world implications are big irrigation impacts.

In the same analysis performed for the other groupings, EX_5 showed very little difference from the control run in terms of the Bowen ratio and convective initiation (Figs. 5.2, 5.3, 5.4). The histogram distributions of reflectivity pixels within vs. outside the moist patches (Figs 5.2, 5.3) show only marginal preference for initiation outside the patches. The difference between the inside patches and outside patches counts is also substantially smaller than the equivalent contrast between dry and wet regions of EX_1–EX_4.

When looking specifically at the reflectivity timing (Fig. 4.7), there is clear initiation around the 2nd row 2nd pivot circle over the dry section in between the perturbation circles. So the

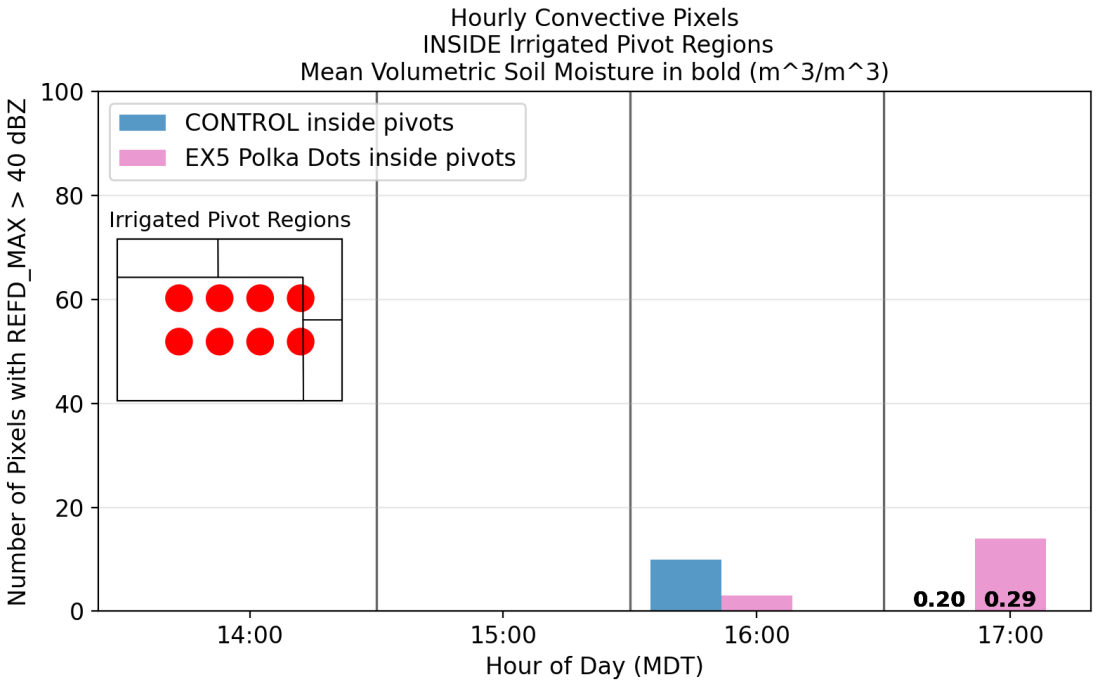


Figure 5.3: Count of convective pixels OUTSIDE Pivot circles area in in the Polka Dot Run vs. the climatology run

similar conclusion regarding CI is reinforced by the experiment. However, the size and scale of the polka dots are likely just small enough for the inner domain resolution to adequately resolve their effects. If the inner nested domain had higher resolution, while keeping the pivot circles the same size, there could possibly be a more pronounced and evident response.

Fig. 5.4 shows the total Bowen ratio taken over the polka dots and compared to the large perturbation rectangle region. The result here reinforces the response from the other runs; there is more latent heating over the anomalously wet dots when compared to the control run.

Additionally, Fig. 5.5 shows the surface pressure anomalies and the wind vectors. And the result here is consistent but not as strong as the larger linear gradients. The magnitude of surface pressure anomalies is correspondingly reduced, with maxima reaching only [0.15-0.25 hPa] compared to [0.6-0.7 hPa] in the larger gradient experiments. But there is a positive pressure anomaly over the wet dots, which reinforces the overarching governing thermodynamics.

These results are likely due to the scale of the soil moisture perturbations. With this irrigation adjacent design, the radius of the center pivot irrigation circles is 31 km (which is unrealistic).

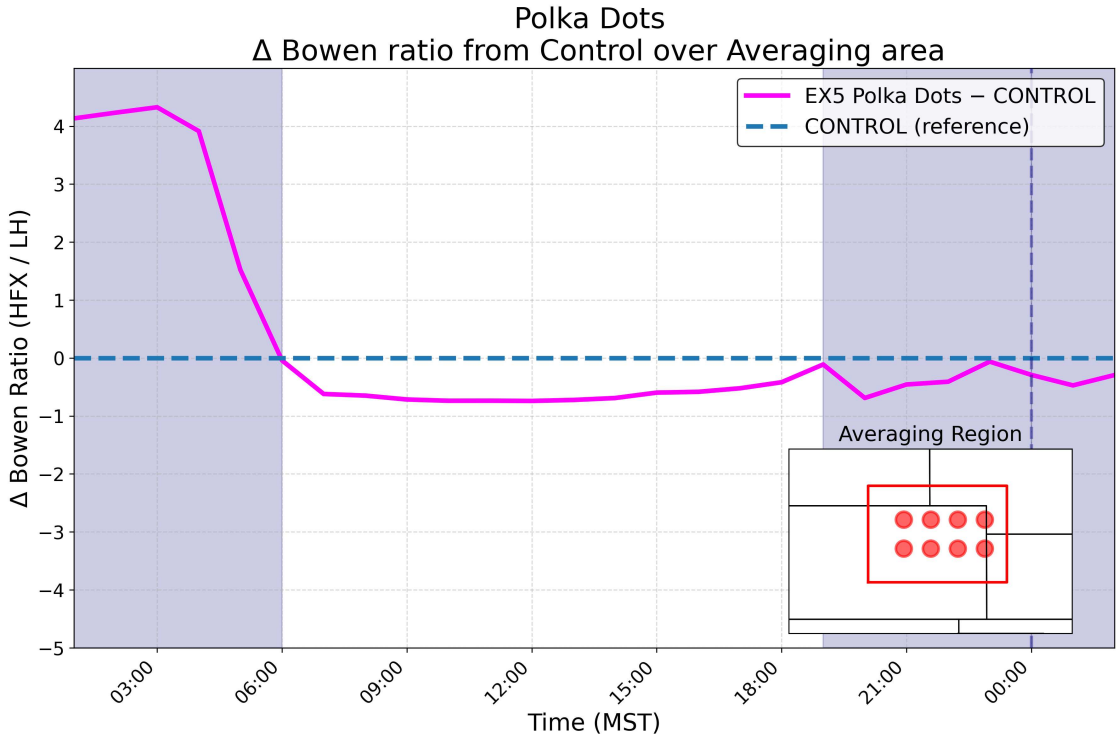


Figure 5.4: The total Bowen ratio over the Polka Dot run

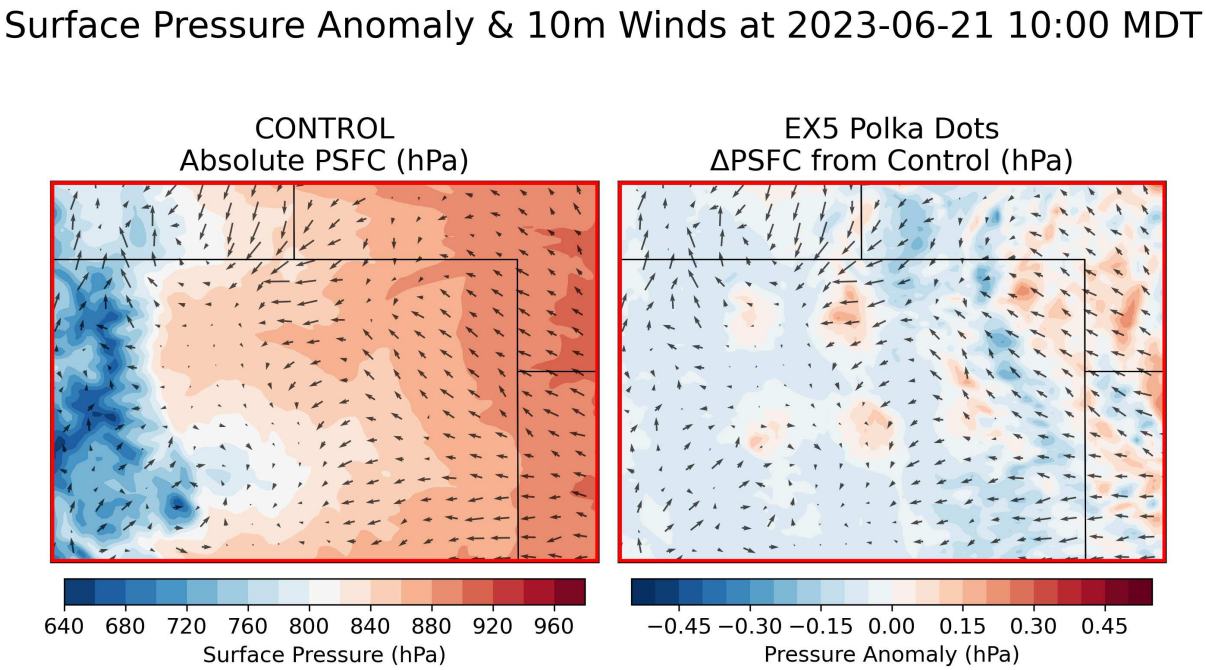


Figure 5.5: Surface Pressure anomaly and 10 m winds at 1000 MDT for the Control run and EX_5

However, the relatively weak response observed in EX_5 suggests that the spatial scale and organization of soil moisture anomalies can play a role in determining the strength of land-atmosphere feedbacks. While the experiment exhibits the same fundamental thermodynamic response observed in the larger perturbation experiments, the resulting pressure gradients and convection analysis are much weaker. This indicates that isolated moist patches may not be sufficient to largely reorganize convection within the model configuration used here, even though they can influence local thermodynamic conditions. Ultimately, the analysis showed that the "polka dot" run has the potential to influence low-level moisture in localized areas and can help initiate convection.

5.5 Limitations and Model Sensitivity

A key methodological choice in this study is the focus on a single case study based on GFS data from a real world severe weather event in eastern Colorado. This approach allows for detailed process level investigation of soil moisture feedback mechanisms under specific synoptic conditions. However, the robustness of these mechanisms across broader atmospheric and climatological contexts remains an open question. Although the observed response proved consistent across different perturbation configurations within this event, generalization to other severe weather regimes, seasons, and synoptic patterns requires more analysis of additional case studies. Future work should employ multiple model runs with perturbed initial conditions for each event to assess how soil moisture sensitivity varies across different atmospheric forcings and to quantify model internal variability.

Within this study, the imposed soil moisture perturbations represent idealized gradients rather than observed heterogeneity. Although useful for isolating physical mechanisms, real-world soil moisture patterns are more spatially complex. Additionally, these idealized simulations used a single dominant soil category (ISLTYP) across the domain, which may have not fully captured the impact of soil type variability on the land atmosphere interactions. Eastern Colorado contains diverse soil types ranging from clay-rich soils in some regions to sandy soils in others. These soil types vary with each type having distinct water holding capacity, and surface energy parti-

tioning ability. Different soil types and vegetation cover can significantly alter evapotranspiration rates, surface roughness, and thermal properties, which in turn influence boundary layer development, and convective initiation timing. Future work should incorporate spatially variable soil type classifications to assess whether our results are sensitive to soil type heterogeneity in addition to soil moisture gradients. Doing these experiments helps paint a better picture as to what the soil moisture feedback might be in places with complicated topographic and orographic settings.

Thirdly, all simulations employ a fixed set of WRF parameterizations for microphysics, planetary boundary layer, and land surface processes. This is potentially a significant constraint because these schemes govern how surface perturbations propagate to the atmosphere. The land surface parameterization controls the conversion of soil moisture into latent and sensible heat fluxes; the PBL scheme determines how these surface fluxes influence boundary layer depth and stability; and the microphysics scheme affects how boundary layer properties translate into cloud formation and precipitation. However, different model configurations could produce substantially different sensitivities to soil moisture variations. For example, a land surface scheme with higher evaporative efficiency might amplify the impact of soil moisture perturbations, while a PBL scheme with stronger vertical mixing might dampen boundary layer responses. Evaluating whether these results hold across alternative WRF configurations is essential for assessing how robust and generalizable the soil moisture feedback is as identified in this study.

Overall, the aim of this study was to analyze the specific soil-moisture feedback in eastern Colorado on a convectively active day. The analysis seeks to better understand the complex dynamics governing land atmosphere interactions under synoptically favorable severe weather conditions. The timing and spatial distribution of the observed vertical and horizontal exchanges of energy (expressed through convective initiation and storm evolution) provide insight into how surface heterogeneity can modulate mesoscale boundaries and boundary layer growth. Ultimately, this work contributes to improving understanding of land surface controls on convective predictability in semi-arid environments.

Chapter 6

Conclusion

6.1 Summary

Overall, this study demonstrates that soil moisture heterogeneity along the Colorado Front Range can exert a measurable and physically consistent influence on convective initiation and early storm evolution through dynamically driven land–atmosphere feedbacks. Across multiple perturbation orientations and spatial scales, convective initiation preferentially occurred over anomalously dry soil; not because of enhanced moisture availability, but due to stronger sensible heating, hydrostatically induced surface pressure falls, and low-level convergence that locally eroded convective inhibition. These results support a convergence-driven feedback regime in which surface thermal contrasts dominate over purely thermodynamic moisture effects in determining where deep convection is triggered.

Returning to the research questions that motivated this study: the imposed soil moisture gradients consistently changed both the timing and location of where convection initiated relative to the control simulation, with dry soil regions repeatedly favoring earlier and more spatially focused storm development. The primary mechanism connecting the land surface to convective initiation was the differential partitioning of surface energy; higher Bowen ratios over dry soils drove deeper mixed layers, stronger surface pressure gradients, and mesoscale convergence along the soil moisture gradient boundaries. The experiments further revealed that both the magnitude and orientation of the gradient mattered: sharper gradients and those oriented perpendicular to the prevailing westerly flow produced the more pronounced dynamical responses, while the meridional experiments demonstrated that the feedback is not limited to the dominant zonal gradient direction but can emerge under a range of heterogeneity configurations.

While the large-scale synoptic environment ultimately governed storm trajectory, the land surface heterogeneity from the soil moisture changed the timing, location, and structural evolution

of convection. In complex terrain such as the Front Range, where orographic circulations and boundary-layer processes already interact, soil moisture gradients can subtly, but systematically alter the summertime mesoscale dynamics. These findings underscore the importance of accurately representing land surface conditions in high resolution numerical models and suggest that soil moisture variability may contribute to predictability of convective initiation in uniquely mountainous semi-arid environments like Colorado.

These findings also have implications for the predictability of convection on sub-seasonal timescales. Because soil moisture evolves on timescales of days to weeks, far more slowly than most atmospheric variables, it can sustain surface energy partitioning across multiple convective cycles and influence both weather and regional climate variability (Guo et al., 2006). Since soil moisture changes slower than the atmosphere, it can show anomalies for longer and influence both the weather and climate based on the depth and overall interaction with the evapotranspiration mechanism. In semi-arid environments like eastern Colorado, where irrigated agriculture introduces persistent and spatially sharp soil moisture contrasts, this predictability window could be practically meaningful. Being able to accurately show these land surface conditions in high-resolution numerical models may improve not just the simulation of individual events, but the broader forecast skill for the iniation of convection in mountainous, semi-arid regions.

6.2 Future directions

Incorporating observed soil moisture fields derived from satellite retrievals or in-situ networks would improve the physical realism of the experiments and allow for more direct comparison with radar-observed convection initiation. The idealized linear gradients used in this study were valuable for isolating mechanisms in a controlled way, but natural soil moisture variability is spatially complex, temporally evolving, and influenced by vegetation, land use, and irrigation. Coupling high-resolution land data assimilation systems such as NLDAS-2 with convection permitting numerical modeling frameworks could provide a more realistic test of how observed soil moisture anomalies influence convective predictability at operationally relevant timescales.

The interaction between soil moisture heterogeneity and complex terrain also warrants deeper exploration. The Colorado Front Range represents a transitional environment where semi-arid plains meet elevated terrain, and where mountain/plains circulations coexist with the thermally driven gradients generated by land surface differences. In this study, orographic effects were present in all simulations through the terrain read into the model configuration, but their interaction with the imposed soil moisture gradients was not isolated separately. In future work, there could be a variation of the placement and orientation of soil moisture gradients relative to the terrain boundary to examine whether thermally driven circulations from land surface contrasts can constructively or destructively interfere with upslope flow and the Denver Convergence Vorticity Zone.

This study examined a single high-impact case using deterministic simulations, which limits the degree to which the results can be generalized. A natural next step would be to extend this framework to an ensemble of Front Range convective events sampled across a range of synoptic regimes, including both weakly and strongly forced environments.

Additionally, taking a ensemble based approaches would also allow for a more in-depth assessment of the sensitivity, since the response to soil moisture perturbations is likely to vary with the background thermodynamics. Events with weaker synoptic forcing may exhibit a stronger and more direct land surface control on the initiation of convection, while strongly forced cases like the one examined here may show a more modest response. Building a climatology of the sensitivities across synoptic setups would help show when soil moisture heterogeneity is most significant for operational forecasting.

Bibliography

Ashley, W. S., T. L. Mote, P. G. Dixon, S. L. Trotter, E. J. Powell, J. D. Durkee, and A. J. Grundstein, 2003: Distribution of Mesoscale Convective Complex Rainfall in the United States.

Barton, E. J., C. M. Taylor, C. Klein, P. P. Harris, and X. Meng, 2021: Observed Soil Moisture Impact on Strong Convection over Mountainous Tibetan Plateau. https://doi.org/10.1175/JHM-D-20-0129.1.

Bowen, I. S., 1926: The Ratio of Heat Losses by Conduction and by Evaporation from any Water Surface. *Physical Review*, **27 (6)**, 779–787, https://doi.org/10.1103/PhysRev.27.779.

Carbone, R. E., J. D. Tuttle, D. A. Ahijevych, and S. B. Trier, 2002: Inferences of Predictability Associated with Warm Season Precipitation Episodes. *Journal of the Atmospheric Sciences*, **59 (13)**, 2033–2056, https://doi.org/10.1175/1520-0469(2002)059<2033:IOPAWW>2.0.CO;2.

Chen, F., and J. Dudhia, 2001: Coupling an Advanced Land Surface–Hydrology Model with the Penn State–NCAR MM5 Modeling System. Part I: Model Implementation and Sensitivity. *Monthly Weather Review*, **129 (4)**, 569–585, https://doi.org/10.1175/1520-0493(2001)129<0569:CAALSH>2.0.CO;2.

Childs, S. J., and R. S. Schumacher, 2019: An Updated Severe Hail and Tornado Climatology for Eastern Colorado. https://doi.org/10.1175/JAMC-D-19-0098.1.

Colorado, W. E., 2023: Agricultural Use. URL https://watereducationcolorado.org/water-101/water-use-conservation-efficiency/agricultural-use/.

DeJonge, K. C., A. E. a. W. R. Institute, and E. i. I. a. H. Committee, 2025: Evapotranspiration Terminology and Definitions. *Journal of Irrigation and Drainage Engineering*, **151 (5)**, 06025 003, https://doi.org/10.1061/JIDEDH.IRENG-10491.

Doswell, C. A., 1987: The Distinction between Large-Scale and Mesoscale Contribution to Severe Convection: A Case Study Example.

Findell, K. L., and E. A. B. Eltahir, 2003: Atmospheric Controls on Soil Moisture–Boundary Layer Interactions. Part I: Framework Development. *Journal of Hydrometeorology*, **4 (3)**, 552–569, https://doi.org/10.1175/1525-7541(2003)004<0552:ACOSML>2.0.CO;2.

Fritsch, J. M., R. J. Kane, and C. R. Chelius, 1986: The Contribution of Mesoscale Convective Weather Systems to the Warm-Season Precipitation in the United States.

Frye, J., and T. Mote, 2010: Convection initiation along soil moisture boundaries in the southern Great Plains. *Mon. Wea. Rev.*, **138**, 1140–1151.

Gaal, R., and J. L. Kinter, 2021: Soil Moisture Influence on the Incidence of Summer Mesoscale Convective Systems in the U.S. Great Plains. *Monthly Weather Review*, **149 (12)**, 3981–3994, https://doi.org/10.1175/MWR-D-21-0140.1.

Ghausi, S. A., Y. Tian, E. Zehe, and A. Kleidon, 2023: Radiative controls by clouds and thermodynamics shape surface temperatures and turbulent fluxes over land. *Proceedings of the National Academy of Sciences of the United States of America*, **120 (29)**, e2220400 120, https://doi.org/10.1073/pnas.2220400120.

Grell, G. A., and S. R. Freitas, 2014: A scale and aerosol aware stochastic convective parameterization for weather and air quality modeling. *Atmospheric Chemistry and Physics*, **14 (10)**, 5233–5250, https://doi.org/10.5194/acp-14-5233-2014.

Guo, Z., and Coauthors, 2006: GLACE: The Global Land–Atmosphere Coupling Experiment. Part II: Analysis. https://doi.org/10.1175/JHM511.1.

Haberlie, A. M., and W. S. Ashley, 2019: A Radar-Based Climatology of Mesoscale Convective Systems in the United States. *Journal of Climate*, **32 (5)**, 1591–1606, https://doi.org/10.1175/JCLI-D-18-0559.1.

Hohenegger, C., and B. Stevens, 2018: The role of the permanent wilting point in controlling the spatial distribution of precipitation. *Proceedings of the National Academy of Sciences*, **115 (22)**, 5692–5697, https://doi.org/10.1073/pnas.1718842115.

Hong, S.-Y., Y. Noh, and J. Dudhia, 2006: A New Vertical Diffusion Package with an Explicit Treatment of Entrainment Processes. https://doi.org/10.1175/MWR3199.1.

Hubbert, J., V. N. Bringi, L. D. Carey, and S. Bolen, 1998: CSU-CHILL Polarimetric Radar Measurements from a Severe Hail Storm in Eastern Colorado.

Iacono, M. J., J. S. Delamere, E. J. Mlawer, M. W. Shephard, S. A. Clough, and W. D. Collins, 2008: Radiative forcing by long-lived greenhouse gases: Calculations with the AER radiative transfer models. https://doi.org/10.1029/2008JD009944.

Jiménez, P. A., J. Dudhia, J. F. González-Rouco, J. Navarro, J. P. Montávez, and E. García-Bustamante, 2012: A Revised Scheme for the WRF Surface Layer Formulation. https://doi.org/10.1175/MWR-D-11-00056.1.

Kain, J. S., and Coauthors, 2008: Some Practical Considerations Regarding Horizontal Resolution in the First Generation of Operational Convection-Allowing NWP. *Weather and Forecasting*, **23 (5)**, 931–952, https://doi.org/10.1175/WAF2007106.1.

Koster, R. D., and Coauthors, 2004: Regions of strong coupling between soil moisture and precipitation. *Science*, **305 (5687)**, 1138–1140, https://doi.org/10.1126/science.1100217.

Mitchell, K., D. Lohmann, P. Houser, and E. Wood, 2004: The multi-institution North American Land Data Assimilation System (NLDAS): Utilizing multiple GCIP products and partners in a continental distributed hydrological modeling system - Mitchell - 2004 - Journal of Geophysical Research: Atmospheres - Wiley Online Library. URL https://agupubs.onlinelibrary.wiley.com/doi/full/10.1029/2003JD003823.

NCEP, 2004: The GFS atmospheric model. URL https://repository.library.noaa.gov.

Ookouchi, Y., M. Segal, R. C. Kessler, and R. A. Pielke, 1984: Evaluation of Soil Moisture Effects on the Generation and Modification of Mesoscale Circulations.

Penman, H. L., 1948: Natural evaporation from open water, bare soil and grass. *Proceedings of the Royal Society of London. Series A. Mathematical and Physical Sciences*, **193 (1032)**, 120–145, https://doi.org/10.1098/rspa.1948.0037.

Pielke, R. A., 2001: Influence of the spatial distribution of vegetation and soils on the prediction of cumulus Convective rainfall. *Reviews of Geophysics*, **39**, 151–177, https://doi.org/10.1029/1999RG000072.

Rantanen, M., J. Räisänen, J. Lento, O. Stepanyuk, O. Räty, V. A. Sinclair, and H. Järvinen, 2017: OZO v.1.0: software for solving a generalised omega equation and the Zwack–Okossi height tendency equation using WRF model output. *Geoscientific Model Development*, **10 (2)**, 827–841, https://doi.org/10.5194/gmd-10-827-2017.

Schär, C., D. Lüthi, U. Beyerle, and E. Heise, 1999: The Soil–Precipitation Feedback: A Process Study with a Regional Climate Model.

Segal, M., and R. W. Arritt, 1992: Nonclassical Mesoscale Circulations Caused by Surface Sensible Heat-Flux Gradients.

Seneviratne, S. I., T. Corti, E. L. Davin, M. Hirschi, E. B. Jaeger, I. Lehner, B. Orlowsky, and A. J. Teuling, 2010: Investigating soil moisture–climate interactions in a changing climate: A review. *Earth-Science Reviews*, **99 (3)**, 125–161, https://doi.org/10.1016/j.earscirev.2010.02.004.

Skamarock, W. C., and Coauthors, 2019: A Description of the Advanced Research WRF Model Version 4.

Smith, R. B., 2019: 100 Years of Progress on Mountain Meteorology Research. https://doi.org/10.1175/AMSMONOGRAPHS-D-18-0022.1.

Sofokleous, I., A. Bruggeman, S. Michaelides, P. Hadjinicolaou, G. Zittis, and C. Camera, 2021: Comprehensive Methodology for the Evaluation of High-Resolution WRF Multiphysics Precipitation Simulations for Small, Topographically Complex Domains. *Journal of Hydrometeorology*, **22 (5)**, 1169–1186, https://doi.org/10.1175/JHM-D-20-0110.1.

Stull, R. B., Ed., 1988: *An Introduction to Boundary Layer Meteorology*. Springer Netherlands, Dordrecht, https://doi.org/10.1007/978-94-009-3027-8, URL http://link.springer.com/10.1007/978-94-009-3027-8.

Sun, J., S. Burns, A. Delany, T. Horst, and D. Lenschow, 2003: Heat Balance in the Nocturnal Boundary Layer during CASES-99. *Journal of Applied Meteorology*, **42**, 1649–1666, https://doi.org/10.1175/1520-0450(2003)042<1649:HBITNB>2.0.CO;2.

Szoke, E. J., and B. L. Shaw, 1984: AN EXAMINATION OF THE OPERATIONAL PREDICTABILITY OF MESOSCALE TERRAIN- INDUCED FEATURES IN EASTERN COLORADO FROM SEVERAL MODELS.

Taylor, C. M., 2015: Detecting soil moisture impacts on convective initiation in Europe. *Geophysical Research Letters*, **42 (11)**, 4631–4638, https://doi.org/10.1002/2015GL064030.

Taylor, C. M., C. E. Birch, D. J. Parker, N. Dixon, F. Guichard, G. Nikulin, and G. M. S. Lister, 2013: Modeling soil moisture-precipitation feedback in the Sahel: Importance of spatial scale versus convective parameterization. *Geophysical Research Letters*, **40 (23)**, 6213–6218, https://doi.org/10.1002/2013GL058511.

Taylor, C. M., C. Klein, E. J. Barton, S. Hahn, and W. Wagner, 2026: Wind shear enhances soil moisture influence on rapid thunderstorm growth. *Nature*, **651 (8104)**, 116–121, https://doi.org/10.1038/s41586-025-10045-7.

Thompson, G., and T. Eidhammer, 2014: A Study of Aerosol Impacts on Clouds and Precipitation Development in a Large Winter Cyclone. https://doi.org/10.1175/JAS-D-13-0305.1.

Tournay, R. C., 2016: LAND SURFACE SENSITIVITY OF MESOSCALE CONVECTIVE SYSTEMS.

Tripoli, G. J., and W. R. Cotton, 1981: The Use of Ice-Liquid Water Potential Temperature as a Thermodynamic Variable In Deep Atmospheric Models.

US Department of Commerce, N., 2024: Historic Tornado Event - June 21, 2023. NOAA's National Weather Service, URL https://www.weather.gov/bou/tornadoes_june_21_2023.

Weisman, M. L., C. Davis, W. Wang, K. W. Manning, and J. B. Klemp, 2008: Experiences with 0–36-h Explicit Convective Forecasts with the WRF-ARW Model. https://doi.org/10.1175/2007WAF2007005.1.

Weisman, M. L., W. C. Skamarock, and J. B. Klemp, 1997: The Resolution Dependence of Explicitly Modeled Convective Systems.

Whiteman, C. D., 2000: *Mountain meteorology: fundamentals and applications*. Oxford University Press, New York.

Xia, Y., and Coauthors, 2012: Continental-scale water and energy flux analysis and validation for the North American Land Data Assimilation System project phase 2 (NLDAS-2): 1. Intercomparison and application of model products. *Journal of Geophysical Research: Atmospheres*, **117 (D3)**, https://doi.org/10.1029/2011JD016048.

Yang, Z., and Coauthors, 2019: Irrigation Impact on Water and Energy Cycle During Dry Years Over the United States Using Convection-Permitting WRF and a Dynamical Recycling Model. *Journal of Geophysical Research: Atmospheres*, **124 (21)**, https://doi.org/10.1029/2019JD030524.

Zhang, J., and Coauthors, 2016: Multi-Radar Multi-Sensor (MRMS) Quantitative Precipitation Estimation: Initial Operating Capabilities. https://doi.org/10.1175/BAMS-D-14-00174.1.